Laboratory observations of turbulence and bed shear stress in the swash zone

Doctoral Dissertation

LABORATORY OBSERVATIONS OF TURBULENCE AND BED SHEAR STRESS IN THE SWASH ZONE

March, 2017

Graduate School of Marine Science and Technology

Tokyo University of Marine Science and Technology

Doctoral Course of Applied Marine Environmental Studies

DEJUN FENG

Abstract

This study presents detailed investigations of hydrodynamics of the flow induced by dam-break bores on an impermeable smooth slope with the main aim to improve the understanding of swash processes that characterizes the beach evolution.

As pointed out by many previous studies, the processes occurring at the edge of swash zone and in the initial stages of uprush and final stages of backwash may be the most important with regard to sediment transport but are most difficult to measure. To shed some light on these issues, laboratory experiments were carried out to resolve the velocity field evolution from the near initial uprush phases to the very late backwash phases in the upper swash zone. To this end, a high-resolution Particle Image Velocimetry (PIV) technique was specially developed. Based on the fact that large vertical velocity gradients and small bed-normal velocities characterize the bottom boundary layer flow, a rectangle interrogation window with a longer dimension in the stream-wise direction and a smaller dimension in the span-wise direction compared with that used in previous studies were adopted to give a dense spatial resolution. The accuracy was improved by applying an iteration cross-correlation scheme based on adaptive Fast Fourier Transformation (FFT) algorithm which can accelerate the computation and overcome the circularity limitation of the normal FFT. With the aid of the spatial-temporal-resolved PIV system, velocity field in the aforementioned complicated flow conditions was successfully measured for the first time. No previous studies were done in such shallow swash zone because of

the technique limitations. Using this advanced PIV technique, small-scale experiments using continuous wave laser to make high temporal resolution swash measurement and large-scale experiments using YAG laser with high magnification lens were conducted to investigate the detailed swash flow structures.

The measured velocities then were ensemble-averaged based on at least 50 events to obtain the mean velocity distribution for the small-scale experiments. Also, the large-scale experiments were repeated for 50 times within bottom boundary layer measurements and another 50 times for capturing the whole water depth. The vertical structure of the velocity was investigated according to the mean event and an individual event that selected randomly. The backwash duration is longer than the uprush duration (85%) showing the natural characteristics of asymmetry in time in the swash zone. The velocity profiles are similar to previous studies with a typical shape of turbulent flow near the bed in the uprush phases and a wall-jet like flow in the backwash phase; the measured peak uprush velocity is larger than the measured peak backwash velocity (80%). Because of the high resolution, phase lead that the lower water reverses direction firstly with respect to the upper layer water flow is firstly found to last for nearly the whole backwash in the upper swash zone. This is very different from what have been observed in the inner swash zone, where the phase lead phenomenon only exists for a short time from the start of the backwash. One explanation is related to the fact that in the upper swash location there is not enough time for the backwash flow to reestablish the velocity profile especially for the upper layer flow. This will have important effects on the sediment transport since the suspend sediments gain from the lower location cannot be carried back resulting relative

accretion here. Near-zero velocities close to the bottom in conjunction with lager velocities away from the bottom reveal that bottom boundary layer exists almost during the whole swash event. Especially, the mini bore collapse that was previously studied by numerical simulation was captured for the first time in the large-scale experiment.

Although there is no consensus on decomposition method of turbulence, it is widely acknowledged that turbulence plays an important role in sediment transport. Ensemble average method and moving average method both were used and compared to evaluate turbulent kinetic energy (TKE). Based on the ensemble average method, peak uprush TKE is 2 times larger than peak backwash TKE. In the early uprush, the TKE shows similar level in the near surface and close to the bottom, indicating a similar contribution of bore-generated turbulence and bed-generated turbulence. After the early uprush, both the surface and bed TKE injects into the water column, resulting a max TKE in the middle water layer. With surface TKE dissipating along the wave propagating, the TKE in the surface is about 60% of that near the bed in the mid to late backwash phases. Seen from the view of moving average method, peak uprush TKE is also 2 times larger than peak backwash TKE. However, both in the uprush and backwash, the surface TKE is only 15% of that near the bed, suggesting that in the shallow swash zone the bed-generated turbulence is dominant. Moreover, the depth-averaged TKE in the uprush and backwash using the moving average method is an order of magnitude smaller than that using ensemble averaging. By inspecting the PIV images and the corresponding velocity field visually, it seems that the result estimated by moving average method is more reliable since most of the bore-related turbulence should have been dissipated along the propagation to the

upper swash zone leading to less strong TKE level. TKE in the large-scale experiment is obtained by phase-averaged-data, which has some contradiction with the statement above, indicating that moving average is more suitable than the phase averaging.

Bed shear stress estimation is still debatable since there is no perfect formula that takes the characteristics of unsteadiness and non-uniformity into consideration without any simplifications. Among others, the log-law method originally formulated for steady flows is the one that widely used mainly because it is easy to apply and can give acceptable results. In this study, the upper limit of the log fitting is decided successfully and uniquely by taking the effects of fitting coefficient, non-dimensional wall unit and the error percentage between the measured velocity data and the fitted velocity data into consideration. This is the first time that bed shear stress is estimated by taking advantage of the velocity information close to bottom. Results of bed shear stress estimated using the resolved near bottom velocity information is 2-3 times greater than that of the previous studies, in which the estimation was based on relative limited near bottom information. The friction coefficients are an order of magnitude larger, correspondingly. Moreover, in the shallow swash zone, the friction coefficient shows a similar magnitude at different locations implying that the friction coefficient is more spatially constant.

Detailed laboratory measurements of velocity field in the entire water column, especially within the bottom boundary layer in the shallow swash zone were successfully measured using the advanced high-resolution PIV technique. Extensive discussions were made on the velocity profiles, turbulence distribution,

and bed shear stress evolution. Moving average method was tried in the swash zone for TKE estimation for the first time and the corresponding results queried the suitability of phase average method in estimating TKE. Bed shear stress and friction coefficient were calculated using the highly resolved near bottom velocity information and showed better results than the previous studies that the near bottom velocity field was unavailable. These novel results provide new insights into the flow processes with extremely shallow water depth. Experiments considering the roughness and permeability with corresponding numerical models of phase-depth-resolving should be carried out to further extent the understanding of swash zone in the future.

Acknowledgements

First of all, I would like to express my sincere gratitude to my supervisor Professor Okayasu Akio for providing me the opportunity to do research work in this laboratory and the continuous support of my research and life in Japan. His immense knowledge, strict logic and great sensing in advanced research inspired me a lot in how to efficiently do research work. I could not have imagined having a better advisor and mentor for my Ph.D. study.

Also, I would like to thank professors: Yoshinori Miyamoto, Ikeya Tsuyoshi, Inazu Daisuke, for their insightful comments and encouragement, also for the hard questions that incented me to widen my research from various perspectives.

Many members of laboratory have given their generous help with my experiments and shared deep discussions during these past years. Whenever I need a hand, they will right be there to help me. Their great help facilitated my learning and research. Besides, all the parties and fun we have will be the forever memory of my life in Japan.

I would like to thank The Kambayashi Scholarship Foundation and the International Office of Tokyo University of Marine Science and Technology for generously funding my Ph.D. research project.

Last but not least, I would like to thank my family: my parents, parents-in-law, my wife and my son for support and encouragement during all these years.

Table of Contents

List of Figures

Chapter 1 Introduction

1.1 The swash zone

The swash zone, where although lacks an exact definition, is arguably regarded as the most dynamic region. As illustrated in Figure 1-1, the nearshore area is roughly divided into two parts: the surf zone and the swash zone. The swash zone is usually defined as the area, where the beach is alternatively covered or uncovered by the water waves. However, the swash zone boundaries continually vary in time and space, driven by a combination of wind wave, swell, infra-gravity wave, and tidal motion. The landward boundary, or moving shoreline, may be visually identified (see Figure 1-2). Defining the seaward swash boundary in the field is more difficult. Theoretically, the location where inner surf zone bores encounter the "dry" beach face forms the seaward swash boundary. However, this location is usually blurred due to strong interactions between the inner surf and swash zones (Elfrink and Baldock, 2002; Hughes and Moseley, 2007). The constant migration of the swash zone and difficulty in defining the seaward boundary complicates the field and laboratory investigations, leading to some uncertainty when comparing with previous studies. Nevertheless, the swash zone can be readily accessed by researchers and continues to receive an increasing level of attention from the coastal engineering community.

The importance of the swash zone on a natural beach is widely recognized, one main reason is that a significant part of the sediment transport takes place in it. It is well known that the intense fluid-sediment interactions in the nearshore

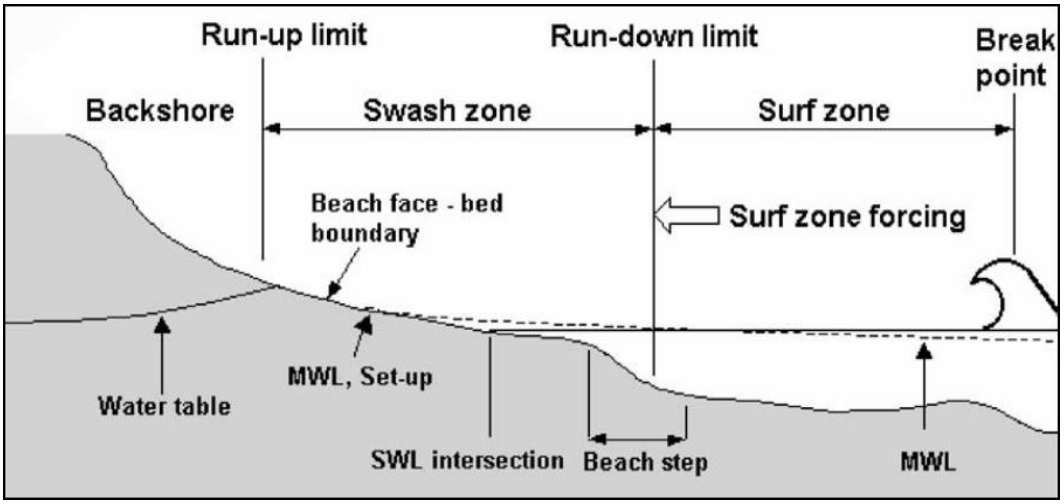

Figure 1-1 Schematic of near shore region.

Figure 1-2 Swash boundary in a real swash zone.

region lead to sediment suspension and transport that modifies the shoreline morphology. In this regard, the swash zone plays a very important role because it is the generator of shoreline erosion or accretion.

The main physical processes in the swash zone consist of flow with different frequencies induced by waves, turbulence due to wave breaking and swash-swash interaction, boundary layer flow and shear stress, longshore current; interactions with sediments and pore water; and infiltration-exfiltration. Swash zone hydrodynamics characterized by fluid uprushes and backwashes on the beach face are considered the principle driver of cross-shore sediment transport for the upper beach and foreshore and in large part controls beach face morphology. And the swash zone hydrodynamics are determined by the above numerous physical processes. Usually the landward directed fluid motion is referred as swash 'uprush', which is typically a decelerating flow with maximum fluid velocity near the shoreline. The backwash is a seaward directed accelerating flow down the beach-face after the uprush flow with a short flow reversal. It is important to recognize that the uprush and backwash are not symmetrical. Recent research results show that the flow characteristics in the two processes are different especially at the locations very near the bed where the turbulent domains the flow.

Sediment concentrations and maximum sediment transport loads in the swash zone can be larger than those in the surf zone and thus may determine the overall sediment budget for beaches. Swash zone sediment transport processes are important to society for two main reasons. Firstly, the water motion within the swash zone provides the principal mechanism for cross-shore sediment exchange

between the subaerial and sub-aqueous zones of the beach. Offshore and onshore sediment transport in the swash zone, therefore, contributes significantly to shoreline accretion and erosion. Secondly, a significant part of the longshore sediment transport occurs in the swash zone and may account for a large portion of the total littoral drift especially on steep beaches. However, prediction of sediment transport in the swash zone remains a major challenge in coastal engineering. Despite recent advances in theoretical and numerical modeling (Bakhtyar et al., 2009; Briganti et al., 2016; Calantoni and Puleo, 2006; Guard and Baldock, 2007; Karambas, 2006; Kobayashi and Johnson, 2001; Lanckriet and Puleo, 2015; Postacchini et al., 2014; Pritchard and Hogg, 2005; Torres-Freyermuth et al., 2013)and detailed field observation of sediment transport, corresponding beach morphology (Aagaard et al., 2006; Austin and Masselink, 2006; Hsu and Raubenheimer, 2006; Kelly and Dodd, 2010; Masselink et al., 2005; Weir et al., 2006) models for beach profile evolution are poor and usually unable to correctly estimate net sediment transport directions and net deposition (Masselink and Puleo, 2006; Miles et al., 2006). The difficulty is that net sediment transport in the swash zone is the difference between two very large numbers, neither of which can be quantified very well. We therefore lack the ability to predict beach face morphological change and have only a heuristic understanding of whether swash zone erosion or accretion will occur.

Bed shear stress plays a key role in the mechanics of sediment transport for its importance in determining sediment transport rates. Reliable estimation of bed shear stress is of vital importance to predict sediment transport and related scour, deposition and morphology change. For the model enhancement, it is essential to accurately evaluate the bed shear stress from flow variables in consideration of

the flow unsteadiness because most sediment transport models rely on the bed shear stress as the mobilizing force. However, the flow characteristics in the swash zone are not well understood quantitatively. This is largely attributed to difficulties in flow measurements since the water is very thin and occasionally absent. Even so, a number of experimental investigations have been done to quantify the bed shear stress both in laboratories and actual fields in the past decade (Cowen et al., 2003; Cox et al., 2000; Petti and Longo, 2001). A common approach is to measure the flow velocity in the boundary and estimate the stress by fitting the velocity profiles to the logarithmic law. The different instruments such as Laser Doppler Velocimetry (LDV), Acoustic Doppler Current Profiler (ADCP) and Particle image velocimetry (PIV) are employed in laboratory measurements of near-bed velocity profiles. The same approach is also applied to field investigations. Major problems of the approach are the difficulty in acquiring the velocity samples in leading and trailing edges and the uncertainty associated with the use of the logarithmic profile. More recently, direct measurements of the shear stress have been attempted to overcome the shortcomings of the indirect measurements (Barnes and Baldock, 2007; Barnes et al., 2009). The most results suggested that a typical value of the friction factor is different between the uprush and backwash implying the quadratic law with a constant factor produces a significant error in the model. However, the reported values of the friction factor are significantly different among the authors. There is still a large amount of uncertainty in the quantitative characteristics on the bottom friction under the swash motion.

In summary, the swash zone on most beaches is readily accessible, but this accessibility does not translate into a wide knowledge of the underlying physical

processes. This zone exhibits some of the most challenging attributes in the coastal ocean with regard to measurement and modeling campaigns. Flows in the swash zone reverse direction with the reversal timing varying across the foreshore extent. Flows are rapid and contain large sediment loads and void fraction. Turbulence is acknowledged as important for energy considerations and sediment mobility but quantification is hampered through non-stationarity and signal discontinuity (for instance due to intermittent submergence of instrumentation and/or to flows laden with bubbles and sediment). Fluid and sediment processes are further complicated by a highly variable sea bed with elevation variability occurring across a wide range of frequencies. More investigations from many aspects are needed to reach a comprehensive understanding of the swash zone hydrodynamics (Puleo and Torres-Freyermuth, 2016).

1.2 Motivation and objectives of this work

As described above, the swash zone is of vital importance to the coastal environment and of much difficulty in conducting quantitative investigations. Especially for the turbulence and bed shear stress, many researchers have devoted much effort into them and still more and more attention is being paid to them for their key role in determining the sediment transport. So, it is not only of interest but also of much practical meaning in doing research in the swash zone. In conclusion, the importance of the swash zone and the unresolved issues of turbulence and bed shear stress in the swash zone motivate me to focus my study on swash zone hydrodynamics.

The issues addressed in the preceding section lead to the below main goals of this study:

1. To evaluate the turbulence level by using ensemble average and moving average decomposition methods. Results of the TKE from the two methods will be compared so as to decide a more robust estimation of TKE in the swash zone. And the TKE evolution within the swash zone especially in the upper shallow locations will be extensively analyzed.

2. To resolve the velocity field close to the bottom so as to clarify the importance and necessary of obtaining high-resolution measurements. The bed shear stress and the corresponding friction coefficient values can be different greatly when estimated using high-resolution and coarse-resolution velocity profiles.

3. To estimate bed shear stress by using available methods. Advantages and limitations of each method are seriously discussed. The applicability of these

methods will be assessed. Especially the criteria used to decide the top elevation of the log fitting will be discussed extensively.

4. To clarify the dependences of hydrodynamics on the measurement locations. All the variables will be estimated at different locations along the swash zone.

1.3 Thesis outline

Chapter 2 gives the detailed literature review of the swash hydrodynamics including the water depth, run-up distance, velocity distribution, turbulence and bed shear stress estimation observed by methods of laboratory experiments, field investigations and numerical studies. By investigating the past studies, the unresolved issues related to this hydrodynamics can be revealed obviously. Then the research direction can be properly directed.

Chapter 3 presents the brief introduction of PIV technique, including the necessary components of a typical PIV experiments, the laser, the high-speed camera and the seeding particles. The PIV evaluation algorithm will be extensively analyzed. The common direct cross correlation calculation method, Fast Fourier Transformation (FFT) based correlation calculation method, and adapted FFT based correlation calculation method will be compared. Methods used to do post-processing also will be presented.

Chapter 4 describes the small-scale experiments in the upper swash zone aiming at presenting a detailed investigation of turbulence and bed shear stress with high-resolution velocity data. The turbulence was estimated by using ensemble average and moving average methods to decompose the turbulent components by taking advantage of the high temporal resolution measurements. And the applicability of the two methods was discussed. The boundary layer thickness and bed shear stress were estimated variable depth and a suitable method was suggested to decide the boundary layer thickness and bed shear stress.

Chapter 5 presents the large-scale experiments with object to reveal the swash hydrodynamics under field-scale flow condition. The measurements were done at three locations from the middle swash zone to the upper swash zone and the velocity field within the near-bottom was highly resolved. At every measurement location two different FOV measurements were made, a small one with focus on the boundary layer and a large one with focus on the whole water column. Velocity results from the two measurements were employed to estimate the same hydrodynamics so as to clarify the importance and necessary of the high-resolution velocity data.

Chapter 6 outlines the conclusions from this study and future work together with the limitations of this work.

Chapter 2 Literature review of swash hydrodynamics

2.1 Introduction

Because of its key role in shaping the beach, more and more societal/scientific interest is focused on the swash zone research. To describe the ideas, concepts, summarize the current research status and light the future directions in context of swash zone, the first and second workshop on swash zone processes were held in 2006 (Puleo and Butt, 2006) and 2014 (Puleo and Torres-Freyermuth, 2016), respectively. Many topics including hydrodynamics, sediment transport, and morphology were discussed and summarized as documented in Figure 2-1. Here, the current study focuses in the swash hydrodynamics. As for the hydrodynamics, it still contains kinds of subtopics: water level, turbulence, void friction, velocity profiles, wave boundary layer evolution, pressure gradients, alongshore flows, complete swash cycle measurements, cross-shore advection, swash-swash interaction, infiltration and exfiltration, extreme events, inter-swash variability and infra-gravity motions.

Numerous research efforts have been made to investigate the swash hydrodynamics. In laboratory studies, solitary wave (Alsina et al., 2009; Barnes and Baldock, 2007; Barnes et al., 2009; Sumer et al., 2011), dam-break flow (Kikkert et al., 2012, 2013; O'Donoghue et al., 2010; Othman et al., 2014; Steenhauer et al., 2011; Yeh and Ghazali, 1988), are widely used to model the swash flow since a single swash event can be easily achieved by using the two

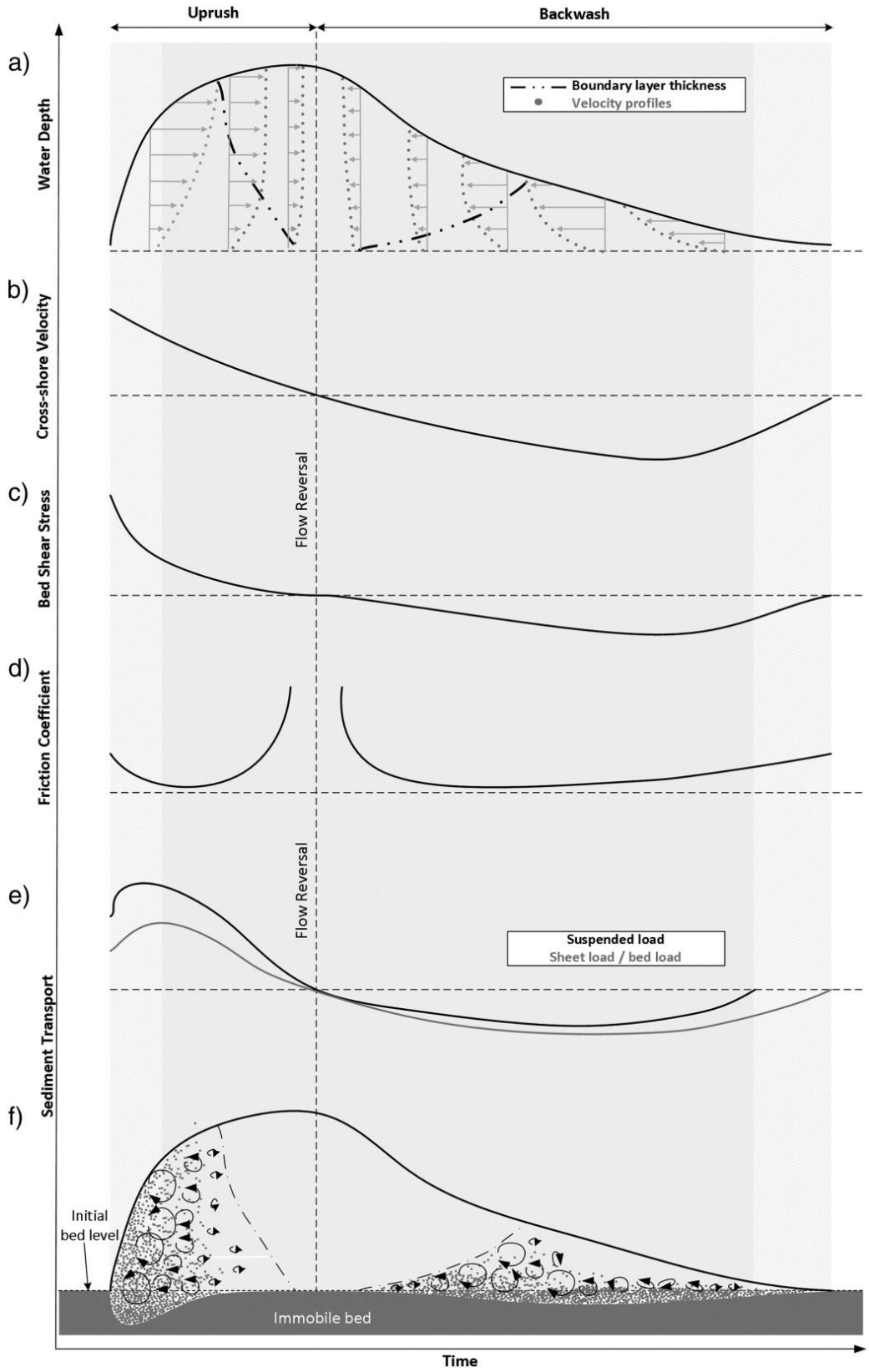

Figure 2-1 Schematic of hydrodynamics and sediment transport processes occurring within a single "free" swash event. From Chardón-Maldonado et al. (2016).

methods. There are a variety of advantages using single swash event rather than multiple-swash events. One of the obvious advantages is that it avoids the conflict of two successive swash events making the measurements and the interpretation easily. Also generating a typical swash event by ensemble averaging the regular or irregular waves (Cowen et al., 2003; Mihoubi et al., 2012; Pedrozo-Acuña et al., 2011; Sou and Yeh, 2011) is another way to study single swash event. However, generally speaking, the practical experimental conditions usually cannot meet the requirements of the ensemble averaging method. Since the repeatability is more or less not perfect that leading to some uncertainty in the results obtained by using ensemble averaging method. It should be more careful when using ensemble average method to evaluate turbulence quantitatively. Compared with laboratory studies, it is more difficult to decide a single event in the field because of the complexity of the real flow conditions. The timings of zero water depth, zero up crossings in a velocity time series, or the time between submergence and emergence of an elevated current meter usually are used to identify a single swash event (Austin et al., 2011; Baldock and Hughes, 2006; Butt et al., 2004; Hughes and Baldock, 2004; Lanckriet et al., 2014; Masselink and Russell, 2006; Masselink et al., 2009; Raubenheimer et al., 2004). As for the numerical simulation, phase-resolving approaches including depth-averaged and depth-resolving models are much popular among the wide range of numerical models. Both the two models can describe the swash flow for rough beds. Depth-averaged models provide a practical tool for engineering use, whereas the depth-resolving models can show much more details of the swash flow, especially the flow characteristics within the bottom boundary layer flow and that during the initial uprush and late backwash. However, the computation cost is

significantly high. There are two main challenges for the numerical simulation. The first one is limitations for obtaining reliable and accurate measurements within the swash zone such as bed shear stress, sediment flux, for model validation. The second one is the difficulty in applying numerical models on the real field swash condition because it is not feasible to give a suitable model setup.

In the following, the swash hydrodynamics of water level and run-up distance, velocity profile, turbulence evolution and bed shear stress estimation will be reviewed in much detail one by one.

2.2 Water depth and run-up distance

Figure 2-1 depicts a typical single swash event including water depth, cross-shore velocity, and sediment transport. Single swash event with little interaction between the backwash and the next uprush is used here to make the interpolation easier. It is very obvious that the shape of water level is asymmetric with a high increasing rate in the initial uprush stage and a relatively slow decreasing rate during the late backwash stage. The water level peaks shortly before flow reversal. (Barnes et al., 2009; Holland et al., 1995; Hughes and Baldock, 2004; Kikkert et al., 2012; O'Donoghue et al., 2010). Water depth time series are more symmetric in the landward direction as the bore head and overall momentum of the uprush are progressively reduced.

Water depth measurements can be cataloged into in situ and non-intrusive approaches. In situ measurements include Pressure Transducer (PT) and Wave Gauge (WG). For the PT, the measurements are based on the assumption of hydrostatic pressure distribution and are employed in the field. Usually these PTs are positioned just below or in vicinity of the bed. WGs are widely used in the laboratory experiments. Although some types of the WGs are specially designed for the filed observation, most of them are used in the laboratory only. In some cases, the modified WGs (resistance run-up wires) are used to measure the run-up excursion across the foreshore (Erikson et al., 2005). It should be mentioned that all the in-situ measurement instruments are suffered from the calibration and the deployment problems. For example, the PTs can be covered by a layer of sand when positioned close to the bed in the field; this can lead to the difficulty in analyzing the output data. For the WG, usually the output voltage

data can be affected by the water quality, water temperature and the duration of submergence. Therefore, a better way is to calibrate the WG before and after the experiments, and then linearly interpolate the calibration factors with respect to time. Because of these limitations of the in-situ instruments, non-intrusive techniques are becoming popular. Until now, the non-intrusive techniques used to measure free surface elevations are mainly based on sound or light. The frequently used instruments are ultrasonic displacement meters (UDM), laser-induced fluorescence (LIF), light detection and ranging (LIDAR), laser Doppler anemometry (LDA or LDV), and video imagery for shoreline position. UDMs measure free surface based on the sound speed and are affected by the air bubbles during the initial uprush stage. Widely used in laboratory, LIF can measure the water depth by using dye (Rhodamine 6G) to dye the water and using laser to illuminate the dyed water, and meanwhile a camera is used to capture the illuminated dyed water. Then by analyzing the captured recordings, the water level can be obtained. Ideally, the water surface can be distinguished easily, however, the water surface usually is ill identified because of the not sharp contrast between the water and air caused by the air bubbles. LIDAR is newly applied in the swash zone study, which is a continuously scanning laser beam that detects swash-zone water surface and exposed bed when the incident angle of the beam is approximately perpendicular to the surface (Blenkinsopp et al., 2010; Vousdoukas et al., 2014). The previous studies showed that LIDAR can measure large range swash wave depth, with the limitations of low resolution. When the wave height is small, it can hardly be captured by this instrument. Video imagery method, similar to the LIF, can detect the water level by analyzing the images recorded through the side wall of the flume using a camera (Erikson et

al., 2005; Sou and Yeh, 2011; Sou et al., 2010). Compared with LIF, the video imagery method may give less accurate result because of the low contrast between the water and air since no laser and dye are used to enhance the contrast that are necessary in LIF. In summary, both in situ and non-intrusive water depth measurements technique cannot give satisfactory results when air bubbles are present, especially in the initial uprush stage with lots of air bubbles induced by bore collapse. Accurate water depth measurements during this critical stage are demanding in the future study.

2.3 Velocity field

Velocity field is one of the most important hydrodynamics variables because many of other variables heavily depend on velocity field. Compared with surf zone flow, the swash zone flow is characterized by shallow water depth, short duration and high turbulence level. As shown in Figure 2-1, the cross-shore velocity peaks suddenly in the initiation of the uprush phase, and then decreases until the stage of flow reversal. After that the flow begins to accelerate towards the opposite direction due to the combination of favorable pressure gradient and gravitational force and peaks again. Then the flow begins to decelerate because of the dominate role of the bottom friction and finally being zero. The velocity time series also depicts asymmetry induced by the different acting directions of bottom friction, pressure gradient and gravitational acceleration. (Barnes and Baldock, 2007; O'Donoghue et al., 2010).

As stated above, many other hydrodynamic variables are heavily dependent on the velocity field. Consistent efforts are devoted to the flow velocity field measurements (Aagaard and Hughes, 2006; Barnes et al., 2009; Inch et al., 2015; Kikkert et al., 2012, 2013; Lanckriet and Puleo, 2013; Masselink et al., 2005; O'Donoghue et al., 2010; Puleo et al., 2012; Puleo et al., 2014; Raubenheimer et al., 2004; Sou et al., 2010). In situ sensors and non-intrusive techniques are employed to measure velocity. The in-situ sensors undergo high development in recent decades: impeller current meters, electromagnetic current meters (EMCM), ADV, and ADPV. Impeller current meters measure the velocity of the flowing water, and the flow rate is obtained when the velocity is multiplied by the cross-section area of the stream; usually the output data can only give the

cross-shore velocity, the along shore velocity cannot be obtained because of the sensor design. Moreover, the relative large sensor diameter in the order around 5 cm limits the application in measuring near bed velocity field (Puleo et al., 2000). EMCMs were widely used in previous studies. It can measure the cross shore and along shore velocity with a low sampling rate. The decreasing sensor size makes it possible to deploy the sensor close to the bed and the corresponding velocity field (~3 cm) can be obtained. ADVs and ADPVs are designed to record instantaneous velocity components with a relatively high frequency. Measurements are performed by measuring the velocity of particles in a remote sampling volume based upon the Doppler shift effect. Now they are very popular in the field investigation for its user-friendly design, high-precision, high sampling rate and 3D measurements. For the limitations, many outliers can occur when air bubbles are present and it is not easy to detect these outliers. Summarily, there is one main limitation of the in-situ instruments: the sensor size is relatively large so that the near bed velocity field cannot be resolved, meanwhile the sensor itself can affect the flow field, especially the flow field within the bottom boundary layer.

PIV and LDA/LDV are mostly used non-intrusive velocity measurements techniques. However, currently these techniques can only be applied in the laboratory swash experiments. There are no specially designed PIV or LAD/LAV for the field swash investigation. In recent decades, PIV is becoming more and more popular because of its full field, non-intrusive measurements. The basic principle of PIV is very easy to understand (Adrian, 1991; Stevens and Coates, 1994). A high-speed camera is used to capture images of seeding-particle-laden flow illuminated by high-power laser. Then statistical analysis is used to decide

the displacement of the particle patterns. The velocity finally can be achieved through dividing the displacement by the time interval between the successive recordings. For the typical 2D laboratory swash experiments that aims at obtaining the cross shore and along shore velocities, the camera is usually located at one side of the wave flume. It is common to deliver the laser sheet into the flow through the bed so as to avoid the reflection of air bubbles in the surface (Kikkert et al., 2012; O'Donoghue et al., 2010). The seeding particles can be sediment particles, hollow glass spheres depending on the research aims. The advantages of PIV technique are very obvious. However, the limitations of PIV technique can also not be ignored. There are several limitations regarding the application of PIV technique in the swash zone. Firstly, the concentrated bore-collapse induced entrained air in the initial stage of uprush can reflect high laser light making the image completely white, thus making it impossible to calculate the velocity field. However, as reported by Cowen et al. (2003), using fluorescent particles and optical filters can make only the particles were imaged overcoming the difficulty with bubbles. Secondly, the seeding particles in the bore front are not enough, so the recorded images cannot give correct estimation of the displacement. Thirdly, the sampling rate is relatively low when considering the short swash duration. So, as for the application of PIV technique in the swash zone, in the future the difficulty in measuring velocity field during the initial uprush phase must be solved, since the velocity field information during this short period is very important for the swash processes. The main principle of LDA/LDV is to decide the velocity by detecting the frequency shift of laser light scattered by particles suspended in the fluid (Shin and Cox, 2006). These sensors are positioned outside the wave tank and emit the laser pulse through the glass side wall. The great

advantage of this technique is the high sampling rate; the main limitation is the single-point measurement.

Both in the field investigations and laboratory studies, it is confirmed that the measured peak uprush velocity usually is larger or similar to the measured peak backwash velocities (Aagaard and Hughes, 2006; Butt et al., 2009; Conley and Griffin, 2004; Houser and Barrett, 2010; Masselink and Russell, 2006; Masselink et al., 2009; Puleo et al., 2012; Tinker et al., 2009;). The peak uprush velocities measured in the field range from 1 m/s to around 3 m/s, and the peak backwash velocities range from 0.5 m/s to 2.5 m/s depending on the slope and the roughness type of the beach and the incident wave conditions. Maximum velocity magnitudes recorded in the laboratory swash experiments can be as large as 1.5 m/s under irregular wave conditions (Alsina et al., 2012; Briganti et al., 2011).

Because most of the laboratory swash experiments are conducted in 2D wave flume, the along shore velocities are ignored. Also, in the field, since the limitation of the measurement technique, the along shore velocities are rarely reported. However, it is certain that in the natural beach, the along shore velocity also play a significant role in the swash processes. Therefore, in the future study, more attention should be paid to the along shore measurements and analysis.

2.4 Turbulence structure

Although it is very difficult to investigate the turbulence characteristics, lots of efforts have been devoted to the turbulence research because of its importance related to sediment transport in the swash zone. It is already established by previous studies that in the swash zone the uprush is connected to the bore-related turbulence and bed-generated turbulence, the backwash is connected to the bed-generated turbulence (Aagaard and Hughes, 2006; Cowen et al., 2003; Longo et al., 2002; Petti and Longo, 2001; Puleo et al., 2000; Sou et al., 2010; Zhang and Liu, 2008). Turbulent kinetic energy (TKE) and the turbulent dissipation rate per unit mass (ε) are commonly used to characterize the turbulence.

It is already acknowledged widely that obtaining the velocity fluctuations from the measured velocity data is a tough work, especially in the swash zone. What's more, because of the shallow water depth, the generation of turbulent fluctuations around the in-situ measurement sensor makes the more difficult to estimate correctly the TKE. As stated above, until now there is no established method to do the turbulence decomposition. It should be very careful when using different decomposition methods to evaluate turbulence, especially when conducting comparisons among different studies with turbulence calculated by different methods. Since the results can differ largely among different methods even for the same measured velocity data. Among others, ensemble averaging (EA) is still a powerful tool to evaluate turbulence. One of the most critical requirements of EA is the high degree of the experiment repeatability. The turbulence results can be questionable if the repeatability is not good enough.

The other issue is the number of repeats; usually 50 repeats can give fair good turbulence estimation. When discussing the EA method, two limitations should be acknowledged. Firstly, any motion that is rotational but repeatable is regarded as part of the organized motion, therefore, lead to an underestimation of the turbulent estimation. Secondly, any large deviations due to the irregularities flow motions or the non-perfect repeatability can cause additional 'pseudo-turbulence', lead to an overestimation of the turbulence estimation (Nadaoka et al. 1989). Phase Averaging (PA) method is similar to the EA, but it is not applicable in the swash zone because of the bore collapse in the shallow water. Moving averaging (MA) method that concentrates on the local time regions without considering the experimental repeatability can give satisfactory results if the sampling rate is relatively high and the choose of the moving window size is appropriate. However, in the current measurement technique conditions, the sampling rate is usually not high enough to apply the MA. For instance, in the laboratory experiments, the widely-used PIV with pulse laser can only reach a sampling rate around 30Hz or at most 100Hz that is far from the requirements of the MA. However, in the near future, with the development of the advanced measurements technique, the MA method should be a promising method for turbulence estimation. Another approach is based on filtering the velocity data, assuming that below a frequency threshold, the velocity is due to waves and all the residual contribution is due to turbulence. The results usually vary with the threshold. The common method to decide the threshold, namely the cut-off frequency, is to check the power spectrum of the velocity. The frequency around the slope break ($f^{-5/3}$) usually is defined as the cut-off frequency (Petti and Longo, 2001). It should be mentioned that the decision of the cut-off frequency may affect the level of turbulence. Another

promising technique that utilizes the difference between the measured velocities from two closely spaced sensors to estimate the average turbulent velocity variance and covariance between the sensors (Trowbridge, 1998; Shaw and Trowbridge, 2001). This method can be applied to random waves and requires that the sensors be separated such that the wave component of velocity is correlated and the turbulent component is uncorrelated between the two sensors. In general, this means that the separation distance between the sensors must be slightly larger than the largest eddy produced by wave breaking. One obvious limitation is the length scales are not well known and will likely differ under different conditions and leading to the difficulty in setting up the separate difference between the adjacent sensors.

The previous laboratory and field studies all show that uprush TKE is mainly dominated by bore-related turbulence with magnitudes from 0.02 to 0.4 m2s-2, and the main TKE mechanism is production (Zhang and Liu, 2008) and sinking of TKE into the bed (Kikkert et al., 2013; Pintado-Patiño et al., 2015). Most of the TKE content during uprush is dissipated by the time of flow reversal, decaying homogeneously (Kikkert et al., 2013; O'Donoghue et al., 2010) and similar to grid turbulence (Cowen et al., 2003; Sou et al., 2010). Backwash begins from rest with minimal initial TKE content. TKE is continuously generated at the bed (Cowen et al., 2003; Desombre et al., 2013; O'Donoghue et al., 2010; Sou et al., 2010) until the end of the backwash. The formation of a backwash bore (Zhang and Liu, 2008) and hydraulic jumps due to swash–swash interactions (Aagaard and Hughes, 2006; Butt and Russell, 2005) contribute as additional sources of TKE that can be advected back into the swash zone and/or exported to the surf zone (Butt et al., 2004; Petti and Longo, 2001). The infiltration and exfiltration of water at the

sediment water interface may also increase TKE on a permeable bed (Kikkert et al., 2013; Pintado-Patiño et al., 2015). It should be mentioned that the measurement location in most of the previous studies are located in the inner of mid swash zone, so the above mentioned TKE characteristics are only responsible for these measurement locations. As for the TKE characteristics in the outer swash zone with much shallower water depth, it may be different from that in the inner and mid swash zone since the flow property is different with less effect of motions induced by bore-collapse. In summary, swash zone turbulence is a major unsolved problem from both a theoretical and measurement standpoint. Future work should be devoted to determine the most practical approaches to quantify turbulence under natural field conditions.

2.5 Bed shear stress estimation

Bed shear stress usually is included in almost all the sediment transport formulations revealing its primate function in sediment transport processes. So methodology used to estimate bed shear stress should be investigated deeply. Bed shear stress estimation methodologies can be divided into two categories: direct investigation and indirect estimation.

Shear stress plate is used by many previous studies under different flow conditions, bore-driven swash flow and solitary swash flow (Barnes, 2009; Barnes and Baldock, 2007; Barnes et al., 2009; Barnes and Baldock, 2010; O'Donoghue et al., 2010; Pujara and Liu, 2014). The main instruments of the shear stress plate are a thin flat plate that the bed shear stress applied on and a displacement probe or a strain gauge used to detect the plate displacement. The relationship between the shear stress on the plate and the displacement of the plate should be calibrated before conducting experiments. Although the principle of the shear plate is simple and there is no need to make assumption on the flow, it faces other challenges. Pressure gradient component steamed from the secondary force on the edges of the shear plate is an important issue confronted when applying as shear plate. This side effect should be removed when obtaining bed shear stress from the output data of the sensor. Previous efforts have been made to resolve this limitation. Pujara and Liu (2014) conducted kinds of experiments with different flow regimes to measure the pressure gradient distribution at the edge of the shear plate and proposed a correction term as a function of shear plate thickness to gap size ratio and gap size to shear plate length ratio. Meanwhile, pressure gradient component was calculated by two different methods: ultrasonic

displacement sensors above the gap; and pressure tapings below the plate (Barnes et al. (2009)) to remove the effect of the pressure gradient. And it has been shown that the pressure gradient component exhibit different characteristics depending on the flow regimes. For the turbulent boundary layer flows, it has little effect on the bed shear stress and can be negligible. However, in laminar boundary layer flow, the pressure gradient component and bed shear stress present similar order of magnitudes. Considering this issue, it should be very careful to make sure the flush amount of the shear plate since large errors might be induced by any misalignments when conducting measurements. It is easier for the laboratory applications on smooth and rough fixed conditions but becomes complicated under natural beach conditions.

Hot film probe is another senor that can be used to directly measure the bed shear stress. In the field investigation, Conley and Griffin (2004) was the only previous study used flush mounted hot film anemometry on a brick under swash flows measure bed shear stress and observed strong asymmetry in bed shear stress between uprush and backwash phases. Sumer et al. (2011, 2013) conducted a series of laboratory experiments under plunging wave conditions to measure the bed shear stress and the resulted sediment transport. In their studies, hot-film sensors (0.5 mm x 0.5 mm) were utilized to measure the bed shear stress and the direction was determined from additional velocity measurements very close to the bed. Parameter of turbulent fluctuations of bed shear stress was presented taking advantage of such small sensor size. The results showed that the instantaneous bed shear stress at the swash tip could be twice the mean bed shear stress, obtained through ensemble averaging. Interestingly, a sudden increase in the magnitude of the bed shear stress in the negative direction was

observed. They concluded that this must be the time when the backwash flow boundary layer becomes turbulent generating fluctuations in the bed shear stress and causing a sudden increase in its mean magnitude.

One limitation is that, as thermal sensors, the calibration of the hot film probe is sensitive to the ambient temperature (Conley and Griffin, 2004) and errors might be magnified at high voltages due to the power relationship. Another limitation is that the direction of the bed shear stress also should be decided by the instantaneous velocity measurement close to the bed.

Compared with direct bed shear stress measurements, the indirect bed shear stress estimation is more practical, although the results also contain some degree uncertainty when applied in the swash zone. The logarithmic law has been used widely in the previous studies under different flow conditions including surf zone and swash zone both in the laboratory and in the field.

2.6 Conclusions

Swash hydrodynamics have been extensively reviewed including: water depth and run-up, velocity field, turbulence evolution and bed shear stress estimation. Thanks to the rapid development of sensor technology and novel methods in the laboratory, in the field and numerical modeling studies, the swash processes can be described in much more details. However, some problems still remain regarding the measurements or estimations of the hydrodynamic parameters in the stages of initial uprush, flow reversal, and late backwash. Since typical in situ measurements sensor size has similar order with the water depth, non-intrusive measurement techniques are preferable and can give much robust results. In the future study, the limitations of the non-intrusive measurement technique in the above-mentioned stages should be overcome so as to get a more extensive description of the whole swash event.

Chapter 3 Displacement evaluation methods for PIV

3.1 Introduction

PIV has been developed for several decades and widely employed in laboratory studies for different purposes. The main part of PIV is to extract the image pattern displacement as accurate as possible. To this end, some sort of interrogation scheme is required. Initially, this interrogation was performed manually on selected images with relatively sparse seeding which allowed the tracking of individual particles. With computers and image processing becoming more commonplace in the laboratory environment it became possible to automate the interrogation process of the particle track images. However, the application of tracking methods that is to follow the images of an individual tracer particle from exposure to exposure is only practicable in the low image density case. In principle, however, a high data density is required on the PIV vector maps, especially for the comparison of experimental data with the results of numerical calculations. This demand requires a medium concentration of the images of the tracer particles in the PIV recording. Medium image concentration is characterized by the fact that matching pairs of particle images due to subsequent illuminations cannot be detected by visual inspection of the PIV recording. Hence statistical approaches had to be developed. The commonly used approach is the FFT based cross correlation coefficient calculation. This approach can speed the calculation with little computation cost. However, it has circular

effect because of the mathematical operation of FFT. Another method is direct cross correlation coefficient calculation that gives the accurate estimation of the coefficient without the circular effects but it is very computation cost. To overcome the limitations and keep the advantages of the two approaches, an adaptive FFT based cross correlation coefficient calculation approach has been developed by previous studies. In this chapter, the principle and the main components of PIV will be presented. Later on the displacement evaluation methods will be introduced in details.

3.2 Principle of PIV

The principle of PIV will be briefly introduced in this section. The experimental setup of a PIV system typically consists of several subsystems. In most applications tracer particles have to be added to the flow. These particles should be illuminated in a plane of the flow at least twice within a short time interval. The light scattered by the particles has to be recorded either on a single frame or on a sequence of frames. The displacement of the particle images between the light pulses has to be determined through evaluation of the PIV recordings.

In order to be able to handle the great amount of data which can be collected employing the PIV technique, sophisticated post-processing is required. Figure 3-1 briefly sketches a typical setup for PIV recording in a wind tunnel. Small tracer particles are added to the flow. A plane (light sheet) within the flow is illuminated twice by means of a laser (the time delay between pulses depending on the mean flow velocity and the magnification at imaging). It is assumed that the tracer particles move with local flow velocity between the two illuminations. The light scattered by the tracer particles is recorded via a high quality lens either on a single frame or on two separate frames on special cross-correlation digital cameras. The output of the digital cameras is transferred to the memory of a computer directly.

For evaluation, the digital PIV recording is divided into small subareas called “interrogation areas”. The local displacement vector for the images of the tracer particles of the first and second illumination is determined for each interrogation area by means of statistical methods (auto- and cross-correlation). It is assumed that all particles within one interrogation area have moved homogeneously

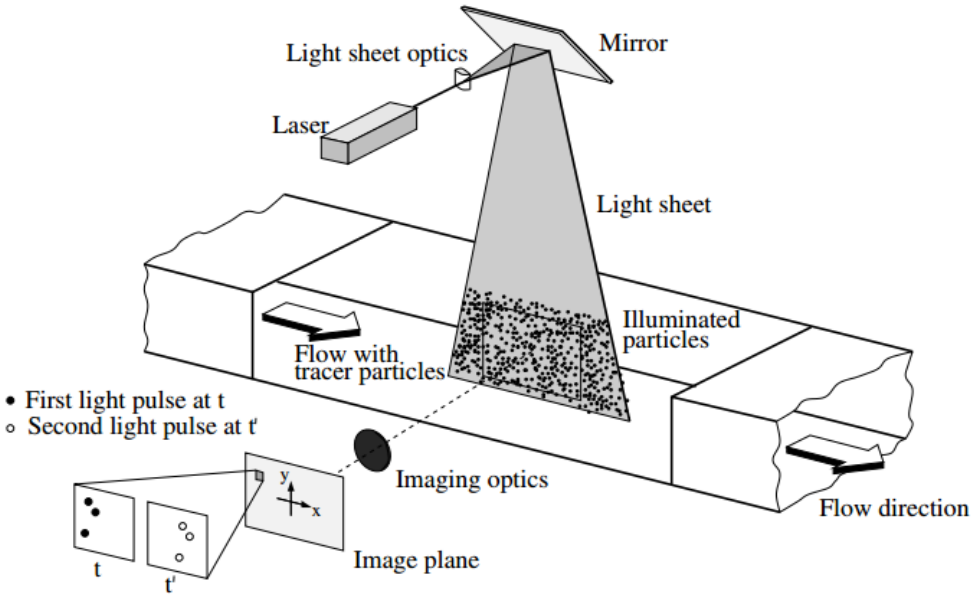

Figure 3-1 Components of a typical laboratory PIV experiment.

between the two illuminations. The projection of the vector of the local flow velocity into the plane of the light sheet (two-component velocity vector) is calculated taking into account the time delay between the two illuminations and the magnification at imaging. The process of interrogation is repeated for all interrogation areas of the PIV recording. With modern Charge Coupled Device (CCD) cameras (1000 x 1000 sensor elements and more) it is possible to capture more than 100 PIV recordings per minute. High-speed recording on Complementary Metal Oxide Semiconductor (CMOS) sensors even allows for acquisition in the kHz range. The evaluation of one digital PIV recording with several thousand instantaneous velocity vectors (depending on the size of the recording, the interrogation area and processing algorithm) is of the order of a second with standard computers. If data is required at even faster rates for online monitoring of the flow, dedicated software algorithms which perform evaluations of reduced precision within fractions of a second are commercially available.

3.3 Displacement evaluation methods for PIV

3.3.1 Direct cross correlation coefficient calculation

The key issue of the PIV analysis is to extract displacement information from the recordings. For the typical PIV recordings, the most we can get is the straight-line displacement of the particle images since the curvature information between the recording instances is lost. What's more, because of the moderate seeding density, it is too homogeneous so that it is difficult to match up discrete particles. An alternative way is to analyzing the movement of localized groups of particles, that is the particle pattern. In practice, this is accomplished by extracting small samples or interrogation windows and analyzing them statistically. In the following, the detailed procedure of the statistical analysis will be given.

Figure 3-2 shows two typical PIV images captured with a time interval of dt. The processing procedure is shown below:

1. The interrogation window should be decided firstly. Before deciding the interrogation window, usually some space between the edges should be kept so as to allow interrogation search around the interrogation window. This is shown by yellow vectors in the image at t1 = t. This space usually decided by the pre-estimated velocity of the flow. For example, if the displacement in the horizontal direction is about 10 pixels during the time interval dt, then the space between the left edge and between the right edge should be set at least 10 pixels, usually 12pixel may be better.

2. After deciding the space between the image edges, then the next step is to set

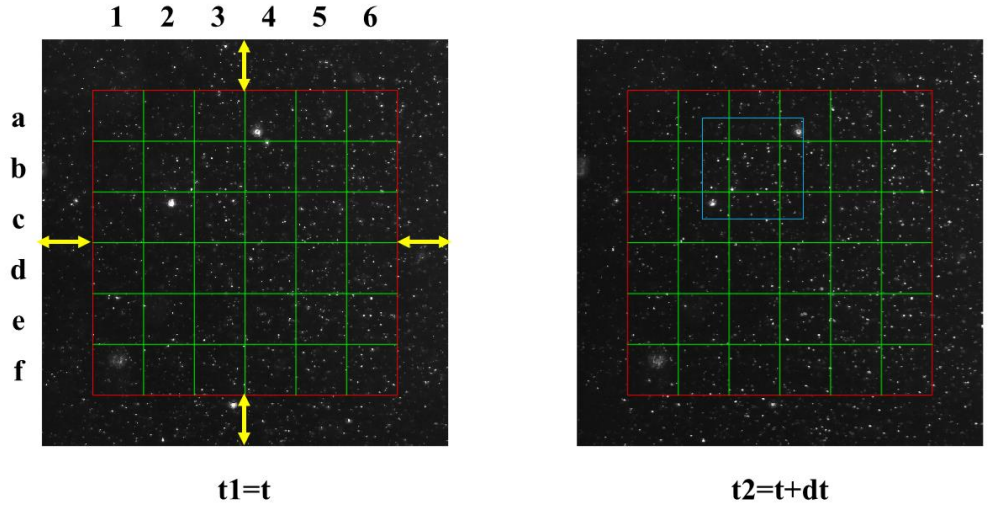

Figure 3-2 Schematic figures illustrating the direct cross correlation coefficient calculation process.

the interrogation window size. One of the important requirements when setting interrogation window size is that, at least 5-7 particles should be presented in the interrogation window; otherwise, the estimated displacement should not be accurate. There is no need to set the interrogation window into square. For example, for the flow in pipe, because of the high gradient in the span-wise direction and low gradient in the stream-wise direction, it is possible to set the interrogation window to a rectangle with longer length in the stream-wise direction. This is done with the aims to increase the resolution in the span-wise direction and increase the measurement accuracy by decreasing the effect of high velocity gradient.

3. The next step is to extract the displacement of every interrogation window. The main idea is to find the best match of the particle image pattern in interrogation window of the first image in the second image. The direct cross correlation coefficient calculation is shown in Figure 3-2. We take the interrogation window b3 as an example. Based on the pre-estimation of the velocity, the search window in the second image can be decided (the blue square). For example, the pre-estimated displacement is 5 pixels in span-wise and stream-wise direction, it is better to set the search window size 6 pixels larger than interrogation window size in each direction. The formulation used to calculate the cross-correlation coefficient is shown below in equation 3-1:

$$R(x,y) = \sum_{i=-K}^{K} \sum_{j=-L}^{L} I(i,j)I'(i+x,j+y) \qquad (3\text{-}1)$$

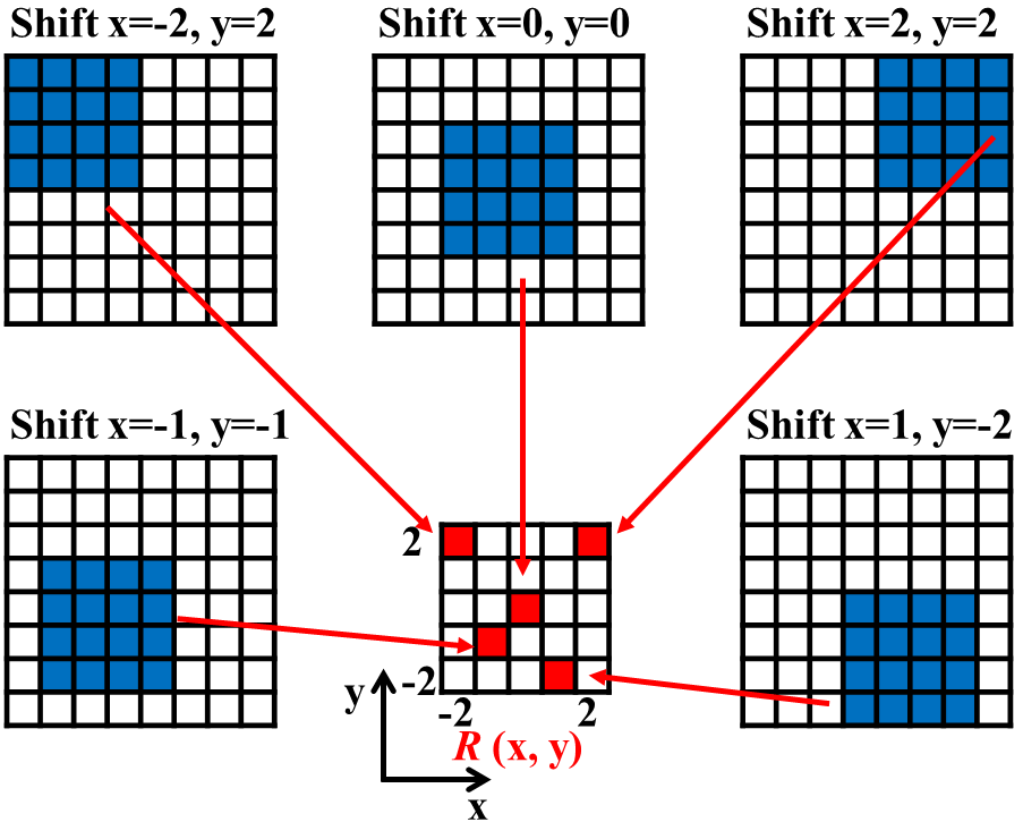

Figure 3-3 Schematic figures showing the formation of cross correlation panel.

The variables I and I' are the intensity value of the interrogation window and search window respectively. Essentially the template I is linearly 'shifted' around in the sample I' without extending over edges of I. K and L are the height and length of the template I respectively. For each choice of sample shift (x, y), the sum of the products of all overlapping pixel intensities produces one cross-correlation value R(x, y). By applying this operation for a range of shifts ($-M \leq x \leq +M$, $-N \leq y \leq +N$), a correlation plane the size of $(2M + 1) \times (2N + 1)$ is formed. This is shown graphically in Figure 3-3. For shift values at which the samples' particle images align with each other, the sum of the products of pixel intensities will be larger than elsewhere, resulting in a high cross-correlation value R at this position (see Figure 3-4). Essentially the cross-correlation function statistically measures the degree of match between the two samples for a given shift. The highest value in the correlation plane can then be used as a direct estimate of the particle image displacement

For a number of cases it may be useful to quantify the degree of correlation between the two image samples. The standard cross-correlation function equation will yield different maximum correlation values for the same degree of matching because the function is not normalized. For instance, samples with many (or brighter) particle images will produce much higher correlation values than interrogation windows with fewer (or weaker) particle images.

This makes a comparison of the degree of correlation between the individual interrogation windows impossible. The cross-correlation coefficient function normalizes the cross-correlation function equation properly:

$$c(x,y) = \frac{C(x,y)}{\sqrt{\sigma_I(x,y)}\sqrt{\sigma_{I'}(x,y)}} \qquad (3\text{-}2)$$

$$C(x,y) = \sum_{i=0}^{M}\sum_{j=0}^{N}[I(i,j) - \mu_I]\left[I'\left(i+x, j+y-\mu_{I'}(x,y)\right)\right] \qquad (3\text{-}3)$$

$$\sigma_I(x,y) = \sum_{i=0}^{M}\sum_{j=0}^{N}[I(i,j) - \mu_I]^2 \qquad (3\text{-}4)$$

Upon examination of this direct implementation of the cross-correlation function two things are obvious: first, the number of multiplications per correlation value increases in proportion to the interrogation window (or sample) area, and second, the cross-correlation method inherently recovers linear shifts only. No rotations or deformations can be recovered by this first order method. Therefore, the cross-correlation between two particle image samples will only yield the displacement vector to first order, that is, the average linear shift of the particles within the interrogation window. This means that the interrogation window size should be chosen sufficiently small such that the second order effects (i.e. displacement gradients) can be neglected. The first observation concerning the quadratic increase in multiplications with sample size imposes a quite substantial computational effort. In a typical PIV interrogation, the sampling windows cover of the order of several thousand pixels while the dynamic range in the displacement may be as large as ±10 to ±20 pixels which would require up to one million multiplications and summations to form only one correlation plane. Clearly, taking into account that several thousand displacement vectors can be

obtained from a single PIV recording, a more efficient means of computing the correlation function is required.

So far, the displacement detection is decided by the peak location of the cross-correlation coefficient. The location can be refined with values can be effectively used to estimate the mean particle image shift within the interrogation window.

It has been shown that fitting the correlation data to some function can yield robust estimation of the displacement. The most common of these three-point estimators are listed in Table 1, with the Gaussian peak fit most frequently implemented. The reasonable explanation for this is that the particle images themselves, if properly focused, describe Airy intensity functions which are approximated very well by a Gaussian intensity distribution. The following procedure can be used to detect a correlation peak and obtain a subpixel accurate (see Figure 3-5) displacement estimate of its location:

1. Scan the correlation plane R for the maximum correlation value R (i, j) and store its integer coordinates (i, j).

2. Extract the adjoining four correlation values: R(i-1, j), R(i+1, j), R(i, j-1) and

R(i, j+1).

3. Use three points in each direction to apply the three-point estimator，general a Gaussian curve.

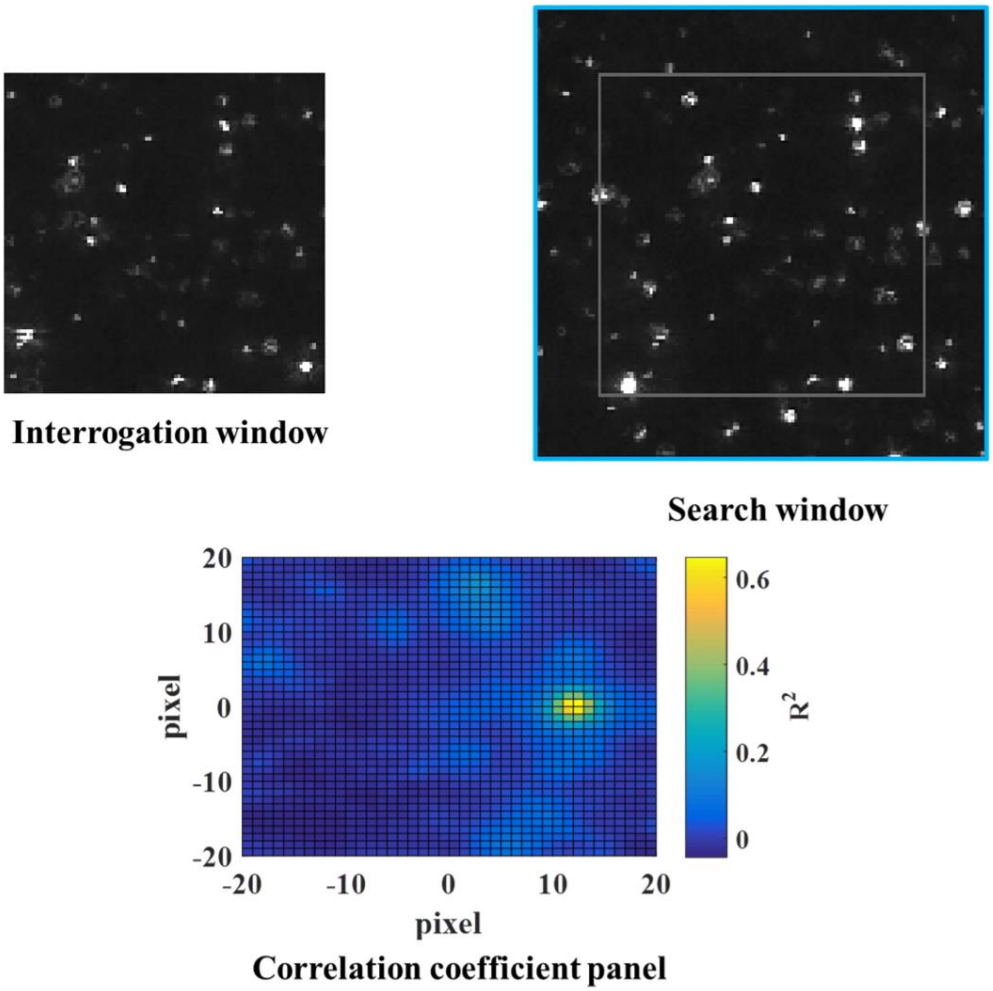

Figure 3-4 Example result of cross correlation panel.

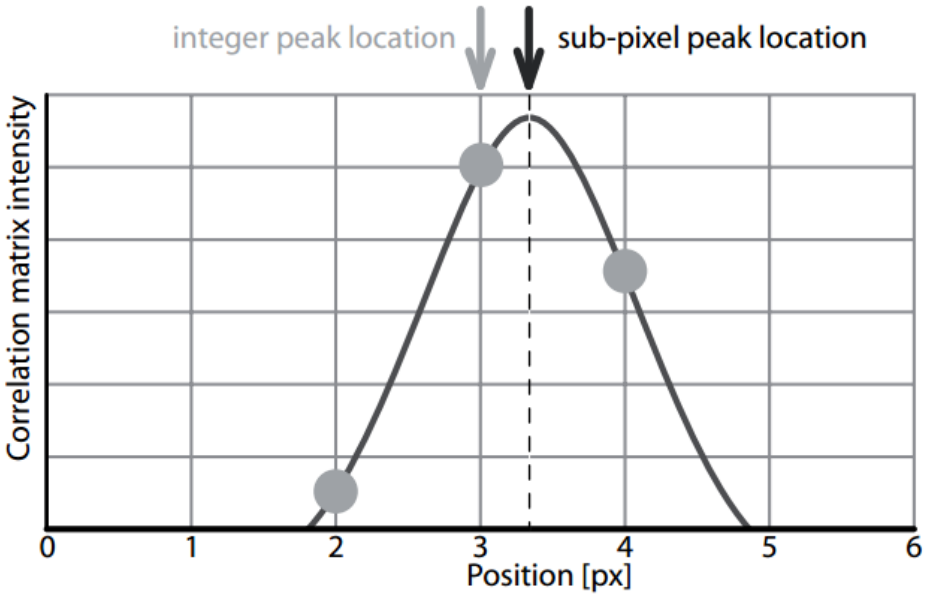

Figure 3-5 Example figure illustrating the sub-pixel estimation From Thielicke and Stamhuis (2010).

Table 1 Fitting functions for sub-pixel estimation (from Raffel, Markus, et al. (2013))

Fitting function	Estimators
Peak centroid $f(x) = \frac{first\ order\ moment}{zero\ order\ moment}$	$x_0 = \frac{(i-1)R_{(i-1,j)} + iR_{(i,j)} + (i+1)R_{(i+1,j)}}{R_{(i-1,j)} + R_{(i,j)} + R_{(i+1,j)}}$ $y_0 = \frac{(j-1)R_{(i,j-1)} + jR_{(i,j)} + (j+1)R_{(i,j+1)}}{R_{(i,j-1)} + R_{(i,j)} + R_{(i,j+1)}}$
Parabolic peak fit $f(x) = \mathrm{A}x^2 + Bx + C$	$x_0 = i + \frac{R_{(i-1,j)} - R_{(i+1,j)}}{2R_{(i-1,j)} - 4R_{(i,j)} + 2R_{(i,j+1)}}$ $y_0 = \mathrm{j} + \frac{R_{(i,j-1)} - R_{(i,j+1)}}{2R_{(i,j-1)} - 4R_{(i,j)} + 2R_{(i,j+1)}}$
Gaussian peak fit $f(x) = \mathrm{C}\exp\left[\frac{-(x_0 - x)^2}{k}\right]$	$x_0 = i + \frac{lnR_{(i-1,j)} - lnR_{(i+1,j)}}{2lnR_{(i-1,j)} - 4lnR_{(i,j)} + 2lnR_{(i,j+1)}}$ $y_0 = \mathrm{j} + \frac{lnR_{(i,j-1)} - lnR_{(i,j+1)}}{2lnR_{(i,j-1)} - 4lnR_{(i,j)} + 2lnR_{(i,j+1)}}$

3.3.2 FFT-based cross correlation calculation

Frequency domain based correlation is an alternative to calculating the correlation directly. The most feature of this method is its less computational effort. Usually this is implemented by Fourier transform algorithm. The mathematic foundation of the FFT-based correlation is that the cross correlation of two functions can be achieved by calculating the complex conjugate multiplication of their Fourier transforms. Figure 3-6 shows the implementation of cross-correlation using FFT.

In the following, the procedure of using FFT to calculate cross correlation will be shown step by step without giving the detailed mathematics equations. And these calculations are implemented in Matlab platform (see the appendix). In Matlab platform, the main core of the process is this script R=fftshift(real(ifft2(fft2(w2).*conj(fft2(w1))))). W1 is the intensity value of the interrogation window from image 1; w2 is the intensity value of the interrogation window from image 2. Figure 3-7 gives an example of the calculation. Although the principle of FFT is not easy to understand, seen from this example, it is easy to understand the calculation process. When w1 moves upward for one step, the first row should be wrapped down. When w1 moves to right for one step, the first right column should be wrapped to the first left column. This leads to the obvious side effect: bias error. With the increasing shifts, less data are actually correlated with each other since the wrapped data makes no correct contribution to the actual correlation value. Especially, the correlation values at edge are calculated based on only half of the overlapping data, the other half wrapped data really

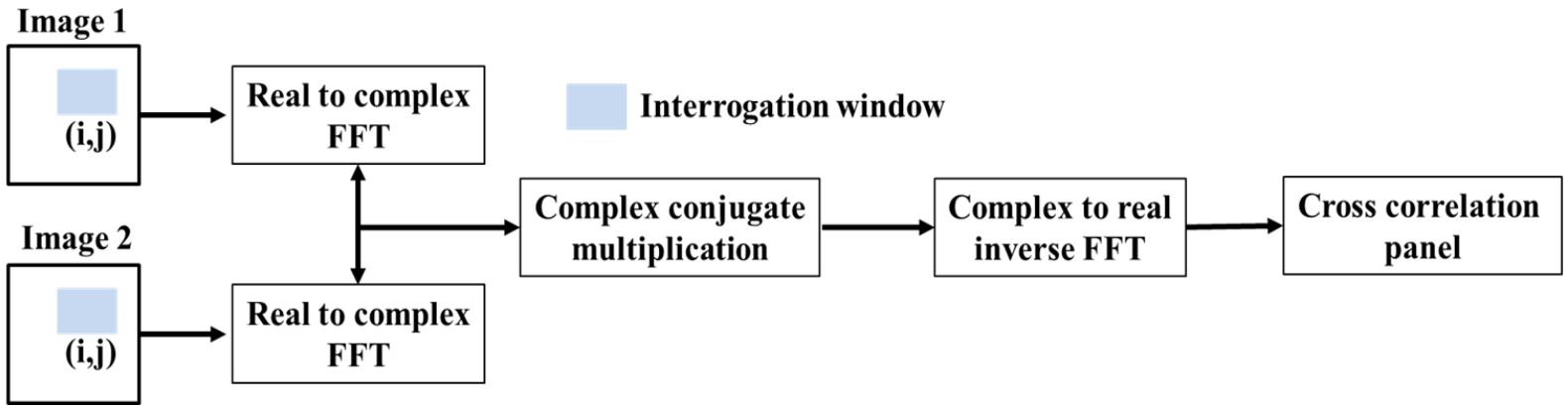

Figure 3-6 Implementation of cross-correlation using Fast Fourier Transforms

only make negative contribution. Unless the correlation values are weighted accordingly, the displacement estimate should be biased to a wrong value. Because the correlation values at the edge are worse correlated, the maximum recoverable displacement rang is limited to half of the interrogation window size. However, in practice, a more conservative but widely adopted value is quarter of the interrogation window size, this also called as one-quarter rule. To reduce the effects induced by the FFT-based calculation, the interrogation window size should be enlarged, or decrease the time interval between laser pulse so as to reduce the displacement of the seeding particles.

From the above statements, it can be concluded that, using FFT-based approach can speed the computation with the limitation of obtaining possible wrong displacement estimation.

3.3.3 Modified FFT-based correlation calculation

Ronneberger et al. (1998) proposed the modified FFT-based correlation calculation method to overcome the limitations of the normal FFT-based approach. The main idea of this method is using a trick to avoid the circular effect induced by the wrapped data in the normal FFT-based approach. Firstly, the interrogation window should be padded with zeros to the size of the search window. Then a mask of the same size with search window having values of zeros except the positions of the unpadded interrogation with values of one is generated. The main different part from the normal one is the mean value of the interrogation window is taken into consideration in iteration so as to get results that exactly the same with the direct cross correlation. The implementation procedure will be explained

w2

4	2	2	5	3	3
2	2	4	2	3	4
5	3	3	4	1	5
2	3	3	4	1	2

w1

4	4	5	4	5	2
4	2	2	2	5	2
2	1	3	3	3	4
4	3	2	4	2	2

r0=sum(sum(w1(:).*w2(:))) 224

w2

4	2	2	5	3	3
2	2	4	2	3	4
5	3	3	4	1	5
2	3	3	4	1	2

t1=[w1(2:end,:);w1(1,:)];

4	2	2	2	5	2
2	1	3	3	3	4
4	3	2	4	2	2
4	4	5	4	5	2

r1=sum(sum(t1(:).*w2(:))) 227

w2

4	2	2	5	3	3
2	2	4	2	3	4
5	3	3	4	1	5
2	3	3	4	1	2

t2=[w1(3:end,:);w1(1:2,:)];

2	1	3	3	3	4
4	3	2	4	2	2
4	4	5	4	5	2
4	2	2	2	5	2

r2=sum(sum(t2(:).*w2(:))) 211

w2

4	2	2	5	3	3
2	2	4	2	3	4
5	3	3	4	1	5
2	3	3	4	1	2

t3=[w1(:,2:end),w1(:,1)];

2	1	3	3	3	4
4	3	2	4	2	2
4	4	5	4	5	2
4	2	2	2	5	2

r3=sum(sum(t3(:).*w2(:))) 216

R=fftshift(real(ifft2(fft2(w2).*conj(fft2(w1)))));

226	226	236	211	228	225
221	204	233	227	209	218
224	220	216	224	226	226
226	218	222	219	221	222

Figure 3-7 An example showing cross correlation coefficient calculation process using modified FFT method.

step by step as follows by using the Matlab script.

1. The interrogation window size should be decided based on the flow in investigation. After that the pre-estimated displacement also should be decided then the mask M can be decided. By using the mask M the interrogation window can be padded with zeros to the size of the search window.

2. By a series of Fast Fourier transforms, the correlation coefficients can be calculated. However, only the part masked by the M is what we are interested in and is the same with the direct correlation calculation.

3.4 Conclusions

In this chapter, three methods used to calculate the cross-correlation coefficients are introduced. The direct cross correlation method gives the accurate result. However, considering the speed of the computation, it is not applicable in practice. The FFT-based approach is widely used globally both for the commercial software and personal-developed software. The greatest feature is high computation speed. However, many limitations are presented in this method, bias error, circular effects, limited measureable range and one quarter rule. Although it is used widely in the commercial software, it must be careful when using it for accurate displacement estimation. To overcome the limitations and keep the advantages, a modified FFT-based correlation calculation approach was proposed by previous studies. This method gives the same results with the direct cross correlation method with an acceptable computation speed.

Chapter 4 Small-scale swash experiments

4.1 Introduction

With the repaid development in the measurement technique and approaches, the swash zone hydrodynamics have been extensively studied in previous studies. Some general conclusions have already been made, for example, the backwash is not just a mirror process of the uprush, the mechanisms between are different; the phase lead that the flow in the bottom layer changes flow direction earlier than that in the upper layer during the flow reversal have been found; the bore-generated turbulence only exists in the uprush stage, however, the bed-generated turbulence is present during the whole swash event; the measured/estimated uprush peak bed shear stress is larger than the backwash bed shear stress. Although these findings have improved our knowledge on swash zone, the continuous efforts are still on going to confirm these conclusions and make new insights into swash zone. In filed investigation, the newly developed ADVP (Puleo et al. 2012; Inch et al., 2015) have been successfully employed to reveal the velocity profile within the bottom boundary layer and make more accurate estimation of bed shear stress. However, because of the variables in determination of bottom location under natural conditions, it confronted some uncertainty in interpreting the results. The same instruments also were used in a large-scale near-field wave flume to investigate the swash hydrodynamics (Ruju et al., 2016). Although the field investigation can show the swash processes under real natural conditions, the difficulty in controlling the natural flow condition and the measurement instruments and measuring the velocity filed very close to the

bed makes laboratory studies another alternative. Various laboratory studies (Cox et al., 2000; Petti and Longo, 2001; Archetti and Brocchini, 2002; O'Donoghue et al., 2010; Kikkert et al., 2012) have been done to document the velocity structure in the swash zone using LDV or PIV on fixed, impermeable slope. Many of these studies fitted the measured velocity profiles to the logarithmic profile, known as log law, and excellent measurement were found. However, the log law is originally developed for the uniform steady flow with fully developed bottom boundary layer; with no accelerating, reversing or stratified flows. The applicability of the log law in swash conditions with obvious acceleration and reversal phenomenon is still need to be quantified. As is known, the flow in the boundary layer is directly touched with the bottom sediments; therefore, the velocity field within in the boundary layer should be resolved as much as possible. At least, compared with the velocity profile in the vicinity of the free surface, the velocity profile within the boundary should be more important regarding to sediment transport in the swash zone. Turbulence in the swash zone is a great challenge since the turbulence decomposition method is still not established. Ensemble averaging method has been widely used in the controlled laboratory studies to separate turbulence although the perfect repeatability rarely is achieved. Moreover, turbulence estimation in the field faces much more difficulty.

This chapter presents the experiments conducted in a swash flume on smooth bed using continuous laser and high magnification camera. By employing a rectangle interrogation window, together with high magnification camera, the spatial resolution is highly improved, leading to resolved velocity measurements within the boundary layer. The continuous laser offers the possibility to extract

turbulence using moving averaging method, which is rarely implemented in the previous studies and is expected to give new insights.

4.2 Experimental setup and instrumentation

The experiments were carried out using an updated version of the open channel flume at Tokyo University of Marine Science and Technology. It consists of a water reservoir built into one end of a 7.1 m long, 0.3 m wide and 0.7 m high, glass-sided flume. The reservoir is fronted by a gate which can be raised to produce a plunging wave leading to a bore which propagates towards an impermeable slope located downstream. The dimensions of the reservoir are shown in Figure 4-1. The reservoir exit is streamlined to ensure a smooth transition for the flow from reservoir to the flume. A 1/6 transparent sloping bottom made of acrylics with a thickness of 8 mm was constructed at the other end of the flume. The slope was mounted to the side-wall of the flume to increase its rigidity. The measurements were done at two locations: L1 (120 cm from the toe of the slope), L2 (140 cm from the toe of the slope). The photo of the flume was shown in figure 4-2.

The CCD camera (Detect HAS-500) used in the experiment has a maximum framing rate of 100000 Hz and the maximum resolution is 1024 x 996 pixels. The camera can be trigged and synchronized by the outer signal. A Fujinon CF25HA-1 lens was used in the experiment. It is a high resolution industrial lens designed for robotics and machine vision. It has a 25-mm aperture that produces a 14° horizontal angle of view on 1/2-inch CCD systems. The lens was designed to be used with high resolution cameras with images up to 1.5 megapixels. Advanced glass composites and anti-reflective coatings produce detailed images with high contrast. The photo of the camera and the lens is shown in figure 4-3.

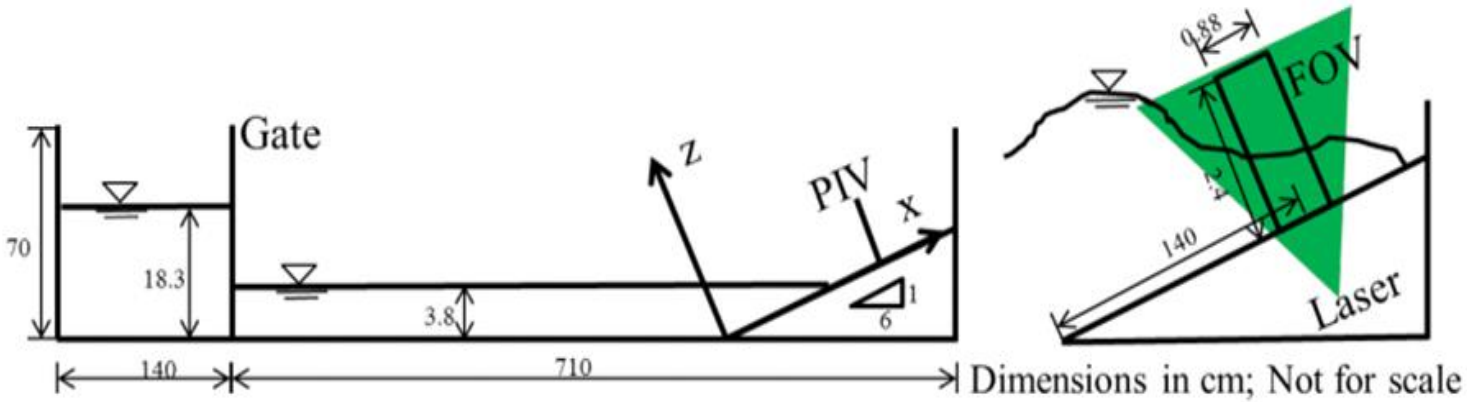

Figure 4-1 Schematic of the small-scale dam-break flume.

Figure 4-2 Photograph of the high-speed camera and the lens.

Figure 4-3 Photograph of the small-scale dam-break flume.

A continuous laser system that has a wavelength of 532nm, a maximum energy output 1W was used to illuminate the measuring section. The laser is given out through a special wire and focused by a laser head. The laser head is a special designed cylindrical plastic box that consists of a series of lenses used to focus the laser. The thickness of the laser sheet can be adjusted through rotating the cylindrical plastic box from a rand of 1mm—5cm. And the energy of the output laser sheet can be adjusted by changing the input voltage. Figure 4-4 shows the laser system.

A Stanford DG645 digital delay generator was used in the experiment to accurately trigger and synchronize the flush lamp, the wave gauge and the CCD camera. The DG645 is a versatile digital delay or pulse generator that provides precisely defined pulses at repetition rates up to 10 MHz The DG645 has many trigger modes. An internal rate generator, with less than 100 ps period jitter, may be set from 100 μHz to 10 mHz with 1 μHz resolution. An external trigger input, with adjustable threshold and slope, can trigger a timing cycle, a burst of cycles, or a single shot. A single shot can be triggered with a key press. A line trigger operates synchronously with the AC mains. A rear-panel trigger inhibit input can disable the trigger or any of the pulse outputs during a timing cycle. In the experiment, the external single shot trigger mode was used to trigger the CCD camera and synchronize the wave gauge and the flush lamp. The photo of the DG645 is shown in the figure 4-5.

It is clear from the principle of PIV that this technique is indirect as it determines the particle velocity instead of the fluid velocity. Therefore, fluid mechanical properties of the particles have to be examined in order to avoid

Figure 4-4 Photograph of the continuous wave laser system.

Figure 4-5 Photograph of the DG645 digital delay generator.

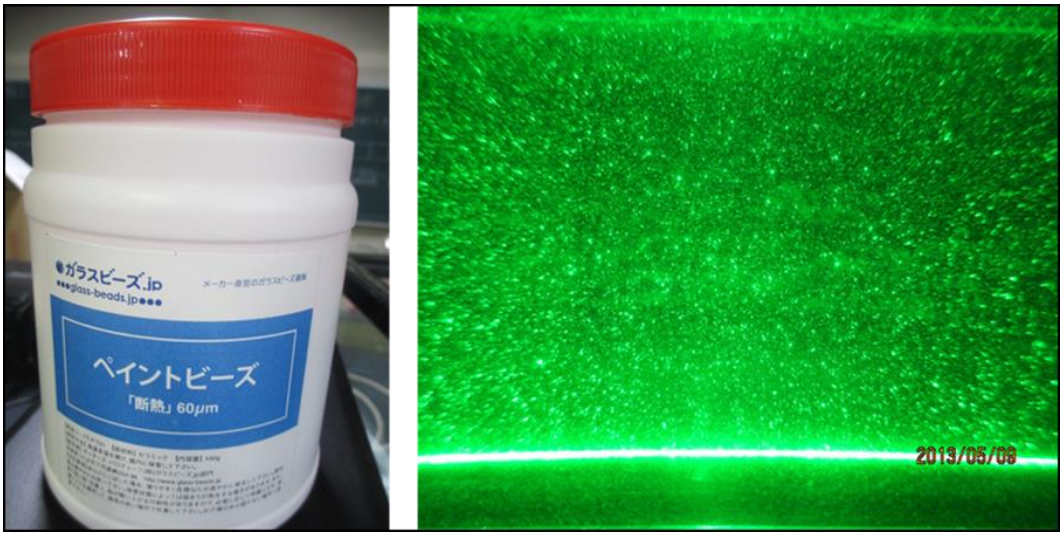

Figure 4-6　Photograph of the glass beads and laser illuminated particles.

significant discrepancies between fluid and particle motion. Proper tracer particles must be small enough to follow (trace) fluid motion and should not alter fluid or flow properties. And proper tracer must be large enough to be visible by the camera. Uniform seeding is critical to the success of obtaining velocity field. In addition, the concentration of the tracer particles must be test to make sure good images can be obtained using the specified concentration. In the experiment, glass beads with a mean diameter of 60 μm were used for its specific gravity is slightly larger than water that can follow the water very well. After a series of test the concentration of the particle was chosen to be 0.08 g/L. The photo of the particle was shown in Figure 4-6

The water depth in the reservoir was measured by a twin-wire capacitance wave gauge. In order to know the time when to raise the gate, a flush lamp was used as an indicator and when it gives a flush then the gate was raised. And a pump was used to pump water into the reservoir from the downstream of the flume.

The experiments were conducted for one initial condition only: a water depth in the reservoir h1 of 183 mm and a water depth in front of the gate h2 of 38 mm. The origin of the x-z coordinate system is at the initial shoreline position, located 5.8 m from the reservoir gate; the x-axis is parallel to the slope and is positive shoreward; the z-axis is perpendicular to the slope. The corresponding velocity components are u and w, respectively. To guarantee that every time the initial condition is the same that is the timing when raising the gate the water depth in the reservoir is the same and the CCD camera can work automatically when the gate was raised, a wave gauge was installed in the reservoir and was used as a

reference signal for externally triggering the CCD camera and the flush lamp with a preset threshold based on the water depth in the reservoir. The digital delay generator, the CCD camera, the wave gauge and the flush lamp were connected together by BNC-splitters. Because the bore will propagate about 1second before reaching the slope, then the time delay between the timing when raising the gate and the timing when the CCD camera beginning to take image is 1 second to save the memory of the camera.

The procedures of the experiments were summarized below:

1. The best focus of the laser with a thickness of 1 mm of the laser sheet at the measurement location was achieved by adjusting the laser head box.

2. The laser head was fixed on a long aluminum board firmly and then the board was put just under the slope. Illuminating the measurement section from beneath the slope can eliminate the negative effects of the surface reflections compared with illuminating vertically downwards from the above. The distance between the center of the laser beam and the nearer sided glass wall is about 2.5mm that is enough to avoid the boundary effect of the glass wall.

3. The camera was rotated to be aligned with the 1/6 slope, so that the bed-normal and the bed-parallel velocities can be measured. The camera working frequency was set to be 2000 Hz, which means that 2000 frames can be captured within one second. And the shutter speed was chosen to be 4000, which means the shutter is open for only 1/4000 second within one frame (1/2000 second). The camera was controlled by specified software. To trigger the camera by external signal, the External Trigger model was chosen in the current experiments. After

recording, the images should be saved into disk by clicking the corresponding button in the software control panel. It is better to save the description of the images including the information of the date and the size when saving the images.

4. The calibrations in the experiments are very important since small errors in calibration can produce big errors. The calibrations were used to enable the measurements to be converted from pixel-space into mm-space. A ruler glued onto an acyclic plate was used in the experiment as the calibration instrument. When conducting the calibration, the special designed instrument will be glued onto the slope just aligned with the laser sheet. That means the laser sheet just goer through ruler. Then a bore was made to make sure that the instrument was immersed by the water, and at the same time images were taken. By checking the recoded images, whether the focus of the lens is good enough or not can be concluded. Through multiple times of the repeats of the test, good focus can be adjusted. It is should be emphasized that the calibration must be done with the ruler immersed by water since the difference between the cases of with water and without water is very large.

5. After the adjustments of the above instruments, the bore was to be generated. A pump put in front of the gate was used to pump water from the front of the gate into the reservoir to the fullest extent. After that the pump was taken out of the flume. Because the seal between the gate and the reservoir is not good enough the water always leaks from the reservoir into the flat flume, then it still needs to wait for some time before lifting the gate. During the time interval, the wave gauge installed 50 cm from the toe of the slope used to check the experimental

repeatability will be turned on. At the timing when the water depth in the reservoir reaches the specific value that corresponds to the presented threshold voltage value in the digital delay generator the flush lamp will send out a flash. At the timing when a flash was observed the gate will be raised by hands. Then after one second the CCD camera will begin to record images automatically. The recorded images will be saved manually with the description information.

6. The experiment was repeated for 100 times in total with the aim to investigate the characteristics of the flow in the swash zone from the view of ensemble averaged case and individual case.

4.3 PIV recordings processing

Ideally, if the repeatability of the experiments is perfect, then for every run the wave front enters into the view of the camera and exits the view of the camera at the same timing. However, in practice, this is usually rarely achieved especially in the swash zone because of the shallow, short-duration, turbulent flow. It has been reported that this can be satisfactorily achieved in the case of deep water with regular waves. In this study, it is much worse for the following reasons. First, the speed of gate lifting is different from run to run because it is difficult to make sure that every time hand can lift the gate using the same force. Second, the seals among the gate and the two sides and bottom of the flume is not tight enough, water always leaks from these seals into the flume. Third, the camera is triggered at the timing when the water level in the reservoir decreases to the threshold (detected by the wave gauge). However, there is a time delay between seeing the flush lamp (water level deceases to the threshold) and lifting the gate that is the reaction time. Due to the combined reasons of the three, the timing of entering into the view of camera is different from run to run. To deal with this problem, swash event is decided in this way: when the water depth increases into 4 mm in the uprush, this timing is regarded as the beginning; when the water depth decreases into 2 mm in the backwash, this timing is regarded as the end. The two water levels were chosen as reference for that the water level can be easily decided in these levels. For example, during the early uprush, it is not easy to satisfactorily decide the water level when it is only about 1 mm. The time interval from the beginning to the end is defined as swash duration. Since there is no need to take much concentration on the swash beginning and swash end because of the above reasons, the swash durations are inspected to quantify the repeatability of

the experiments. The swash durations for every event at the two locations are presented in Figure 4 -7. The upper panel is for location 1 and the bottom panel is for location 2, respectively. The values of the standard deviation over the mean value are 2.2% and 6.2% at the two locations indicating good repeatability of the experiments. But it is still need to note that there are several events that are relatively far from the mean value. It is sure that this will affect the results. However, considering the large total event numbers, it is acceptable to include these events into ensemble averaging processes.

After deciding the timings of swash beginning and ending of every event, the times-tack of the swash event can be obtained based on these timings. Time-stack image can be used to evaluate the free water surface so it functions like a wave gauge. One example of the time-stack at location 2 is shown in Figure 4-8. Although the free water surface cannot be detected exactly because of the air bubbles in the surface and the reflections of the surface particles, the rough surface can be decided. These detected rough free water surfaces can be used as mask of the recordings for the deciding the area of PIV calculation. These time-stacks were presented for every swash event for determining the PIV calculation area.

Before conducting PIV experiments，pre-processing of the image usually is needed. The main goal is to enhance particle image contrast and to bring particle image intensities to a similar signal level such that all particle images have a similar contribution in the correlation function. The intensity capping technique (Shavit U et al., 2007), which was found to be both very effective and easy to implement, relies on setting intensities exceeding a certain threshold to the

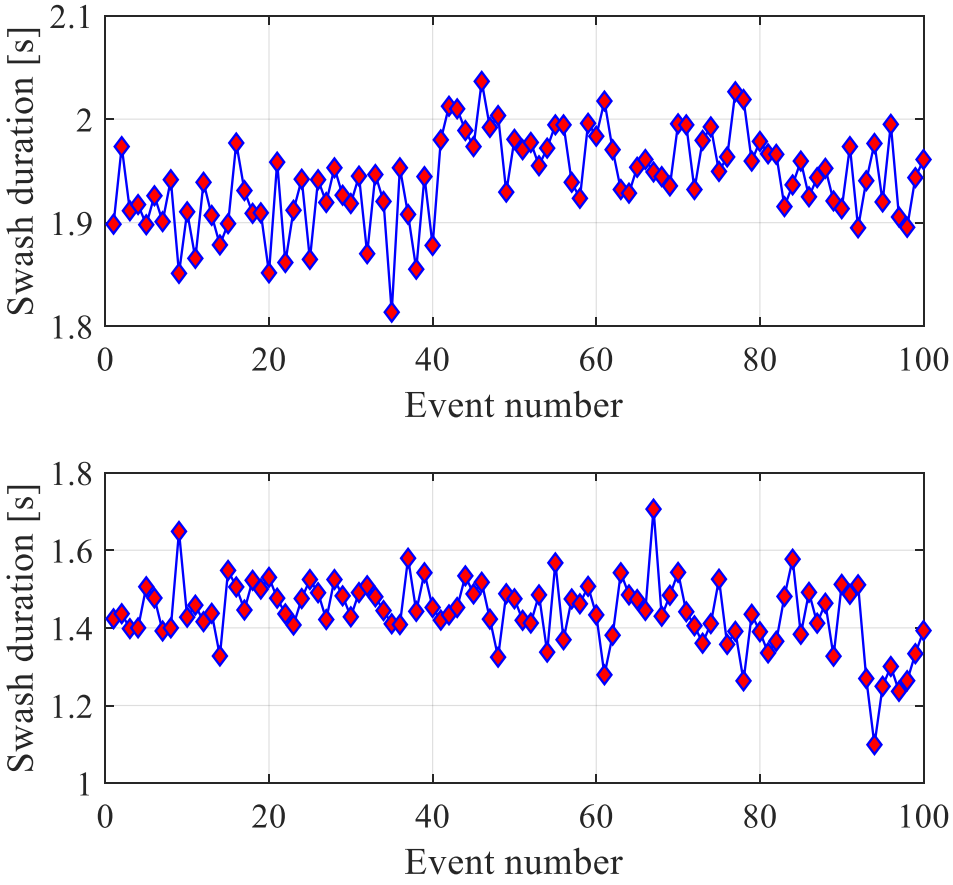

Figure 4-7 Swash duration. First panel: L1; second panel: L2.

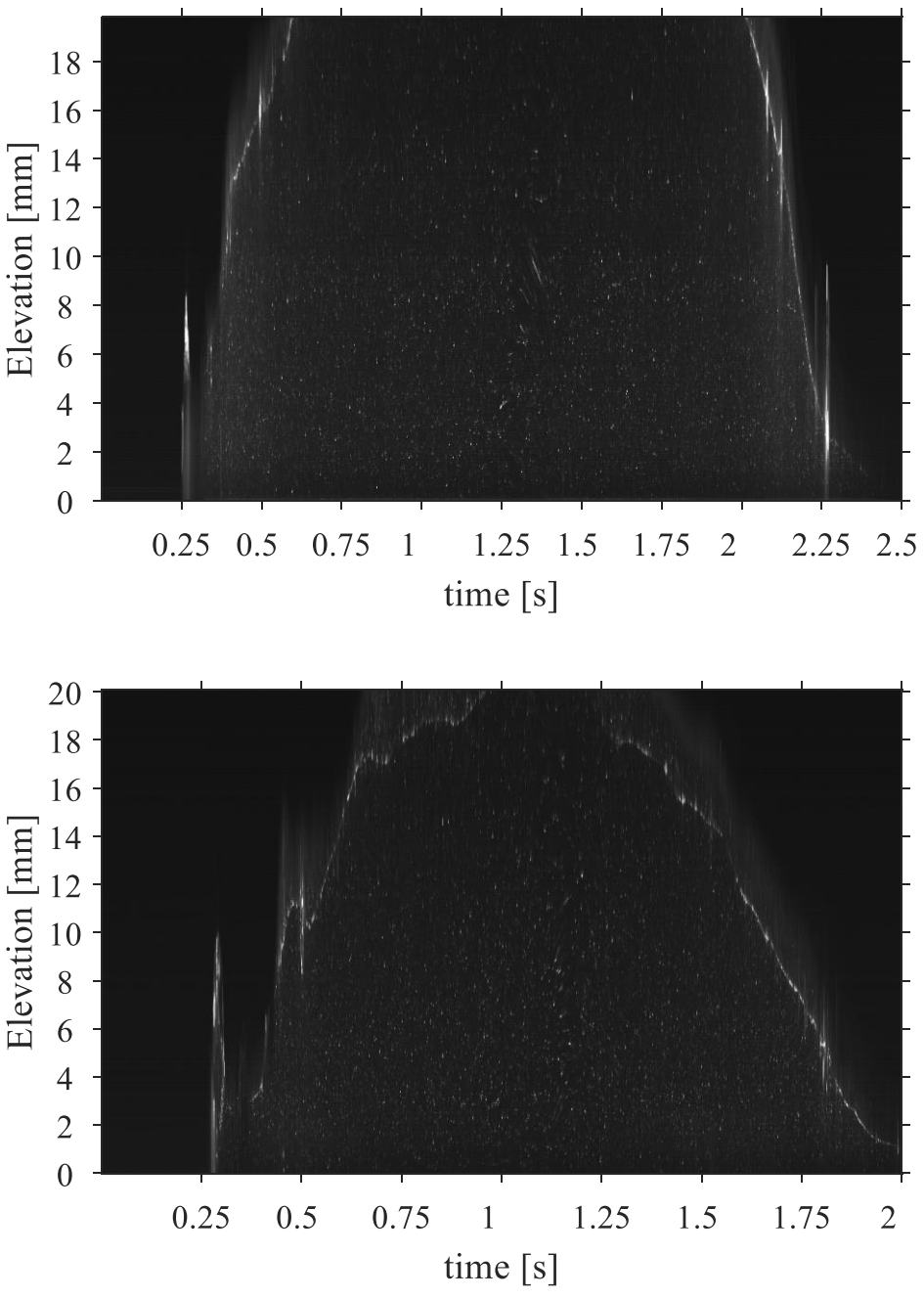

Figure 4-8 Time-stack images of an example swash event. First panel: L1; second panel: L2.

threshold value. Although optimal threshold values may vary with the image content, it may be calculated for the entire image from the grayscale median image intensity, Imedian, and its standard deviation, σI: Iclip = Imedian +nσI. The scaling factor n is user-defined and generally positive in the range $0.5 < n < 2$. In this study, n is chosen as 1. From this example shown in Figure 4-9, it is easily can be seen that the particle image intensities have been brought into a similar condition. Thus, the image intensities make equal contribution to the total cross correlation calculation.

The next step is to do PIV analysis to extract displacements of the seeding particles. To increase the spatial resolution, the accuracy and the computation speed, multiple steps and FFT-based algorithm were used in this study. In the first three steps, interrogation windows size of 96 x 32, 96 x 16, and 48 x 8 were used to calculate the displacements. The result of the former iteration was used as an offset for the next iteration. FFT-based algorithms were used in the first three steps to get rough estimation of the displacements with a high computation speed. In the final step, the interrogation window size is same with the third step, 48 x 8; however, modified FFT-based algorithm was used to accurately calculate the displacements with a moderate computation speed. The calibration factor that converts the length scale from pixel unit to real world length scale is 40 um/pixel in this study. The overlap in vertical direction is 75% with a vertical resolution of 0.08 mm. the lowest measurement point is 0.26 mm from the bottom. It is important to emphasize that in the swash zone, where vertical velocity is negligible compared with lager velocity in the stream-wise direction, the interrogation window size should be a rectangle with a larger dimension in the stream-wise direction. Although in most of the PIV analysis, square interrogation

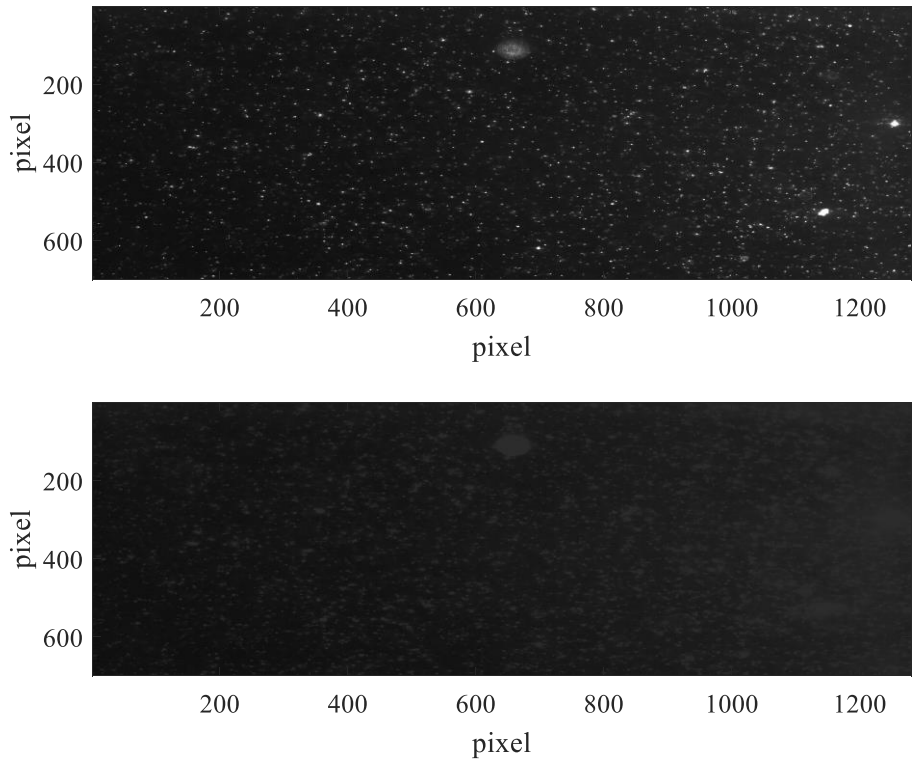

Figure 4-9 Example figures showing intensity capping method for pre-processing. First panel: raw image; second panel: intensity capped image.

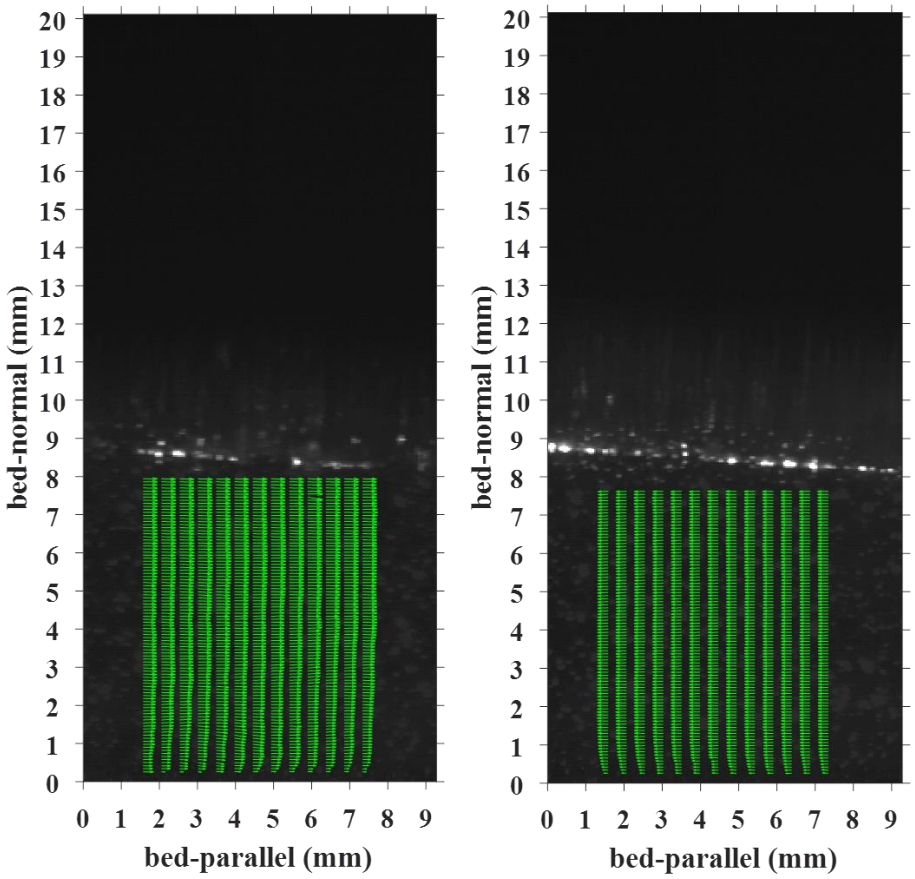

Figure 4-10 Example results of velocity vectors. Left panel: uprush; right panel: backwash.

window size is widely used, the window size should be adjusted with the corresponding measurement conditions. One of the velocity results obtained from the study is shown below. As seen from Figure 4-10, it easily can be found that the velocity information within this this bottom boundary layer is successfully captured indicated by the apparent velocity gradient close to the bed.

After getting the displacement, a certain number of obviously incorrectly determined velocity vectors (outliers) can usually be found by visual inspection of the raw data. In order to detect these incorrect data, the raw flow field data have to be validated. For this purpose, special algorithms have to be developed, which must work automatically. When the outliers are detected, means to replace these outliers must be developed. The outlier detection and replacement have been main problems for PIV development. There have been no general (universal) methods to do this work, since the experimental condition is different from case to case. So in the future, this issues will continually been the center of improving PIV. In this study, the outliers are mainly located close to the bottom due to the less concentrated seeding particles and near the surface due to the laser light reflections. It is important to note that some large natural particles such as the rubbishes in the flume affect the PIV recordings very much. For example, if one particle with diameter of 1 cm is present in the flume and enters into the field of view, then nearly half of the field of view can be occupied by this natural particle. Then this PIV recording certainly cannot give useful flow information but to make the post-processing of the detected velocity data complicated. So when conducting PIV experiments, the flume should be kept as clean as possible to exclude the effects of large natural particles. In this study, there are some large natural particles in the flume, so the outlier detection should be done at first. By

comparing the efficiency of different detection methods, the detection work was finally implemented by using the Grubbs test method, which is a statistical test used to detect outliers in a univariate data set assumed to come from a normally distributed population. Then the detected outliers were replaced by the smoothed data. The smoothing procedure was done by using the widely-used program as explained in this reference (Garcia D et al., 2010). Figure 4-11 shows the process and results of outlier detection and replacement. Once again, we emphasize that there is no universal outlier detection method, so the method used here also can overestimate or underestimate the original data. Fortunately, after outlier detection, the smoothing processing can compensate these side-effects.

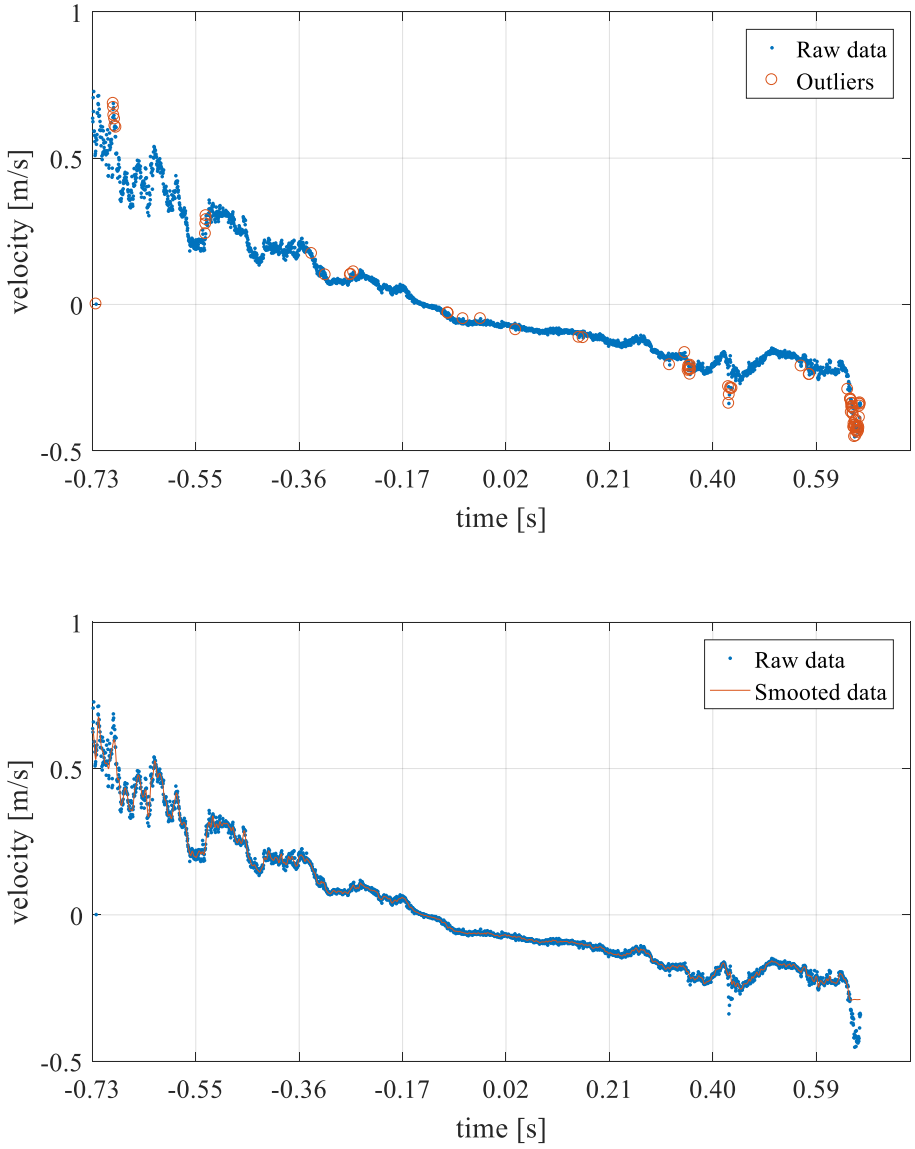

Figure 4-11 Example results of velocity vectors. Left panel: uprush; right panel: backwash.

4.4 Results

4.4.1 Velocity profile

As already stated in above, the measurements at each location were repeated for 100 runs, the ensemble averaged, bed-parallel and bed-normal velocities can be calculated by using the following equation 4-1:

$$\bar{u}(x,z,t) = \frac{1}{N}\sum_{i=1}^{N} u_i\,(x,z,t)$$

$$\bar{w}(x,z,t) = \frac{1}{N}\sum_{i=1}^{N} w_i\,(x,z,t) \qquad (4\text{-}1)$$

where $\bar{u}$ and $\bar{w}$ are the averaged bed-parallel and bed-normal velocities respectively, and u_i and w_i are instantaneous velocities. x is the measurement location, z is the elevation in respect to the bottom, t is the time.

The repeatability of the experiments also was confirmed by the wave height measured by the wave gauge installed close to the toe of the slope. As be seen from Figure 4-12, the standard deviation value is comparably small indicating acceptable repeatability. Velocity information in the swash zone is the most interesting parts since many other parameters are calculated from it. Based on the advanced PIV technique used in this study, the velocity information in this turbulent, short-duration, shallow water region has been successfully resolved. In the following, the velocity information will be analyzed from many aspects to reveal the flow structure as much as possible. In each figure, there are 13

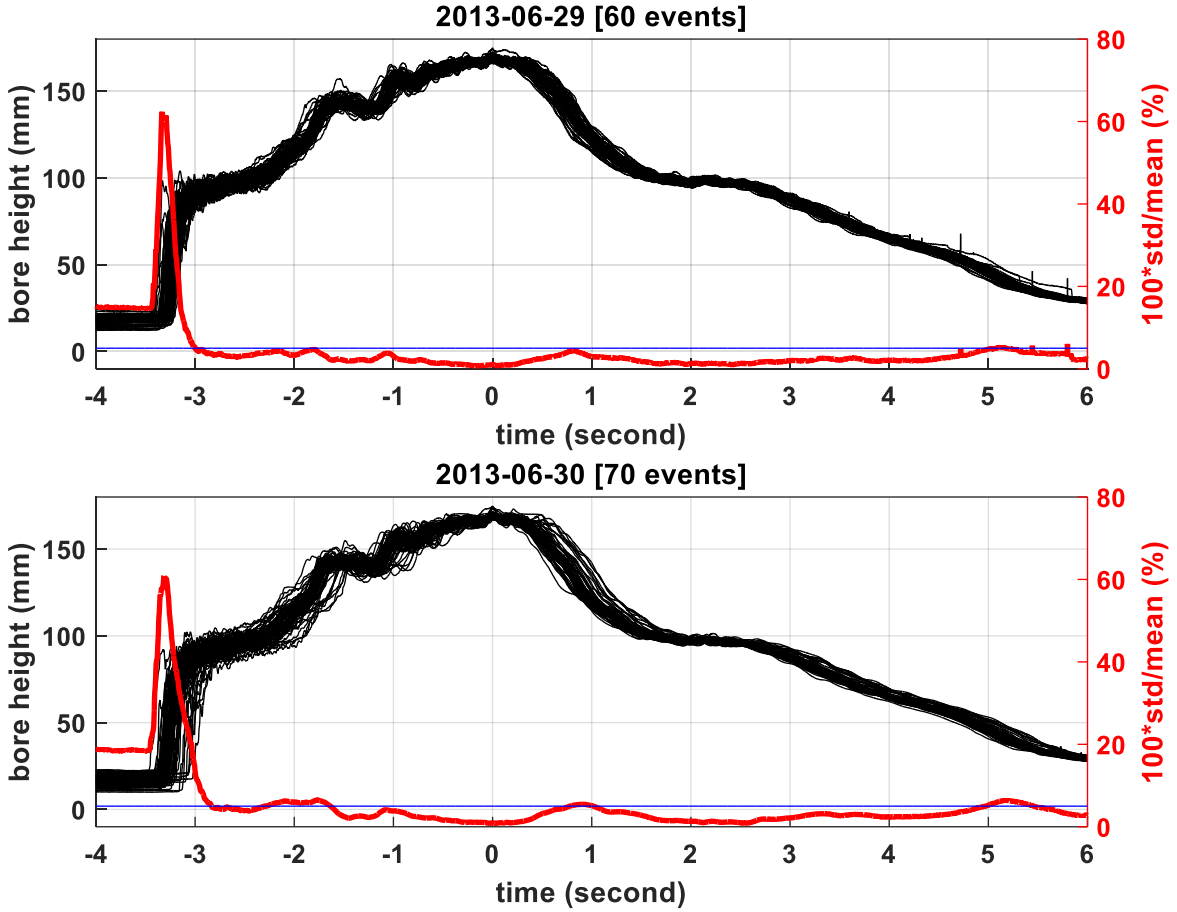

Figure 4-12 Example figures showing the implementation of the post-processing. First panel: the detected outliers; second panel: the replaced data.

columns velocity vectors. The median value of each row is chosen as the representative velocity. Figure 4-13 shows the profiles of ensemble averaged data (bed-parallel) and individual data at selected instants at location 1. The corresponding velocity profiles at location 2 are presented in Figure 4-14

The uprush duration is less than the backwash duration at these two locations indicating the asymmetry of the swash duration. It can be roughly estimated the uprush duration is about 80% of that in the backwash. It is emphasized that the real value of the uprush duration and backwash duration is longer than the measured value. The asymmetry in duration is mainly because of the strong bore collapse in the uprush and the non-exist of strong bore in the backwash. This feature can certainly have some effect on sediment transport. The measured peak velocity is larger than the measured peak backwash velocity, which is consistent with previous studies. It is sure that the real uprush velocity is not measured and it should be larger than the measured one in the current study, however, whether the real backwash velocity is measured or not is still not known. In the lower and middle swash zones, the backwash velocity usually increases firstly then reaches the maximum value, after that it begins to slow down with nearly zero at the end of backwash. So in such locations, with appropriate measurements, the maximum backwash velocity can be successfully captured. However, in the upper swash zone, whether the backwash velocity can decrease or always increases until the end is still debating. The measured peak backwash velocity is about 80% of that in the uprush. The apparent velocity gradient close to the bed indicates the presence of bottom boundary layer that has great relationship with bed shear stress. From this figure, it can be seen that the velocity gradients are very large in the early uprush, then decrease and vanish in the stage of flow reversal. From

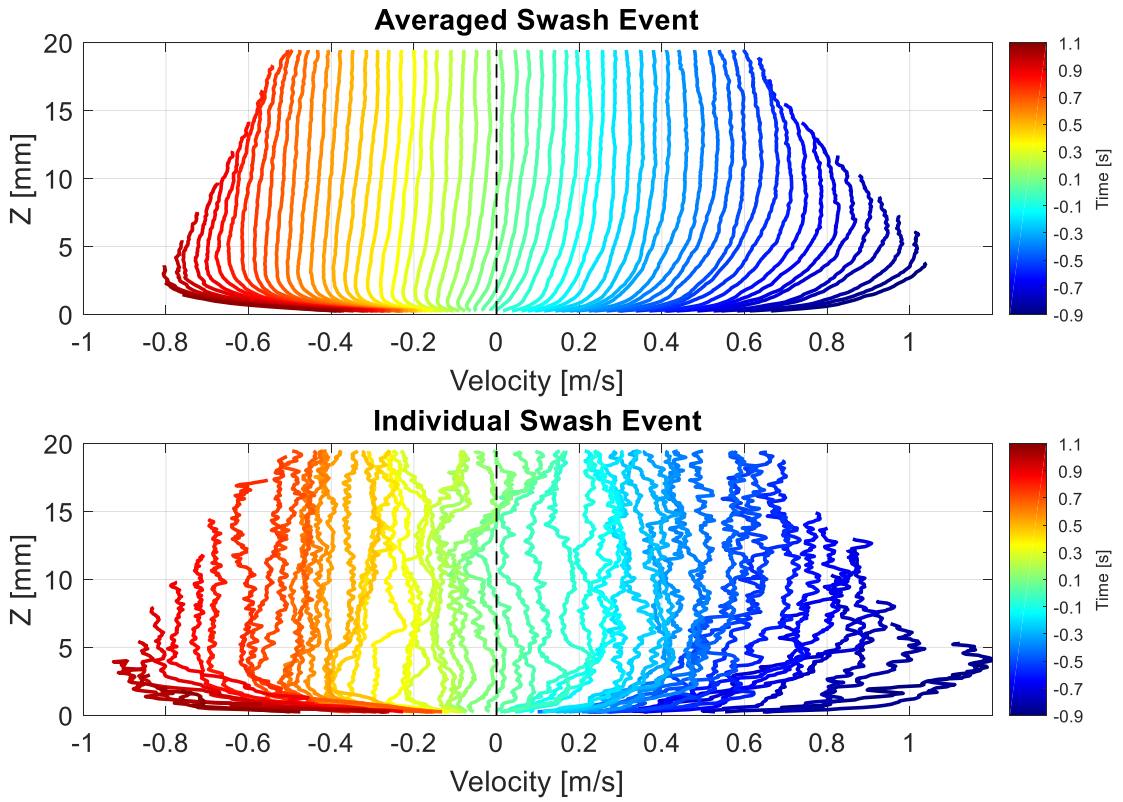

Figure 4-13 Velocity profiles at selected times at L1. First panel: averaged swash event; second panel: individual swash event.

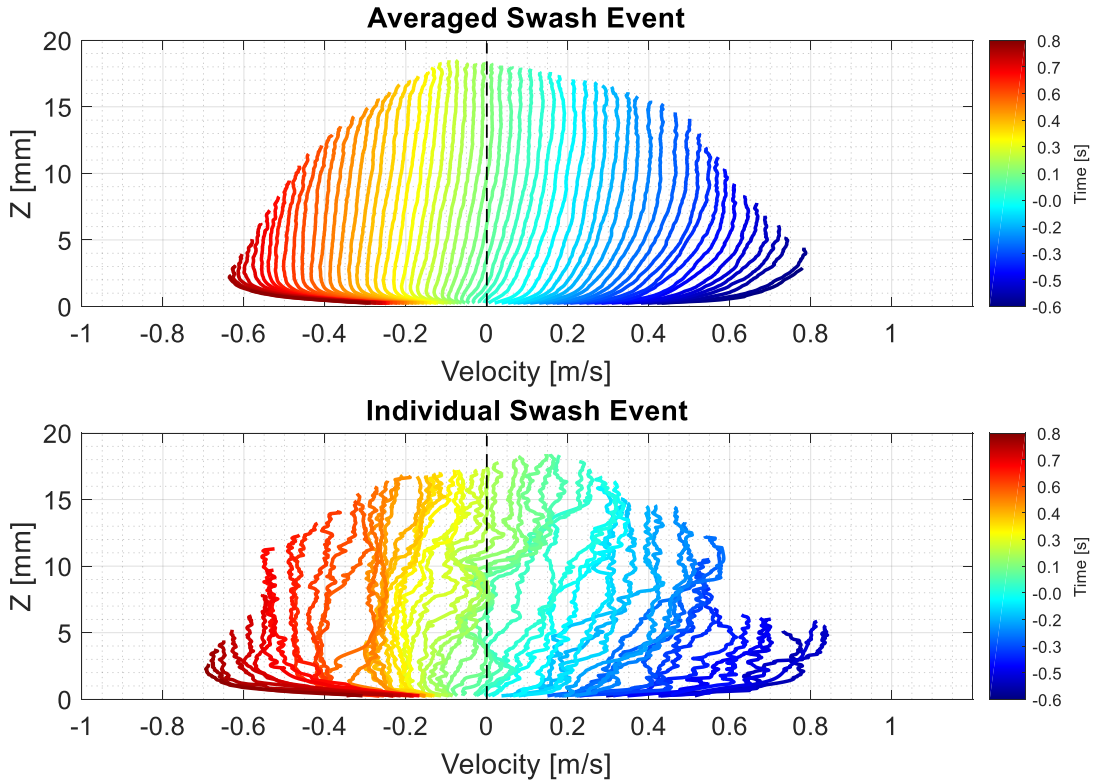

Figure 4-14 Velocity profiles at selected times at L2. First panel: averaged swash event; second panel: individual swash event.

the early backwash, they re-develop again and become thicker with confined by the shallow water depth in the late backwash.

The boundary layer thickness, which will be discussed later, has the same evolution features. For the velocity profiles, in the uprush it has a 'forward-leaning' shape with a distinct non-depth-uniform; then the velocity decreases gradually to depth-uniform; after that the phase lag phenomenon was observed that the bottom layer first changes direction to the off-shore with an on-shore direction of the flow in the top layer. From the previous studies, the phase lag phenomenon only exists for a short while after flow reversal, after that the phase lag vanishes and the top layer flow velocity becomes larger than that in the bottom layer. However, in current study, the phase lag lasts nearly for the whole backwash. One possible reason is that the measurement is made in the upper swash zone, where there is not enough time for the backwash flow to re-develop. This should be verified by future work in the upper swash zone. So far there have been not so many previous studies in upper swash zone that can be used to confirm this explanation. Another interesting characteristic is that the velocity profile shows the largest velocity in the mid-layer across the water column. Although the actual velocity in the vicinity of the surface is not successfully measured, velocity profile really shows a larger value below the surface. This feature also was reported by previous studies (Watanabe et al., 2013). This was due to different eddy structure in the bottom layer and around the top layer. In the bottom layer, the eddy structure is clockwise. However, in the top layer, it is counterclockwise. The two-contrast eddy structure leads to formation of larger velocity below the surface. Although strong fluctuations are present in the individual case, the general features of the velocity profile are

similar, indicating the feasibility of applying ensemble averaging. If using coarse-resolution measurement technique, the fluctuation may be not so strong. This is because high-resolution measurement can reveal structures of small scales thus leading to the strong fluctuations in current study.

Figure 4-15 and Figure 4-16 show the time series of the velocity profile at selected elevation near the bed from the ensemble averaging and individual view point at location 1 and location 2, respectively. These two figures can reveal the same features as shown in the previous figures. The apparent velocity gradients during the early uprush and late backwash demonstrate the existence of thick boundary layer clearly. Seen from these two figures, the velocity profiles at the same instants of different elevations show a similar tendency, indicating that the strong fluctuation is not because of measurement errors. By comparing the velocity profiles at location 1 and location 2, it can be concluded that the general features are the same with no obvious differences.

Although the bed-normal velocities are very small compared with the bed-parallel velocity, it is still useful to analyze them since they are related to the vorticity. Since the bed-normal velocities are randomly distributed at one frame, it is not appropriate to pick the median value to take as representative value. The velocity of the center column is chosen as representative velocity. The following analysis is based on the ensemble-averaging. Figure 4-17 shows the bed-normal velocity distribution at the two locations. Although the velocities are randomly distributed because the flow are strong turbulent, some features still can be found from these distributions. In the uprush, the top layer is characterized by positive (upward) velocity; the bottom layer is characterized by negative (downward)

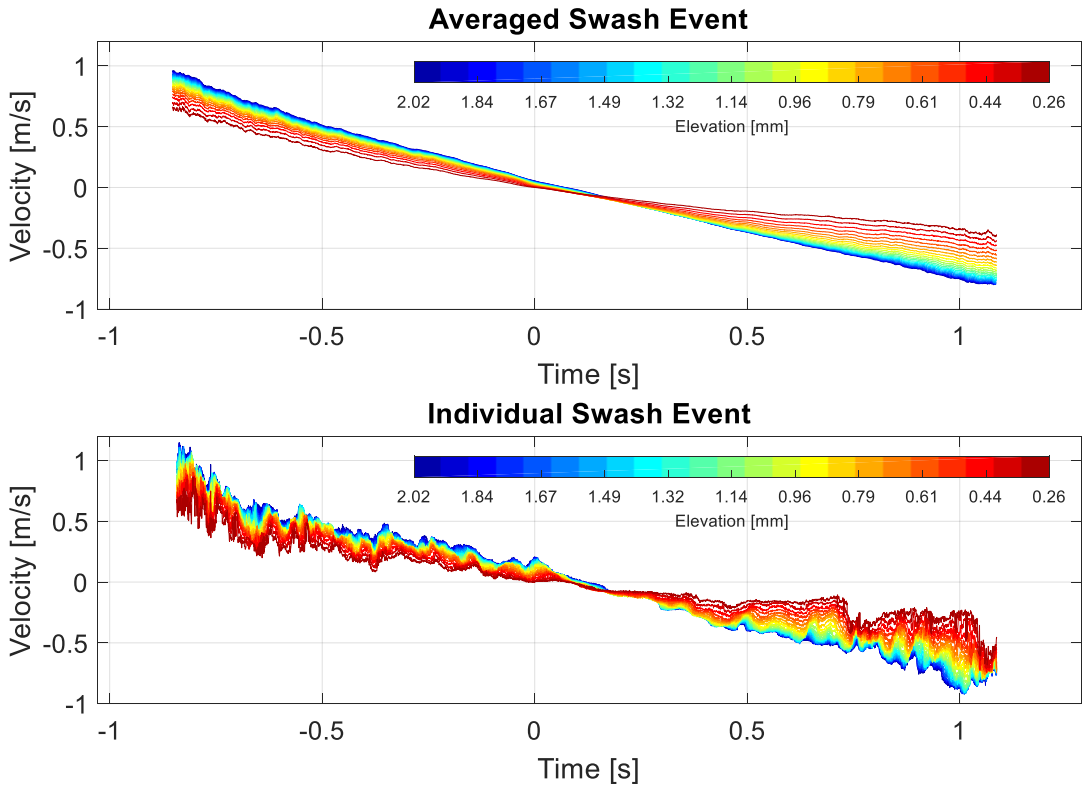

Figure 4-15 Time series of velocity at selected elevations at L1. First panel: averaged swash event; second panel: individual swash event.

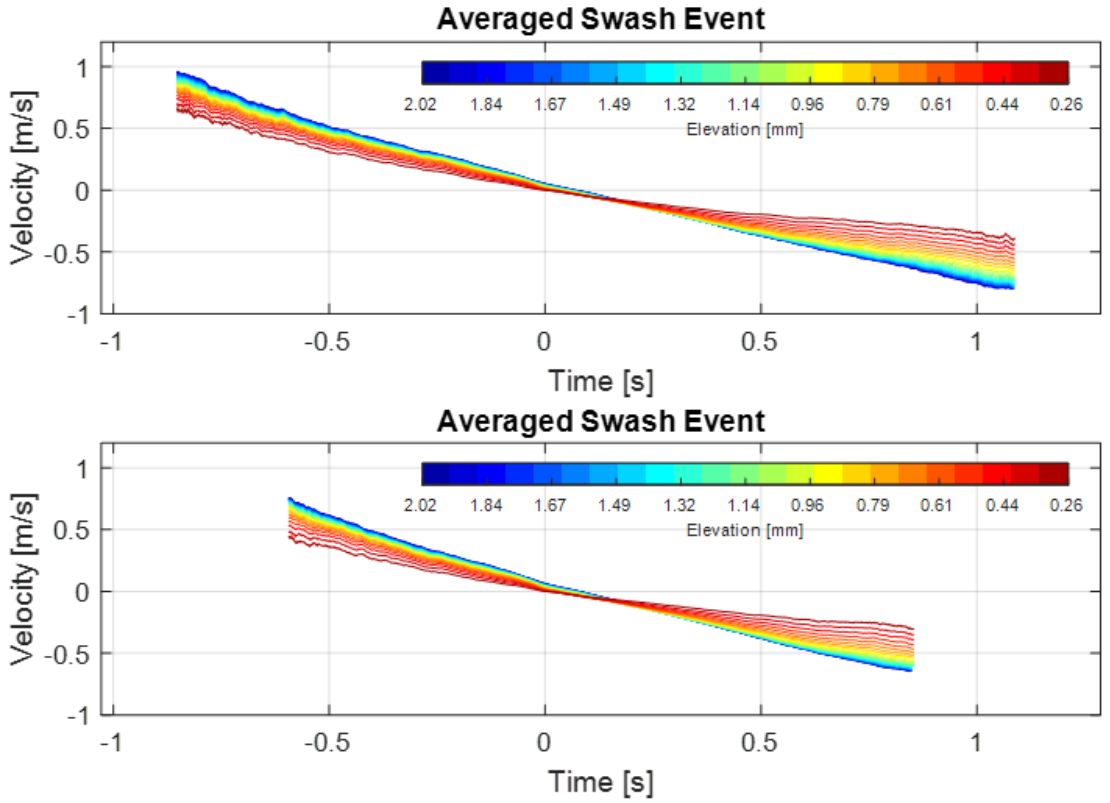

Figure 4-16 Time series of velocity at selected elevations at L2. First panel: averaged swash event; second panel: individual swash event.

velocity. This feature can make possible explanation to the bed-parallel velocity phenomenon observed in the bore front that the velocity achieves its maximum magnitude in the middle layer. As reported by previous studies, the flow in the bore front can be separated into two parts: the top layer with counterclockwise direction vorticity and the bottom layer with clockwise direction vorticity. In current study, the vorticity cannot be calculated appropriately because only 13 columns velocity vectors were calculated in one frame. However, from the bed-normal velocity distribution as shown in the above figures and observations of the PIV videos, it can be concluded that the flow in the front does depicts the tendency of counterclockwise direction vorticity in the top layer and clockwise direction vorticity in the bottom layer. During the backwash phases, the bed-normal velocities are relatively small compared with that in the uprush; this is consistent with the observations of the PIV recordings. Another reason for the small bed-normal velocities in the backwash is that the effect of bore collapse has been dissipated, so the flow is stable than that in the early uprush. It is important to note than in the backwash the bed-parallel velocity also shows the peak value in the middle layer, however, this is because of the phase lead not the different vorticity structures.

Bottom boundary layer characteristics are very important since most of the important flow processes occur here. However, because of the difficulty in measurement, the investigation of bottom boundary layer is still lacking. The first problem when discussing bottom boundary layer is the definition of bottom boundary layer thickness. In the surf zone, there are several kinds of formulations used to estimate the bottom boundary layer thickness. However, because of the strong turbulent flow feature, the definition in the swash zone is

still unclear. In the numerical simulation studies, usually the velocity has been assumed to have a logarithmic profile and the boundary layer thickness is defined by the distance from bottom to the elevation where the free stream is reached. However, whether the velocity profile has a logarithmic profile in the swash zone is still debating. In the field and laboratory studies, there are no quantitative formulations to calculate the boundary layer thickness. In recent studies, the thickness is estimated based on the velocity gradient as presented in this reference (Ruju et al., 2016). However, the bottom boundary layer thickness is not successfully captured during the uprush. This is because of the strong turbulence level and remove of the outliers of the ADV velocity data. In current study, the same method is employed to evaluate the bottom boundary layer thickness. The results are presented in Figure 4-18. Compared with previous studies, the bottom boundary layer thickness can be successfully captured both in the uprush and in the backwash phases. The thickness firstly is initiated by the incident swash bore and is limited by the shallow water depth. After that, it increases for a short while, and then begins to decrease, with a near-zero value around flow reversal. Then it redevelops again in the backwash phase and reaches the maximum value in the late backwash and becomes limited by the shallow water depth again. The two locations show a similar tendency. However, for the previous studies, the evolution of the bottom boundary thickness is a little different from the current study. In the previous studies, the bottom boundary layer thickness is estimated to be bounded by the water depth almost in the entire swash phases except that around the flow reversal the thickness is zero. Although, it is not easy to conclude which estimation is more appropriate, it should be noted that the bottom boundary layer should be the layer that is affected by the bottom characteristics

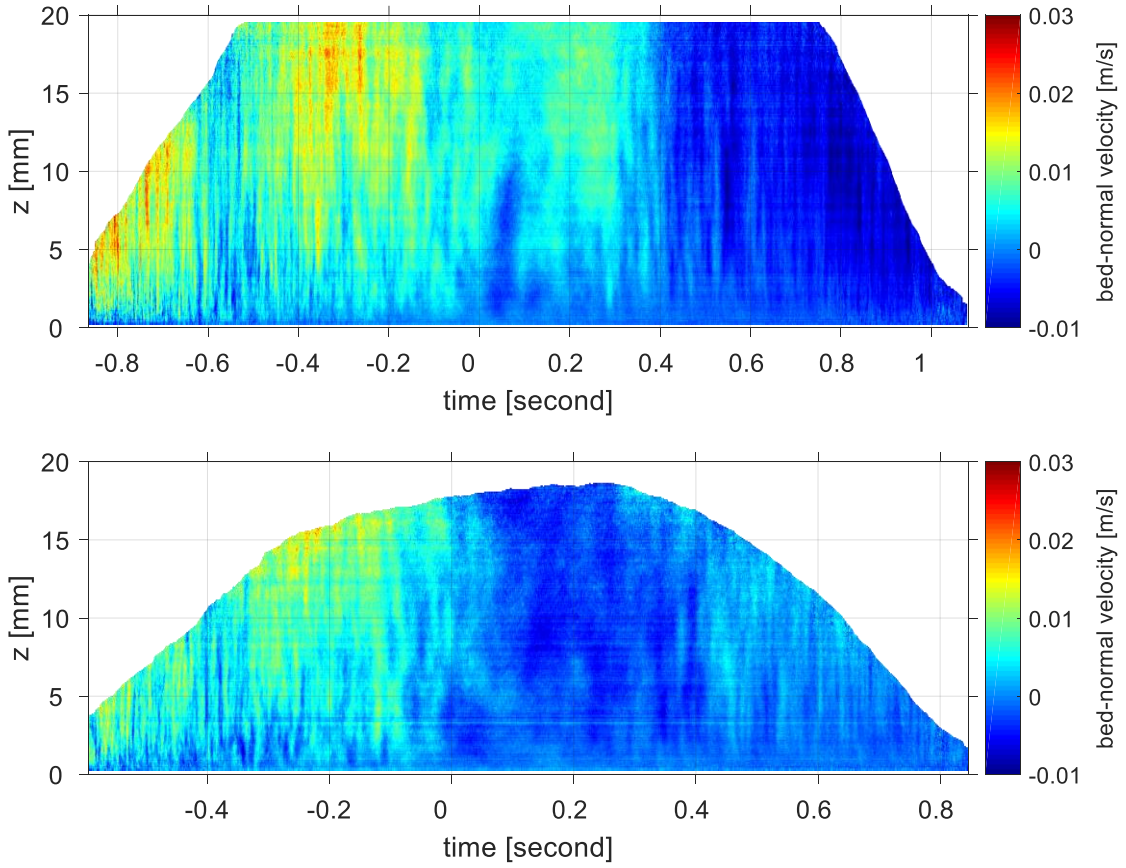

Figure 4-17 Bed-normal velocity distribution. First panel: L1; second panel: L2.

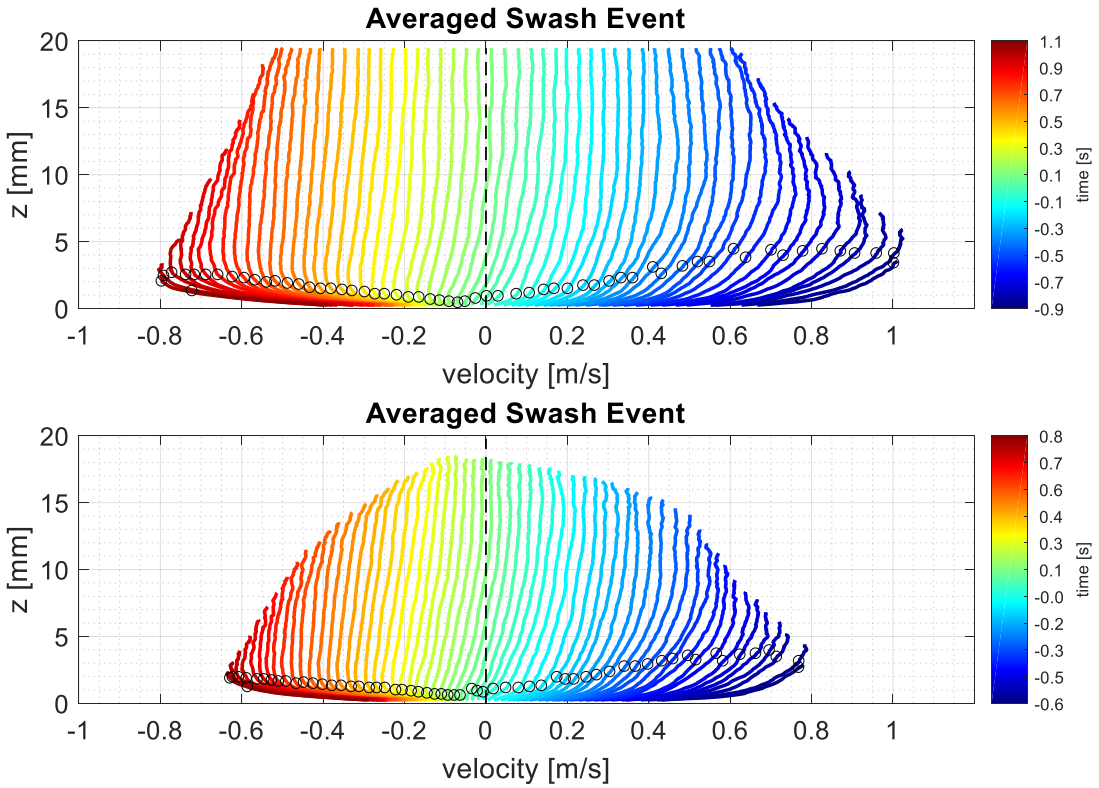

Figure 4-18 Bottom boundary layer thickness estimation. First panel: L1; second panel: L2.

and the effect made by the instable surface should not be taken into consideration. One possible reason for the thick boundary layer of the previous studies may steam from that the effects of surface also are included.

4.4.2 Turbulence evolution

Ensemble averaging method

Given the acceptable repeatability of the experiments, the turbulence was estimated using ensemble averaging method. It has been shown that the bed-normal velocity is relatively small compared with the bed-parallel velocity. So in this study, the turbulence was calculated based the bed-parallel velocity without bed-normal velocity. The turbulence was estimated using the following in equation 4-2 and equation 4-3:

$$u_i'(x,z,t) = u_i(x,z,t) - \bar{u}(x,z,t) \quad (4\text{-}2)$$

$$u_{TKE} = \overline{u'u'}(x,z,t) = \frac{1}{N}\sum_{i=1}^{N} u_i'u_i'(x,z,t) \quad (4\text{-}3)$$

where u_i' is the turbulent velocity fluctuation for runi of the experiment, u_{TKE} is the turbulent kinematic energy. In this study, $N = 100$.

The results for the two locations are presented in Figure 4-19. The turbulence level is comparable with previous studies under similar experimental conditions indicating that the data in this study is reliable. As expected, the turbulence level

is high when the corresponding mean velocity is high. For example, the turbulence level during the early uprush and late backwash are higher at location 1 than that at location 2. At location 1, during the early uprush phases, the turbulence shows peak value in the middle layer revealing the fact that the surface turbulence is transported downward and the bed-generated turbulence is transported upward. During the late backwash, the turbulence level is only strong near the bed. This can be explained by the fact that, the bore-generated turbulence has been dissipated during the total run-up, and in the late backwash the turbulence is due to the bed-generated and surface fluctuation generated turbulence. However, at location 2 the late backwash velocity is still large producing relative stronger turbulence than that induced by the surface fluctuation. At location 2, the turbulence level is strong near the bed both during the early uprush. This is because of the large uprush velocity gradient close to the bed and the absence of the bore-induced turbulence. However, in the late backwash, the turbulence also is high in the vicinity of the surface. This can be explained by the fact that location 2 is located far landward and close to the run-up limit; the water surface has not been stable from the run-up limit to location 2. The surface fluctuation generated turbulence also makes similar contribution to the total turbulence level as that made by the bed. During the flow reversal, the turbulence level is very weak mainly because of the small velocity magnitude. The depth-averaged ensemble averaged TKE is shown in figure 4-20. As depicted, the peak uprush TKE is stronger than that in the backwash for both locations with reasons has been discussed in the above. As expected, the turbulence level for location 2 is less than that for location 1 because of the decreasing velocity and absence of the bore-generated turbulence.

Moving averaging method

The high sampling rate of this study offers the possibility to apply moving average to derive the turbulent component. The moving averaging estimation is based on the following equation from equation 4-4 to equation 4-7:

$$\widehat{u_i} = \frac{1}{M} \sum_{dt=-\frac{M}{2}}^{dt=\frac{M}{2}} u(x, z, t + dt) \qquad (4\text{-}4)$$

$$u_i'(x, z, t) = u_i(x, z, t) - \widehat{u_i}(x, z, t) \qquad (4\text{-}5)$$

$$u_{i-TKE}' = u_i' u_i'(x, z, t) \qquad (4\text{-}6)$$

$$u_{TKE} = \frac{1}{N} \sum_{n=1}^{N} u_{i-TKE}' \qquad (4\text{-}7)$$

Moving average also has the disadvantage that it is difficult to definitely determine the cut-off frequency or the moving average time, because the spectral velocity components as mean flow and turbulent flow are mutually superimposed in a range of the frequency domain. There is no general method that can be

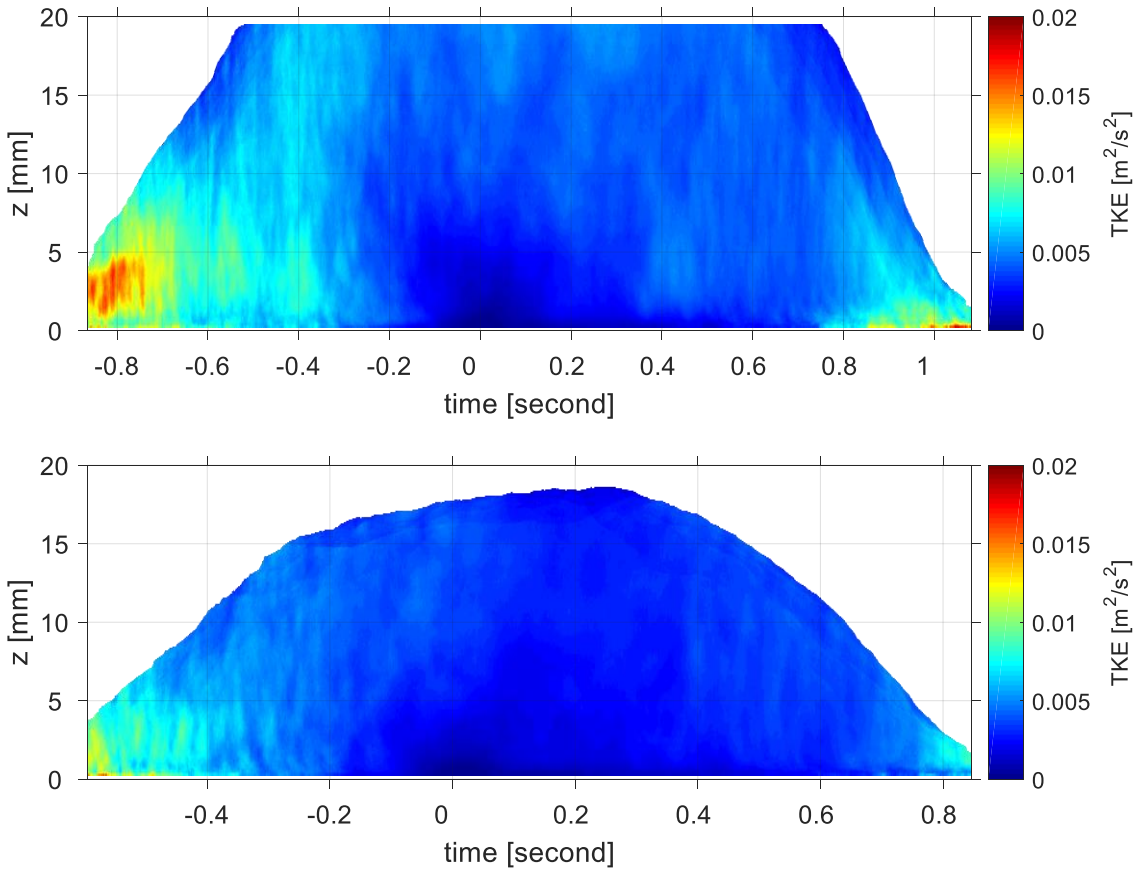

Figure 4-19 TKE_EA distribution. First panel: L1; second panel: L2.

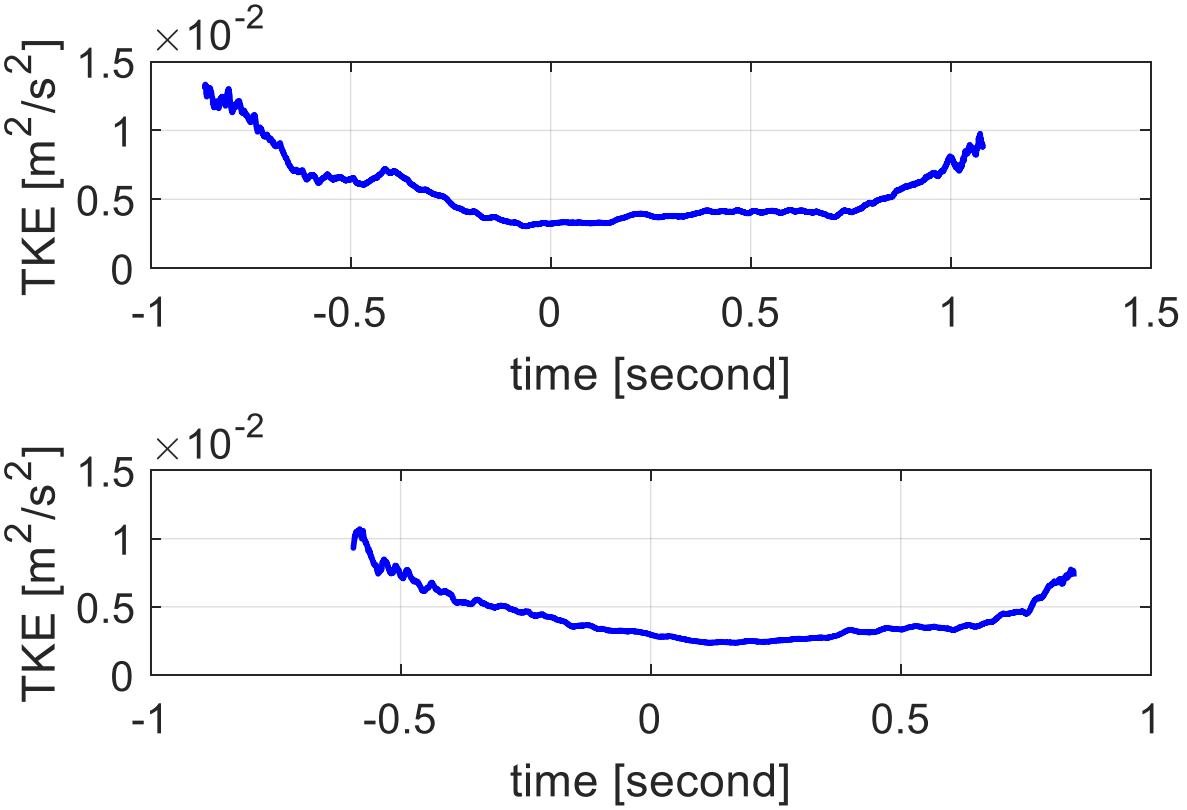

Figure 4-20 Time series of depth-averaged TKE. First panel: L1; second panel: L2.

employed to decide the moving average time window; although many previous studies employed the power spectral density and -5/3 law to decide the threshold. So in this study, the concentration is not focused on the decision of the cut-off threshold but on the results obtained by several cut-off thresholds based on the assumption that the real turbulent components should be located in some where among these results. Or at least the tendency of the real turbulent component should be similar to that as depicted by these results of different cut-off thresholds. The other purpose of using moving average is to check whether the ensemble averaging method is suitable when using in the swash zone. If results obtained by these two methods show similar tendency, then conclusions can be made with much confidence that both the ensemble averaging and moving averaging can be applied in the swash zone turbulence decomposition.

The TKE results for location 1 obtained by setting the moving window to 100/2000 s, 200/2000 s, 300/2000 s, 400/2000 s were shown in Figure 4-21. These moving window sizes correspond to the cut-off frequency of 20 Hz, 10 Hz, 6.6 Hz and 5 Hz, respectively, which means the flow motion under these frequencies, are decided as turbulent components. As depicted by Figure 4-21, the TKE shows similar tendency for all the cut-off frequencies and differs for the TKE level. As expected, the TKE is level is larger for the low cut-off frequency and the upper layer TKE also becomes apparent when low cut-off frequency is used. Different from the results from ensemble averaging, the upper layer TKE in the early uprush and late backwash phases are both not comparable to that in the bottom. The results of moving average should be more appropriate since the calculation is based on the local time series of the flow velocity, which is different from that in the ensemble averaging that the results heavily depend on the performance of

repeatability of the experimental conditions. As can be seen from Figure 4-22, the results for location 2 also present a similar tendency to that for location 1, which improves the confidence of the TKE results. In fact, by checking the instantaneous velocity distribution, it has been shown that the velocity fluctuation in the upper layer is relatively small compared with that in the bottom. Another feature is the high TKE level in the uprush and low TKE level in the backwash level. Reasons for this phenomenon have been stated in the previous sections that the backwash velocity is smaller than the uprush velocity. To compare the results from the view of depth averaged value, the depth-averaged results for the two locations with the 4 cut-off frequencies are presented in Figure 4-23 and 4-24. For both locations, the depth-averaged results show a higher TKE level in early uprush phases and relative weak level in late backwash phases. The difference between TKE levels in these two phases is larger in location 2 with a ratio of 3 between the uprush and backwash peak TKE level. The ratio is between 1 and 2 for location 1. The possible explanation is that there is no enough time for the backwash flow to develop for location 2 with shallow water depth and small peak late backwash velocity leading to relatively weak TKE level. Derived from the depth-averaged figures, the TKE levels for location 1 and 2 are similar with a little large value for location 1. This should be due to the short distance between the two locations. However, the depth-averaged results obtained using ensemble average and moving average differ so much with an order larger in the ensemble average TKE calculation. Although as discussed in many previous studies, ensemble average is a standard and accurate method for evaluating turbulence in the regular wave condition, the application in the swash zone still needs further investigation because of the strong irregularity in

this turbulent area. At least the ensemble average method can overestimate the TKE level since perfect repeatability usually cannot be achieved in the dam-break case. What's more, in this study, the measurements were conducted in the upper swash zone with extreme shallow water depth, where little fluctuation can lead to serious bias of the results. So the result of moving average is more reasonable and the moving average method seems to be promising in the turbulence decomposition especially in the swash zone with difficulty in applying ensemble averaging method.

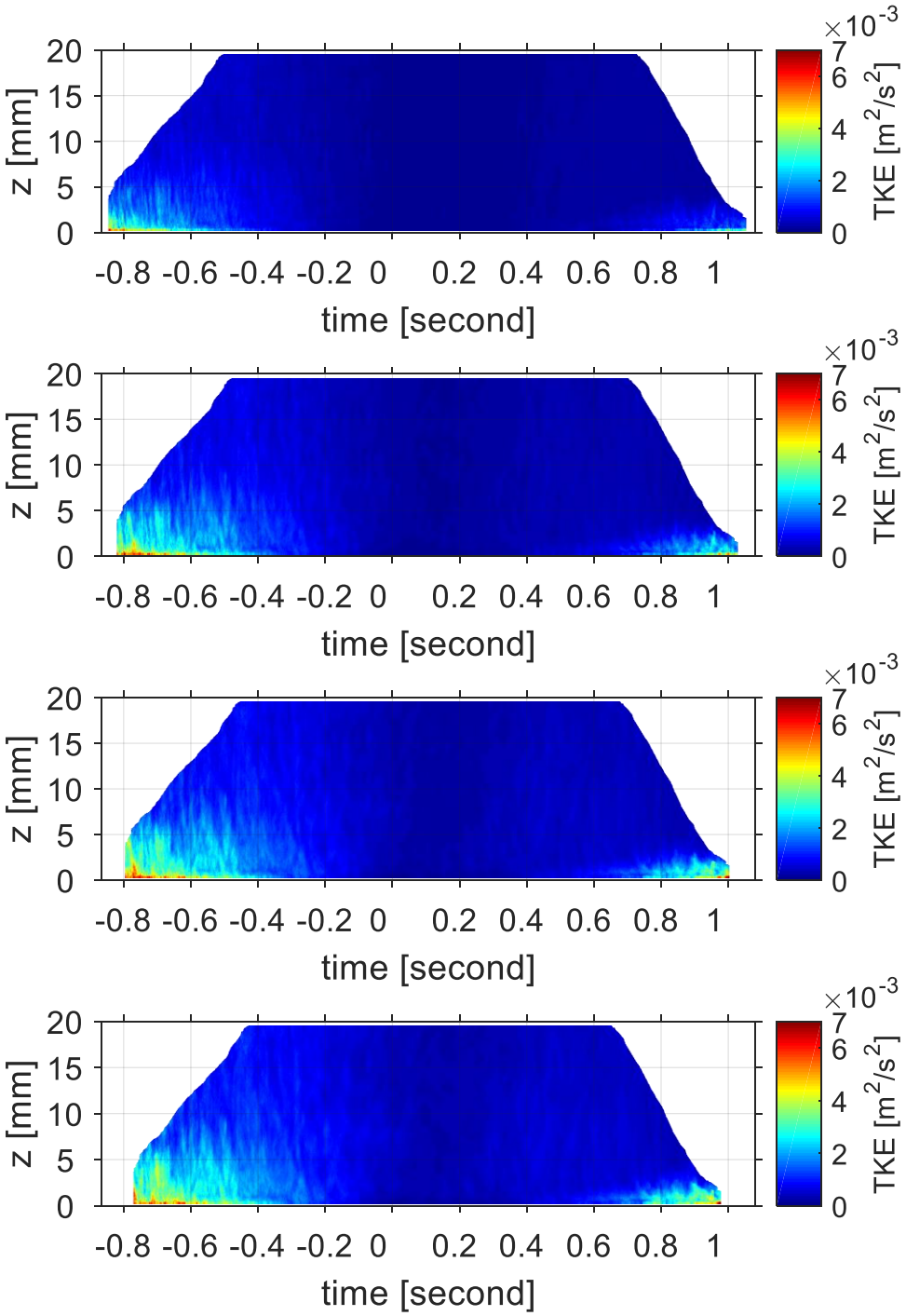

Figure 4-21 TKE distribution using four cut-off frequencies at L1. From the first panel to the last panel: 20 Hz, 10 Hz, 6.6 Hz, 5 Hz.

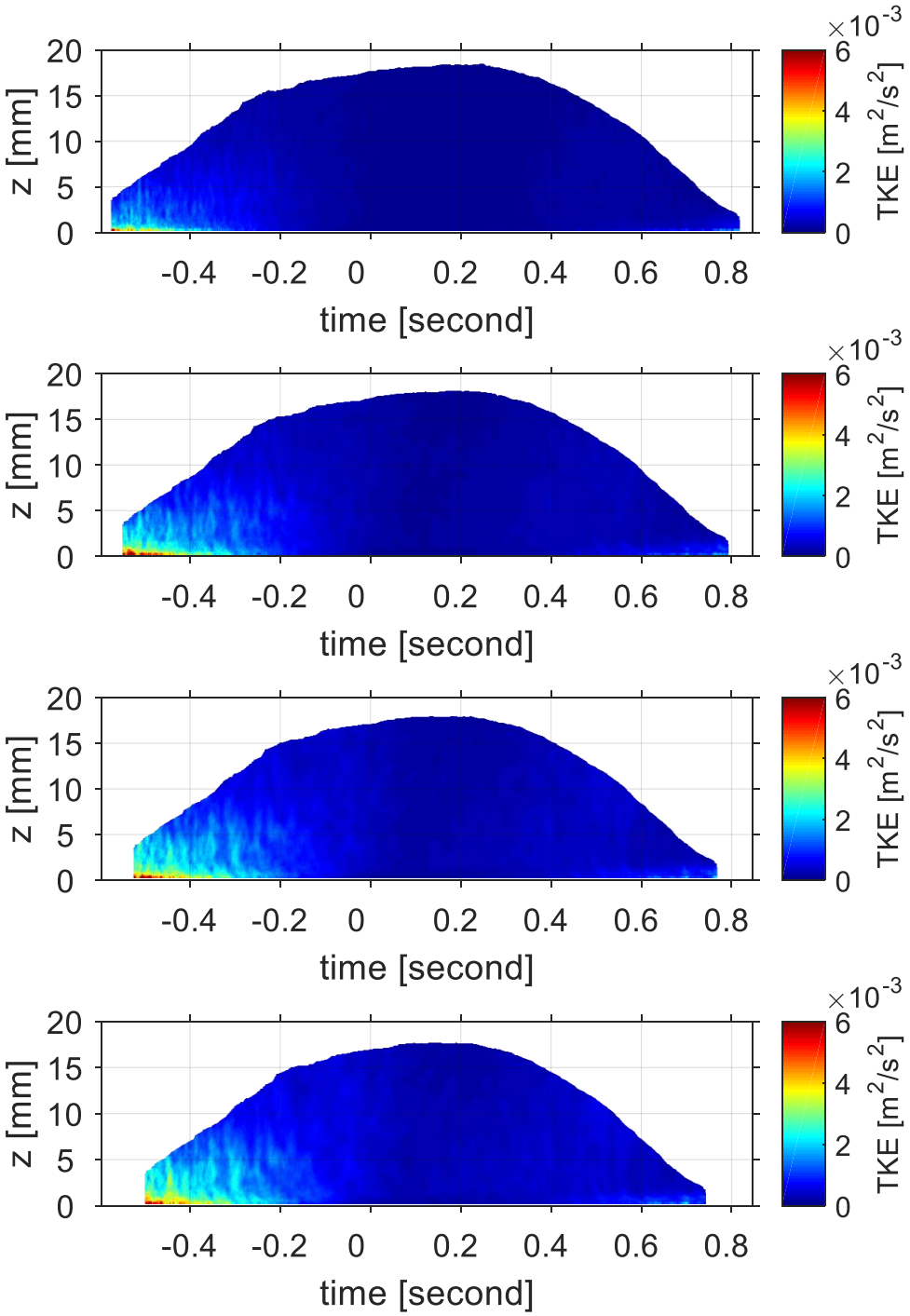

Figure 4-22 TKE distribution using four cut-off frequencies at L2. From the First panel to the last panel: 20 Hz, 10 Hz, 6.6 Hz, 5 Hz.

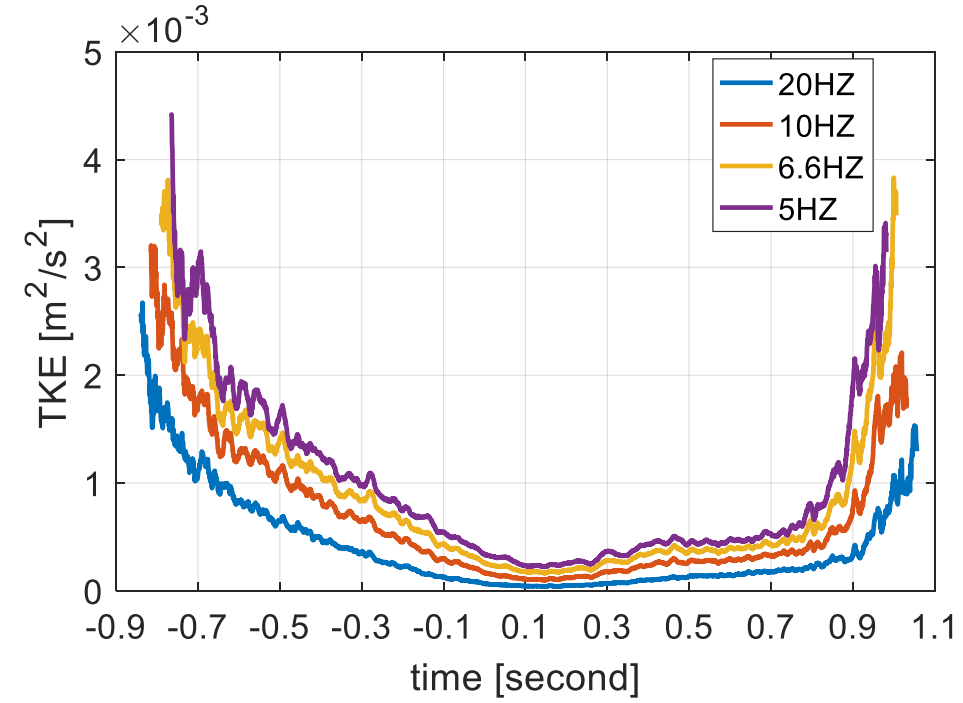

Figure 4-23 Time series of depth-averaged TKE for 4 frequencies at L1.

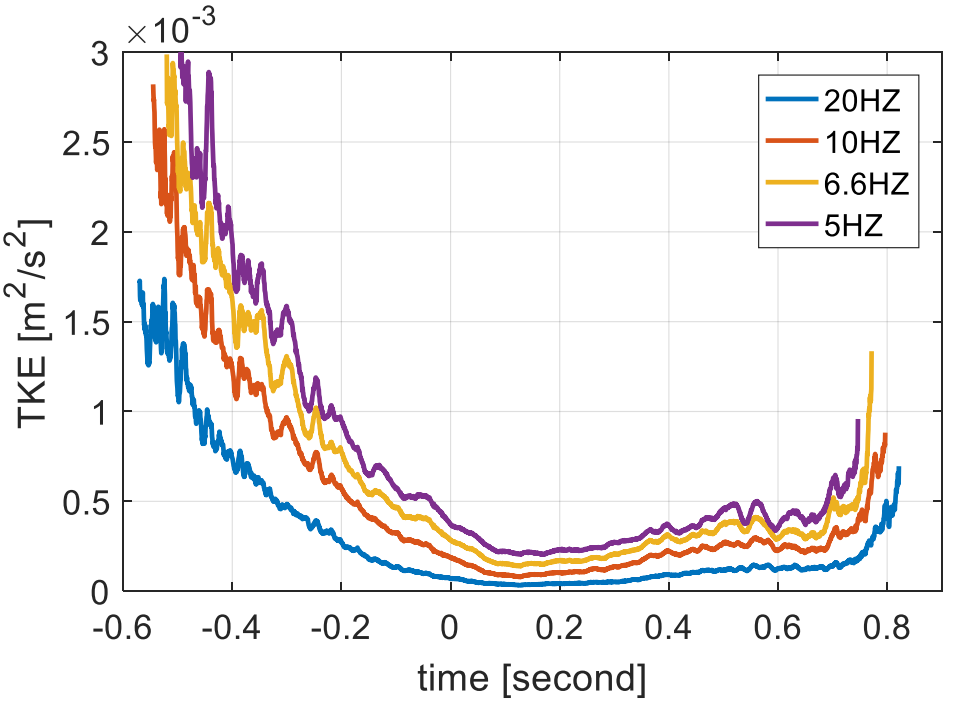

Figure 4-24 Time series of depth-averaged TKE for 4 frequencies at L2.

4.4.3 Bed shear stress estimation

The momentum integral method

In the case of horizontal uniform flow, the momentum conservation equations for the boundary layer can be written as follows:

$$\rho \frac{\partial u}{\partial t} = -\frac{\partial p}{\partial x} + \frac{\partial \tau}{\partial z} \quad (4\text{-}8)$$

$$\frac{\partial p}{\partial z} = -\rho g \quad (4\text{-}9)$$

where u is the horizontal velocity, t is the time, p is the pressure, τ is the shear stress, g is the gravitational acceleration, and ρ is the water density. The two equations imply that inside the boundary layer, the pressure is hydrostatic, and the longitudinal pressure gradient $\partial p/\partial x$ is constant across the boundary layer thickness. By assuming that the shear stress vanishes outside the boundary layer, it is possible to write the horizontal momentum equation on the top of the boundary layer as

$$\frac{\partial p}{\partial x} = -\rho \frac{\partial U_0}{\partial t} \quad (4\text{-}10)$$

where U_0 represent the free stream velocity. By combining these equations, the defect velocity law (Fredsøe and Deigaard, 1992; Nielsen, 1992) describing the evolution of the boundary layer is obtained:

$$\rho \frac{\partial}{\partial x}(U_0 - u) = -\frac{\partial \tau}{\partial z} \quad (4\text{-}11)$$

The bed shear stress τ_b can be obtained by integrating this equation across the boundary layer thickness δ:

$$\tau_b = \rho(\delta \frac{\partial U_0}{\partial t} - \int_{z_0}^{z_0+\delta} \frac{\partial u}{\partial t} dz) \quad (4\text{-}12)$$

Two main assumptions are involved in the derivation of the above equations from the general momentum conservation equations. The first assumption concerns the flow uniformity leading to negligible advection terms and dynamic pressure in the boundary layer. A zero shear stress at the top of the boundary layer represents the second assumption. It is need to note that in the swash zone, the boundary layer thickness is not much smaller than the water depth h (Puleo and Holland, 2001). In case the boundary layer covers the entire swash depth, the assumption of $u(h) = U_0$ is considered (Briganti et al., 2011).

The linear fitting method

It has been studied that when the flow regime is laminar, the bed shear stress can be calculated using the following equation 4-13:

$$\tau_b = \rho \nu \left.\frac{\partial u}{\partial z}\right|_{z=z_b} \quad (4\text{-}13)$$

where τ_b is the bottom shear stress, ρ is the fluid density, u is the horizontal velocity, z_b is the bottom elevation with respect to an arbitrary horizontal datum

and ν is the kinetic viscosity. Hence, the bottom shear stress can be estimated from the vertical velocity gradient near the bottom.

The logarithmic model method

In the case of a hydraulically rough bed, the law of the wall prescribes that a logarithmic-shaped horizontal velocity profile $u(z)$ develops inside the boundary layer:

$$u(z) = \frac{U_f}{\kappa} \ln\left(\frac{z}{z_0}\right) \qquad (4\text{-}14)$$

where k is the von Karman constant (0.40) and z_0 is the height above the bed at which the velocity is assumed to be zero. Following Nikuradse (1932), z_0 is equal to $k_N/30$, k_N being the bed roughness. Finally, U_f is the friction velocity defined as

$$U_f = \sqrt{\frac{\tau_b}{\rho}} \qquad (4\text{-}15)$$

where τ_b is the bed shear stress and ρ is the water density. The equation was originally derived for steady flows assuming that shear stresses are constant close to the bottom. These assumptions, on which the law of the wall relies, restrict its theoretical validity to a region whose vertical extent above the bottom depends on the non-dimensional elevation z^+ defined as

$$z^+ = \frac{U_f}{\nu} \qquad (4\text{-}16)$$

where ν is the kinematic viscosity ($\nu = 10^{-6} m^2/s$). According to Pope (2000) and Wei and Willmart (1989), the law of the wall holds for $30 < z^+ < 1200$. However, experimental work has found good agreement between observed and predicted data well beyond the range of applicability of the logarithmic model.

The concept of friction factor f has been introduced in order to relate the free stream horizontal velocity U_0 to the bed shear stress by means of

$$\tau_b = \frac{1}{2}\rho f |U_0| U_0 \qquad (4\text{-}17)$$

When velocity profile information is not available, the bed stress τ_b is estimated through the above equation 4-17, also known as the quadratic drag law, by introducing an empirical value of f. For instances in which velocity profile measurements are available, f can be estimated as

$$f = \frac{2\tau_b}{\rho |U_0| U_0} \qquad (4\text{-}18)$$

For the linear fitting method, in this study, velocity profile is fitted linearly within the lowest 5 points measurements points, which corresponds to an elevation of 0.58 mm. The momentum integral method is applied to the bottom boundary layer thickness that has been calculated above using the velocity gradient threshold. The bed shear stress results obtained using the two methods are presented in the Figure 4-25. The momentum method shows almost all negative values during both the uprush and backwash phases with only portion of the backwash flow shows positive values. This strange tendency is much related to the calculation of the bed shear stress using numerical differencing of the PIV

velocity data, which certainly produces great uncertainty. Momentum method also is tested by previous studies conducted in the swash zone and similar results were obtained. The discrepancies are largely related to the velocity data quality and the assumption of the applicability of the method. As has been shown above, the method is only valid for the uniform and steady flow. Because of the unreliable estimation results, the bed shear stress results of momentum method will not be further analyzed in the following. As for the linear fitting method, one advantage is that it is easy to be applied in the measurement. However, it should be noted that the linear fitting is only valid for laminar flow, which is not the case in the swash zone, where strong turbulent flow always exist the swash duration. However, the results of linear fitting also can give show some information of bed shear stress. As seen from the results, the large velocity gradients in the early uprush and late backwash result in high bed shear stress compared with that during the flow reversal stage. And the measured peak uprush velocity is smaller than that of the backwash. Here it is to note that, the actual value of peak uprush and backwash bed shear stress is not measure because of the difficulty in measuring velocity field during these stages with many air bubbles and strong turbulence. Although the linear fitting method can reveal the general tendency of the bed shear stress, the detailed distribution of bed shear stress cannot be fully studied using this method.

Logarithmic model method also known as log law method has been widely used under different flow conditions from the uniform steady flow to turbulent flow. In theory, in fluid dynamics, the law of the wall states that the average velocity of a turbulent flow at a certain point is proportional to the logarithm of the distance from that point to the "wall", or the boundary of the fluid region. This law of the

wall was first published by Theodore von Kármán, in 1930. It is only technically applicable to parts of the flow that are close to the wall (<20% of the height of the flow), though it is a good approximation for the entire velocity profile of natural streams. When talking about log law method, the most important issue is to decide the elevation that under which the log law is applied. So far there are no universal conclusions to decide that elevation. In practice, many different ways were adopted to decide the elevation: 1) the elevation that measurement data is available; 2) the elevation that whole water depth; 3) the elevation that when the square of correlation coefficient is larger than a threshold, usually R^2 >0.95 for the laboratory experiment and R^2 >0.8 for the field investigation. The decision of this elevation depends on the accuracy that needed. For instance, in the swash zone study, when applying log law to estimate bed shear stress, the elevation should be chose carefully. Since little errors in the elevation determination can lead to large errors in the bed shear stress results which will be shown in the following section.

In most of the previous studies, the correlation coefficient of fitting between the measured velocity profile and log profile is adopted to decide the upper limit of the fitting elevation. However, as seen from Figure 4-26, it is easy to find that, when fitting the measured velocity profile using different elevations, the corresponding correlation coefficients are almost all larger than 0.95, which means that the fitting limit elevation cannot be singly decided by using the correlation coefficient. And it is important to note that although the correlation coefficients are larger, the corresponding fitting slope is different from one fitting elevation to another. Another condition is that the non-dimensional wall unit should be around from 30 to 1200. However, the wall unit must be calculated from

the friction velocity, which has to be calculated from the log law. So the circular effect occurs, which makes it difficult to directly using wall unit to check the fitting limit elevation. However, regardless whether the fitting limit elevation is appropriate, we can just calculate the friction velocity using log law based on the assumption that this layer just is within the log layer. Then the resulting friction velocity can be used to back-calculate the wall unit. If the wall unit is out of the range, then it must be that the fitting limit elevation is not appropriate. On the contrast, if the wall unit is just within the range, it has the possibility that the fitting limit elevation is appropriate. Although this method has its own shortcoming, it can guide the choice of appropriate fitting limit elevation. As seen in the figures, almost all the fitting limit elevation can meet the condition of wall unit. This means that it is still difficult to decide the appropriate fitting limit elevation using the above two criteria. Another criterion should be developed to guide the decision of the suitable fitting elevations. As shown in theory, the log law method is based on the profile fitting process, it is necessary to make detailed investigations into the fitting process. When considering fitting process, the correlation coefficient of the fitting really can give certain guide to the goodness of the fitting, meanwhile, the errors between the measured data and the model data also should be taken into consideration. In this study, error level between the measured data and the model data combined with the above two methods is used to indicate the fitting is good or not. Then the corresponding fitting limit can be decided uniquely based on the three criteria. The error level is calculated based on the following equation 4-19:

$$\%error = 100\left(\left|\frac{measured\ data - model\ data}{measured\ data}\right|\right) \quad (4\text{-}19)$$

It should be noted that since the sensitivity of the fitting progress, it is important to make sure that all the fitting points should have small fitting errors. For instance, if some portion of the fitting points has large fitting errors with other portion has small fitting errors; the total fitting errors may be small. However, in log fitting process, we should avoid these kinds of problems. So the individual error also should be taken into consideration so as to make sure that the fitting results can really be the log profile. Then the standard deviations of the errors should be calculated. If the mean errors are small and the corresponding standard deviations are also small, and the correlation coefficients are larger than the threshold, then the fitting can be regard as good enough to be log profile and can give reliable estimation of the bed shear stress

The procedure of log law fitting is done in the following steps:

1. The log law is done to different fitting limit elevation, whilst the lower 5 points are always included in the fitting. Then the corresponding bed shear stress can be estimated that using different fitting limit elevation with corresponding correlation coefficients.

2. The non-dimensional wall unit is calculated based on the friction velocity estimated using the above fitting at different elevations.

3. The mean and standard deviation of the error between the measured and model velocity were calculated.

4. The elevation when the minimum mean and standard deviation of the error was calculated. If the fitting at this location also can satisfy the correlation coefficient, non-dimensional wall unit, this location is regarded as the fitting limit elevation. Although whether it is the real fitting elevation, the three criteria together can improve the reliability of the fitting results.

Seen from Figure 4-27 and Figure 4.-29, for the two locations, the correlation coefficients can be larger than 0.95 at all the elevation during most of the uprush phases and late backwash. Only during the flow reversal stages, the correlation is much smaller. This is due to the different flow directions within this stage, which is similar to the previous studies. For the non-dimensional wall unit, it is almost within the threshold range at all elevations except at the lower elevations around the flow reversal phases with very low velocities. This is similar to the previous studies of (Puleo et al., 2000) that used high resolution ADVP to measure the velocity profiles in the swash zone and concluded that nearly all the fitting at different elevations can satisfy the condition of non-dimensional wall unit parameter. The mean and standard deviation of the error show interesting tendency. Both of the two parameters show lowest values close to the bottom indicating that the measured velocity profiles are almost exactly log profiles. Then the log law method results can be more reliable within this thin layer because of the high correlation coefficient, suitable non-dimensional wall unit and small mean and standard deviation of the errors. Although the mean and standard deviation of the errors show some fluctuations during the whole swash event, the elevations are all around the mean elevation. What's more, seen from the bed shear stress results, the bed shear stress shows consistent values close to the bottom. That means during a constant value equal to the averaged elevation

can be used to be the fitting limit elevation. By checking the mean and standard deviation of errors for the two locations, an elevation of 0.82 mm was chosen as the fitting limit elevation. This value also satisfies the practical condition that usually the log layer is located under the 20% of the whole water depth. Then the bed shear stress can be obtained by fitting the measure velocity profile to the log profile to this elevation.

The estimated bed shear stress at that elevation was shown in Figure 4-28, together with the velocity at this elevation $\overline{U_0}$, which will be used as free stream velocity when calculating the friction coefficient in the following analysis. The velocity at the elevation of 10 mm also is plotted in the figure, which also will be used as free stream velocity in the following. The reason is that for the velocity profiles close to the bottom usually cannot be measured easily, then the quadratic law has to be applied to get a rough estimation of the bed shear stress with a constant friction coefficient. So by calculating the friction coefficient using the 10 mm velocity, the estimated results can give some guide to the decision of suitable friction coefficient when using quadratic law. And for the current measurement technology, velocity measurement at 10 mm elevation is not a tough work. The measured peak uprush bed shear stress is less than that in the backwash. This may because that the real peak uprush bed shear stress is not captured because of the difficulty in measuring velocity in the initial uprush, where large velocity gradient usually occurs. However, for the backwash, although the real peak bed shear stress is also not measured, the measured peak value should close to the real peak value. However, in the uprush, the measure one should be far away from the real one. It should be pointed out that, in the previous studies that using high resolution measurement technique, also found that the measured peak

backwash bed shear stress is larger than the peak uprush bed shear stress. However, for the studies using coarse measurement velocity data, the measured peak uprush bed shear stress is usually larger than that in the backwash. This is due to the fact that in the coarse case, both the measured peak value in the uprush and backwash is far away from the real peak value. That means the backwash flow was successfully measured in this study, which is advanced compared with previous studies in which the backwash velocity is usually poorly measured.

For the friction coefficient estimation, the main difficulty relies in the selection of appropriate free stream velocity. As seen from the above equations, when using smaller free stream velocity, the larger friction coefficient can be obtained. In this study, velocity at the log fitting limit elevation and that at 10 mm was used to estimate the friction coefficient. The mean friction coefficients averaged over early uprush and late backwash also were calculated with the aim to find a constant value for the application of quadratic law. The results show that the friction coefficients during the uprush are smaller than that in the backwash. This is because of the large velocity and small bed shear stress in the uprush and small velocity and large bed shear stress in the backwash. Using the log fitting limit elevation gives mean friction coefficients of 0.0014 and 0.042 for the uprush and backwash, respectively. Using the10 mm elevation velocity gives mean friction coefficients of 0.008 and 0.031 for the uprush and backwash, respectively. These values are similar to the previous studies in the uprush except that in the backwash with high friction coefficients. The reason has been stated above; the high-resolution measurements clearly resolved the velocity in the late backwash which was not in the previous studies.

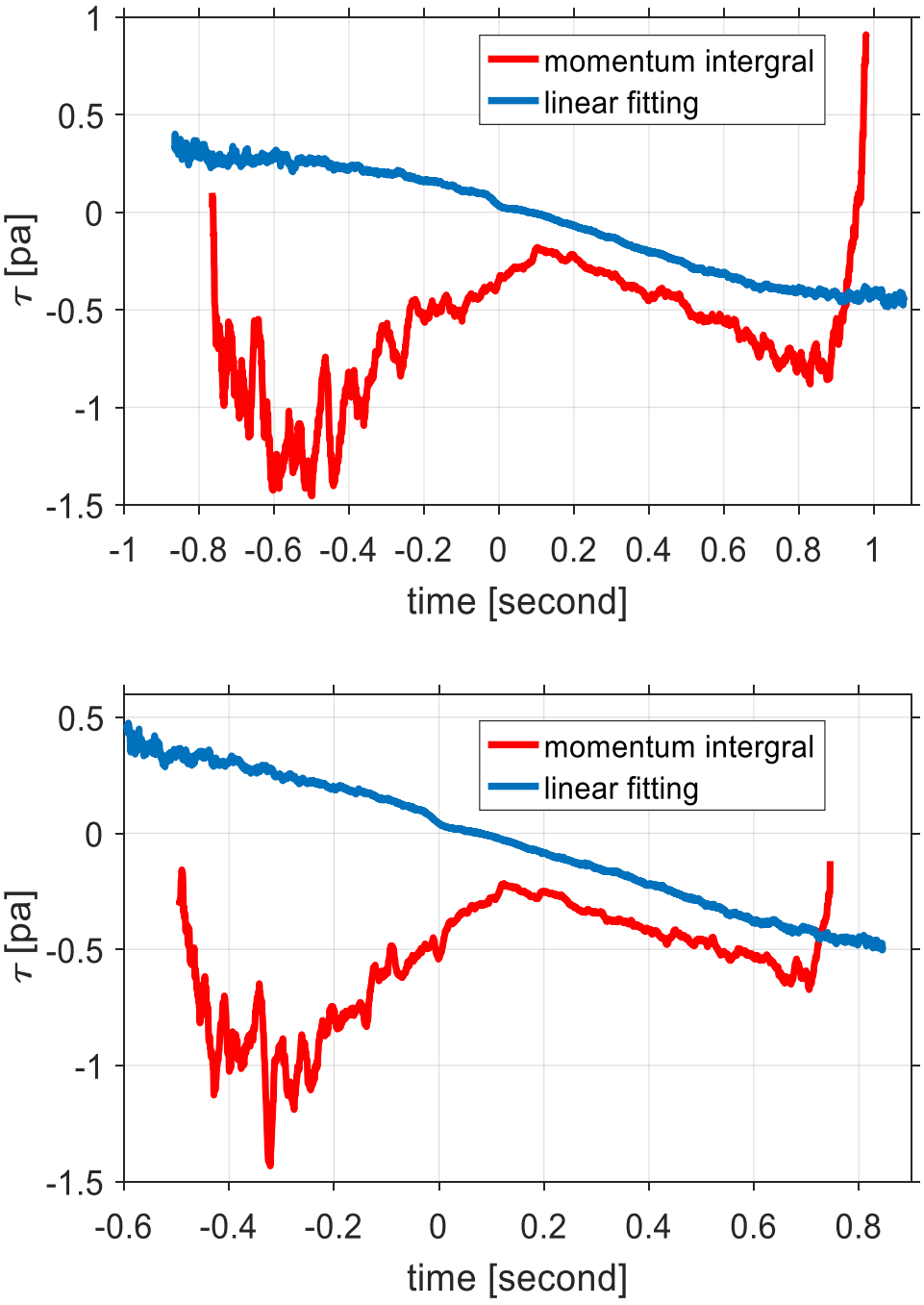

Figure 4-25 Time series of bed shear stress estimated using momentum integral method and linear fitting method First panel: L1; second panel: L2.

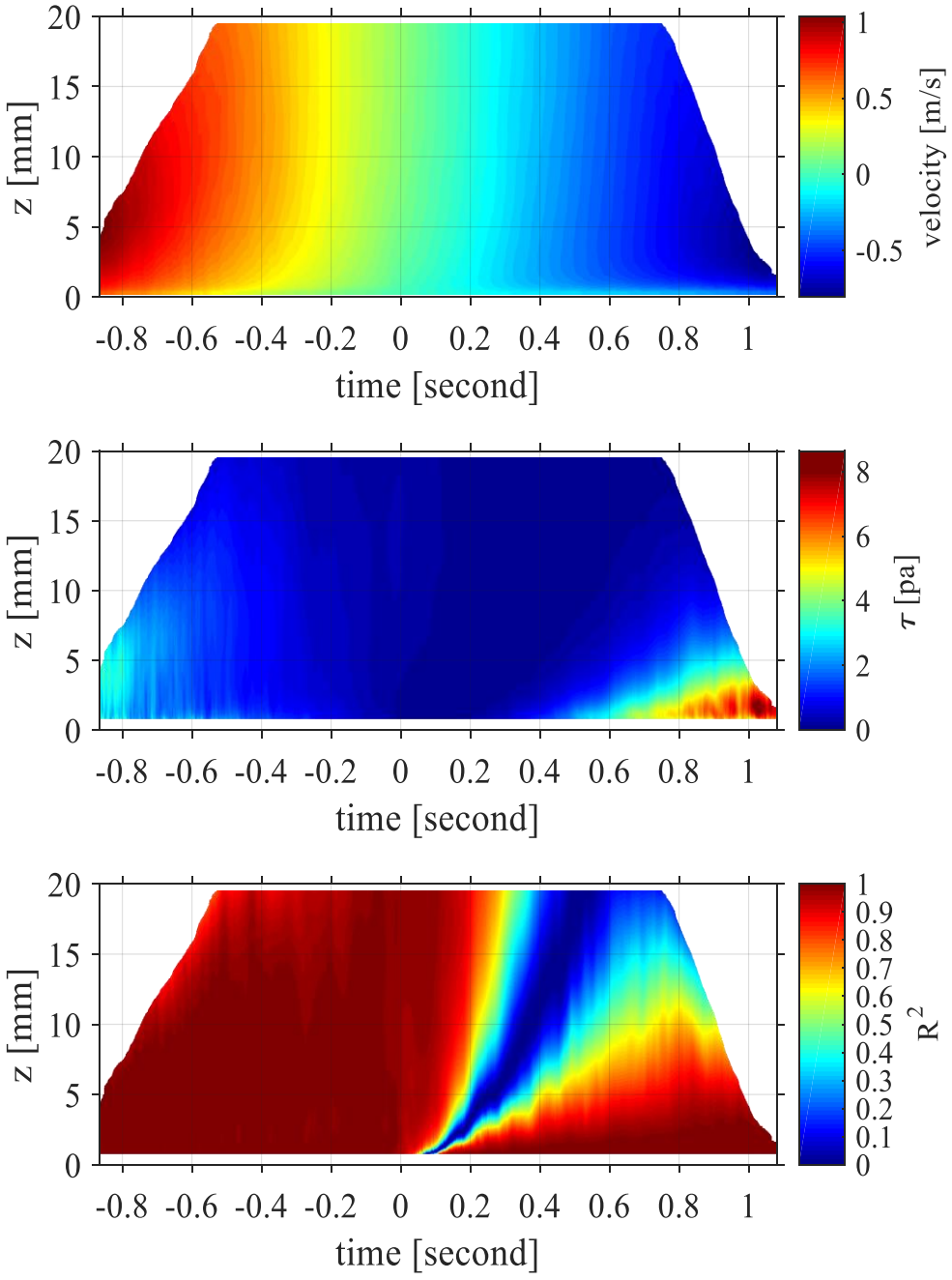

Figure 4-26 Distribution of velocity (first panel), estimated bed shear stress at different fitting elevations (second panel), and correlation coefficient (third panel) at L1.

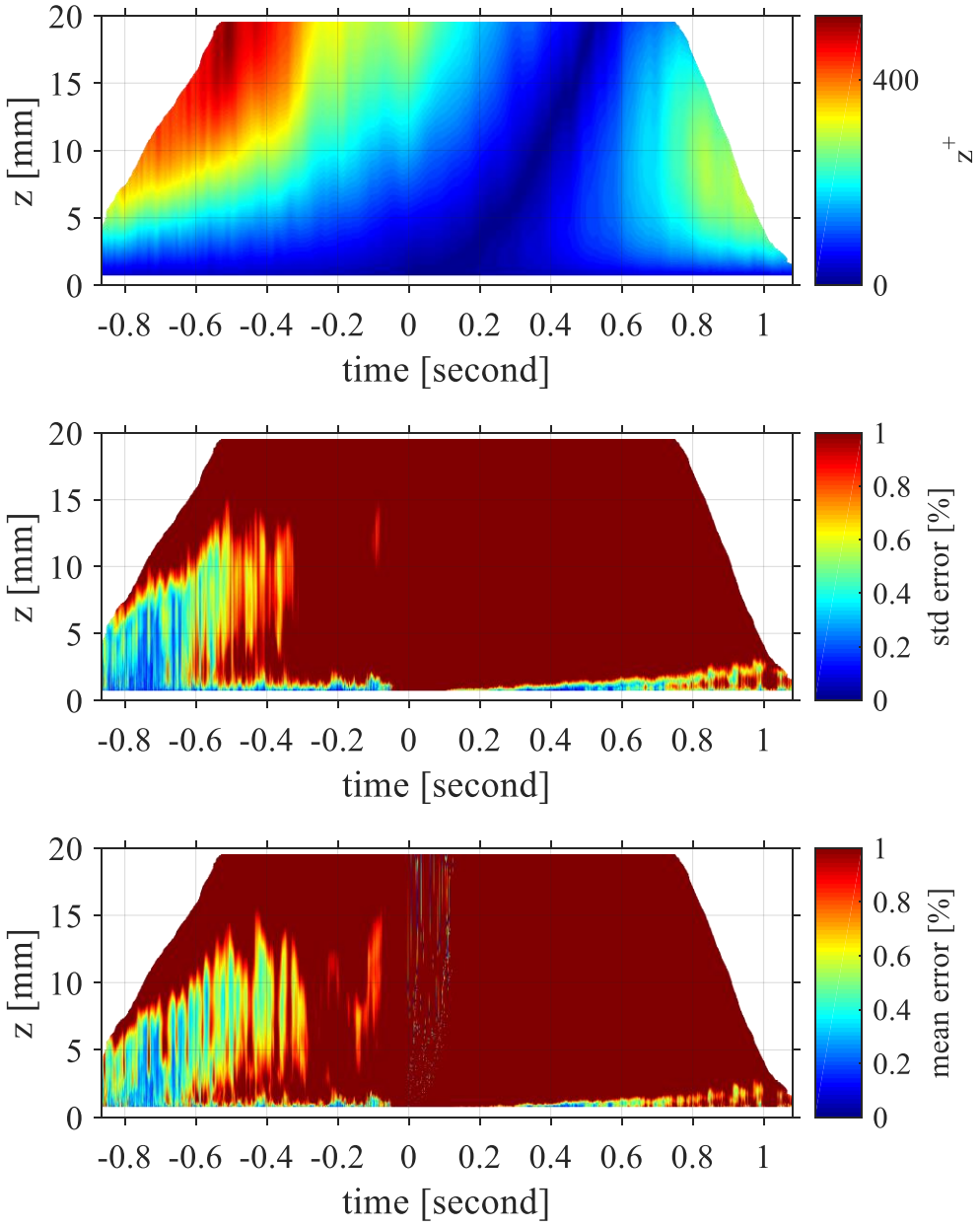

Figure 4-27 Distribution of non-dimensional wall unit (first panel), standard deviation of errors (second panel), and mean errors (third panel) at L1.

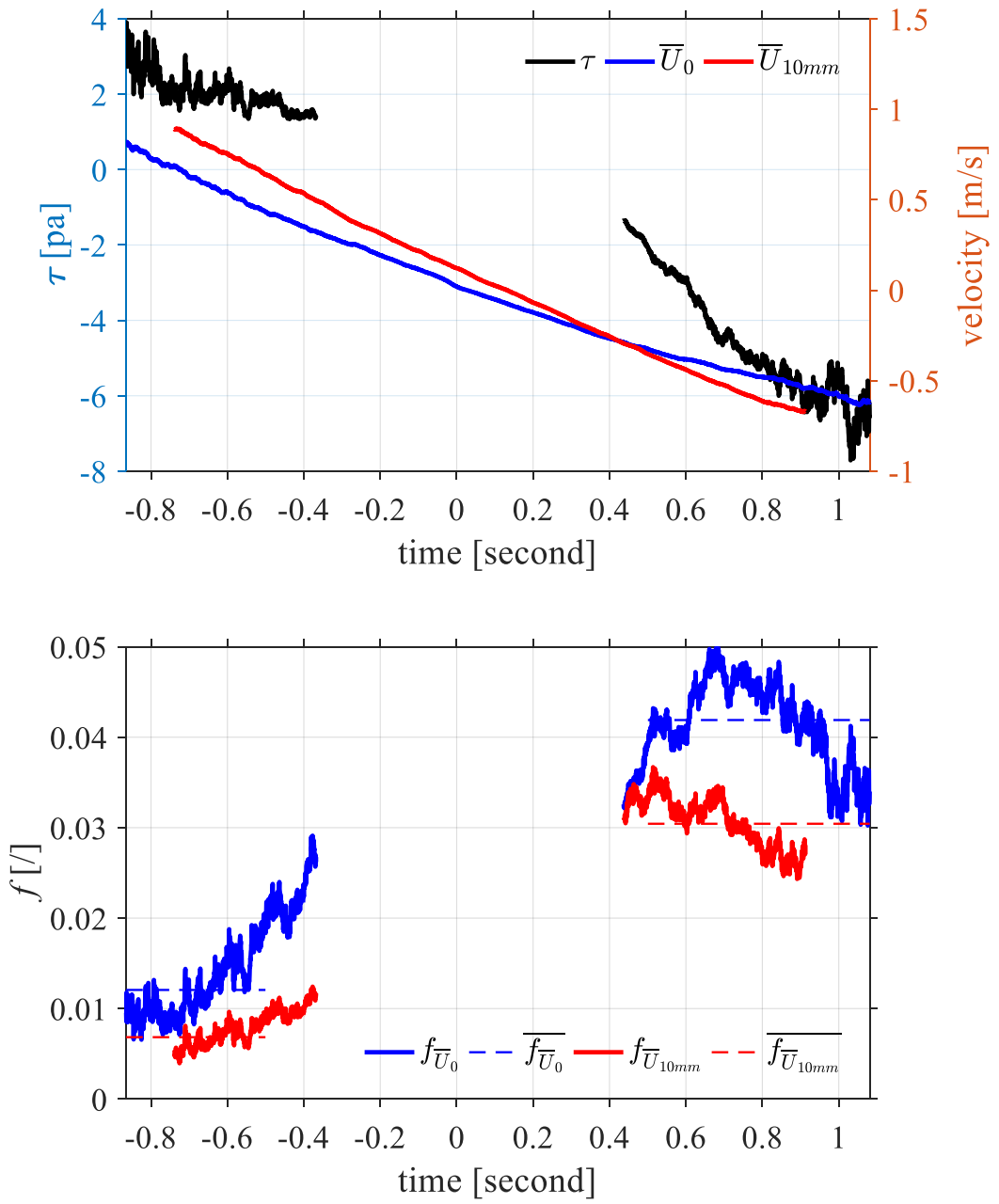

Figure 4-28 Time series of bed shear stress and velocities at the chosen fitting elevation and the 10mm elevation (first panel); corresponding friction coefficient (second panel) at L1.

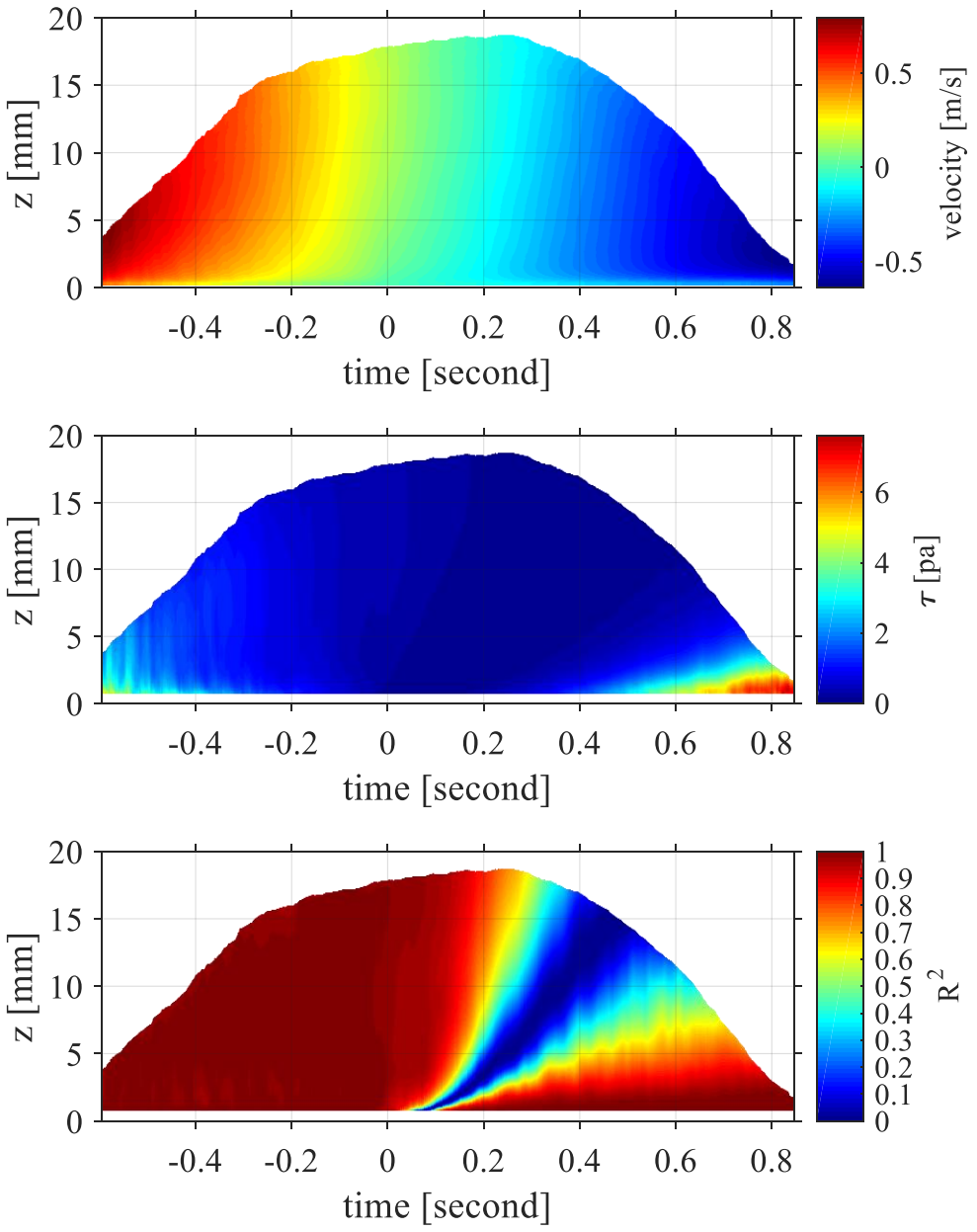

Figure 4-29 Distribution of velocity (first panel), estimated bed shear stress at different fitting elevations (second panel), and correlation coefficient (third panel) at L2.

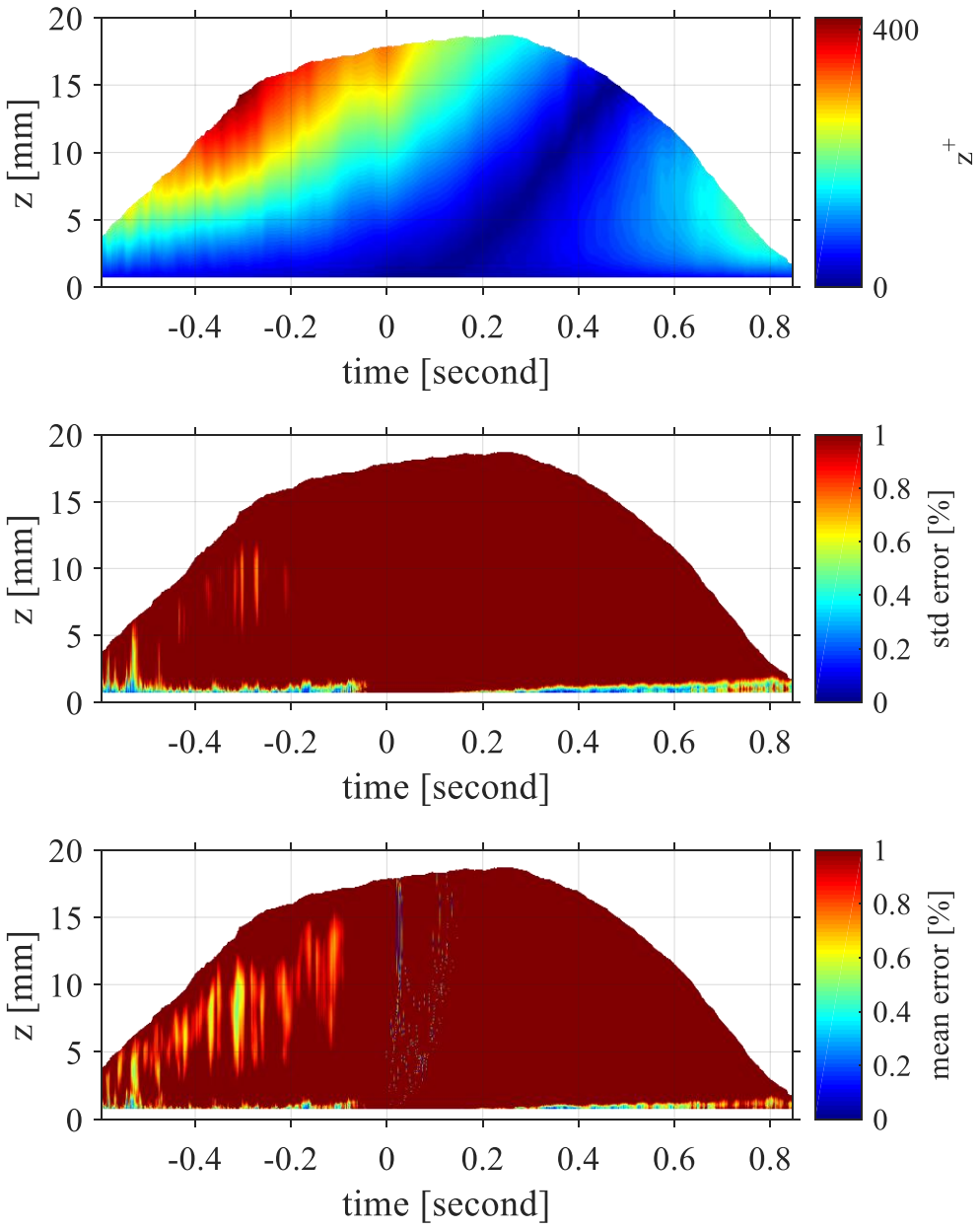

Figure 4-30 Distribution of non-dimensional wall unit (first panel), standard deviation of errors (second panel), and mean errors (third panel) at L2.

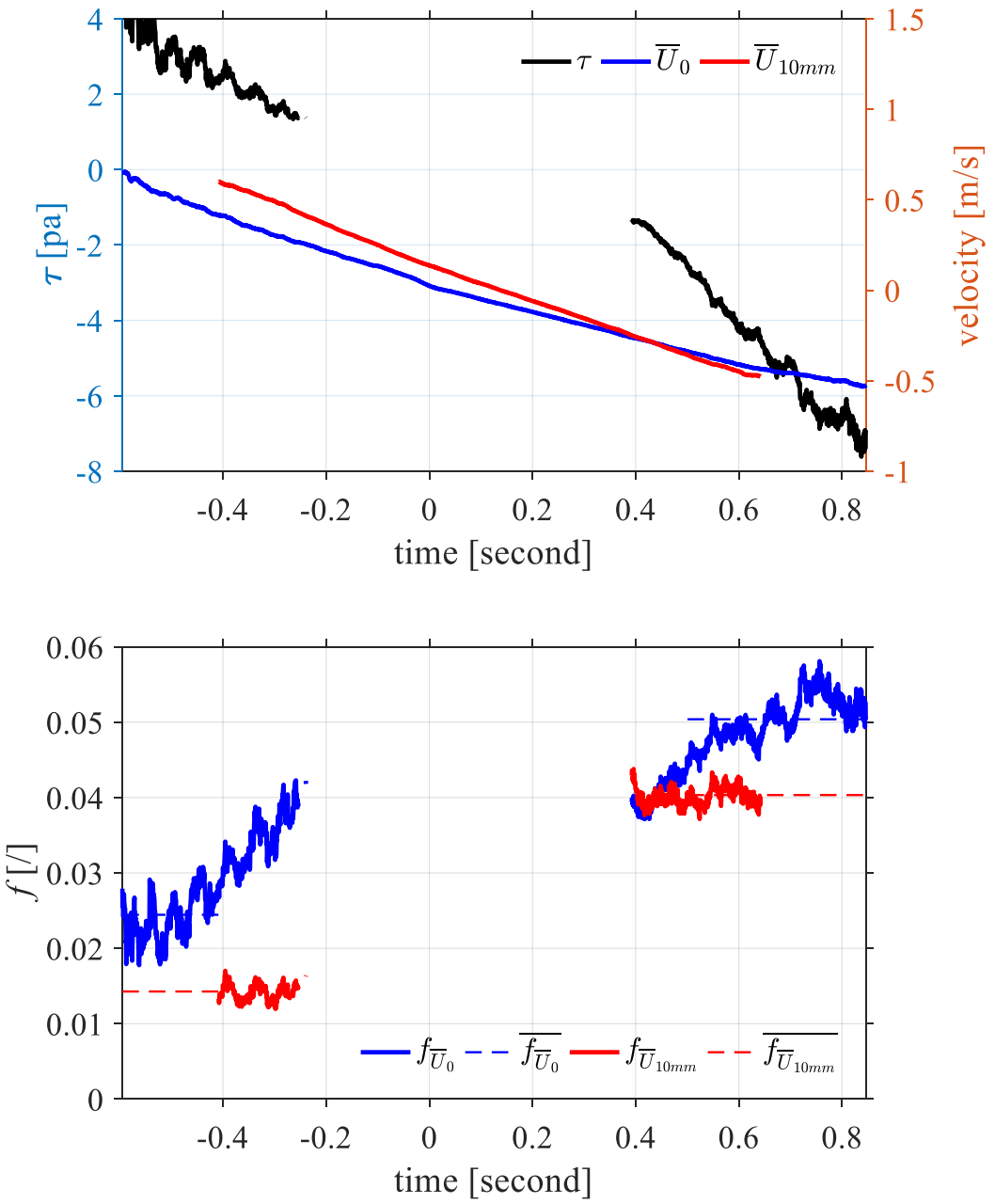

Figure 4-31 Time series of bed shear stress and velocities at the chosen fitting elevation and the 10mm elevation (first panel); corresponding friction coefficient (second panel) at L2.

4.5 Conclusions

Swash flow hydrodynamics in the swash zone has been extensively studied in small scale experiments. The velocity field in the upper swash zone within this bottom boundary layer is measured using high resolution PIV technique. The measured velocities were ensemble-averaged to show the tendency of velocity distribution in the swash zone. The apparent velocity gradient in the early uprush and late backwash clearly shows the existence of bottom boundary layers in these phases. The vertical velocity distribution also shows that the velocity peaks at the vicinity of the surface with smaller velocity in the surface and close to the bed. This is similar to previous studies explained by the vorticity in the uprush front with a negative vorticity in the surface and a positive vorticity close to the bed. The duration of flow reversal almost occupies most of the backwash flow. This is because that there is not enough time for the backwash flow to develop into the fully turbulent flow. The turbulence characteristics were investigated using ensemble average and moving average method by taking advantage of the high temporal resolution. The results show that both in the uprush and backwash, the bed-generated turbulence dominates the flow. The surface-generated turbulence is not as important as that in the lower swash zone because of the non-exist of bore-generated turbulence. The TKE in the uprush is larger than that in the backwash because of the high velocity in the early uprush. It also seems that the moving average method can give appropriate estimation of TKE since this method is based on the local time information with little effects connected to the experimental repeatability. The high spatial resolution in velocity measurements offers the possibility to take log law to estimate the bed shear stress. In this study, the correlation coefficient, the non-dimensional wall

unit and the mean and standard deviation of the fitting error were together used to decide the fitting limit elevation. The results show that in the current study, the fitting limit elevation was appropriate at the elevation around 0.82 mm, which also corresponds to the empirical criteria that the fitting limit elevation should be within 20% of the whole water depth. Especially in this case, smooth bed was used; the thickness of the log layer should be very thin. So the three criteria can give relatively guide to decide the fitting limit elevation. The bed shear stress shows that the peak uprush and backwash value are around 4 pa and 6 pa. This result is consistent with the previous studies using high resolution measurement technique. One main reason is that the measured real peak uprush bed shear stress was far from the measured peak bed shear stress; while the measured peak backwash bed shear stress should be around the real backwash bed shear stress. The corresponding friction coefficients also show the similar tendency with a larger value in the backwash although free stream velocity was adopted at different elevations.

Chapter 5 Large-scale swash experiments

5.1 Introduction

Swash experiments are usually done in small or middle scale using normal wave flume. One disadvantage of the small swash experiments is that the swash duration is too short to make enough measurement. The other one is the small scale may make it difficult to apply the results into field scale when considering the scale effect. One way to conduct large scale swash experiment is to do experiments using huge wave flume, for instance the large wave flume in Delft, Oregon and German. But these facilities are not always available for usual usage. Another way to do porotype swash experiments is to use dam-break facility. By increasing the water level in the flow reservoir and the ratio of water level between the reservoir and in front of the slope can enhance the incident bore. Also using long slope also can make the swash duration longer. Recently, (Pujara et al., 2015) conducted solitary wave experiments in the Oregon large wave flue with the aim to make direct measurements of bed shear stress. The swash flow created by solitary waves beyond the still water shoreline on a plane, impermeable beach is studied. Measurements of the bed shear stress, flow velocities, water depths, and bed pressure and shoreline motion are presented for a wide range of incident solitary waves that span different regimes of wave breaking. The flow evolution due to breaking solitary waves is found to be a gravity-driven flow that is scaled by the initial velocity of the shoreline, which, in turn, is shown to be predicted by measurements of wave height near the still water shoreline. Experimental results are presented that show how different wave breaking regimes influence

the initial shoreline velocity, the swash flow evolution, the run-up and the time period of the swash. Time-histories of the bed shear stress are also presented, but a new normalization for the peak values of the bed shear stress using the initial shoreline velocity shows the cross shore variation of bed shear stress and the influence of different wave breaking regimes. However, the detailed velocity measurement within close to the bottom boundary layer was not measured, which makes it difficult to relate the direct measurements of bed shear stress results to the velocity. This shortcoming limits the application of the results to the practical use. And large scale wave flume experiments also were conducted in the Delta flume (The Netherlands), which is included in the BARDEX II project. These large experiments were designed to investigate the detailed swash hydrodynamics and sediment transport in the swash zone. The velocities were measured by using high resolution ADVP technique that can measure velocity at a resolution 1 mm and the measurement range is about 7 cm. This measurement resolution and rang are much better than the previous studies and many new findings were from this experiments. Also the new findings based on the high resolution velocity measurement motivate us to measure the velocity with much higher resolution so as to estimate these parameters related to the velocity with higher accuracy. However, in the laboratory, velocity is usually measured using PIV technique, the resolution is limited by the CCD camera and the processing algorithm. To investigate the swash hydrodynamics in the large-scale swash experiments with high measurements resolution, experiments under dam break flows were conducted with the main aims to reveal the swash hydrodynamics within the thin bottom boundary layer.

5.2 Experimental setup and instrumentation

Laboratory experiments were conducted using a dam-break flume (15 m x 1.8 m x 1 m) with a reservoir in one end and a 1/10 transparent slope in the other end as shown in Figure 5-1. The slope is designed to be 10 m long so as to increase the duration of swash flow making the longer measurements possible. By quick releasing the gate, a great plunging wave was generated towards the slope leading to a swash bore. The experiments were conducted under the following condition: the initial water depth in the reservoir and on the flume floor is 750 mm and 50 mm, respectively. Five wave gauges were installed as shown in Figure 5-1 to measure the water depth. PIV measures were conducted in 3 locations and every location 100 repeats: first 50 repeats with small Field Of View (FOV) for bottom boundary layer velocity measurement and the second 50 repeats with large FOV capturing the whole water for whole field velocity measurement as shown in Figure 5-2. The repeatability of the facility was shown to be satisfactory by comparing the 50 water depths measured by the wave gauges as shown in Figure 5-3. A high speed camera was used to obtain PIV image pairs with the following setting: 1280 x 1024 pixels, 100 fps time delay between image pairs 100 μs. High-performance double heads Nd:YAG laser with maximum repetition rate up to 100 Hz together with a series of optical elements was used to illuminate the measuring section upward from the under of the slope to avoid free surface disturbances. In the small FOV case, the camera was positioned very close to the laser sheet to increase the magnification (12 μm/pixel) to measure the boundary layer velocities.

In the large FOV case, the distance between the laser sheet and the camera

depends on the measurement location for just capturing the whole water. Glass hollow sphere with a diameter of 10 μm were used as tracer particles. The specific gravity of the particle is slightly larger than unity and thus it follows the water flow well. The timing t = 0 was defined as the timing of gate releasing and simultaneously a TTL signal was generated and sent to trigger a DG645 digital delay generator that used to achieve the synchronization of all the instruments. To achieve this synchronization, a laser displacement meter was installed parallel to the gate, when the gated is opened, the laser displacement meter will send out a TTL signal to the delay generator and then the entire instrument will work simultaneously.

The experimental procedure was described in the following:

1. All the instruments will be checked before conducting experiments to make sure that all can work properly.

2. The gate will be firstly pull down to form the flow reservoir, and then pump will be used to pump water from one side of the reservoir into the reservoir. When nearly reaching the desired water level, the pump will be taken out form the flume and waiting for the water level decreases into the desired water level because of the water leak. At that instance reaching the desired water level, the gate will be released by a quick release system and all the instruments begin to work.

3. Then save the recording images and the wave gauge data into hard disk. After that a new run will start.

4. After finishing the experiments of bottom boundary layer FOV, the next is to

do the experiments with whole water depth FOV. Before the new experiments, the water should be drain off and then have new fresh water into the flume. This is because in the bottom boundary layer measurements the seeding concentration should be dense enough to make sure that many particles can be captured by the high magnification camera. However, in the whole water depth measurements, the seeding concentration should not be so much dense since the magnification is so small that dense concentration will make the FOV all white, thus making the PIV analysis impossible.

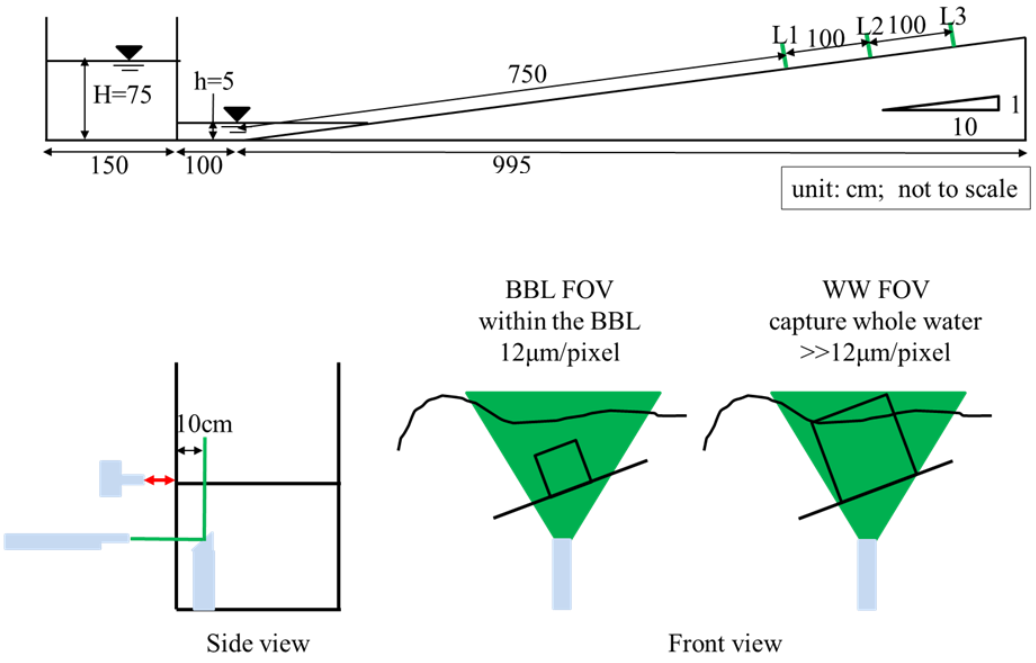

Figure 5-1 Schematic of large-scale dam-break flume with two FOVs.

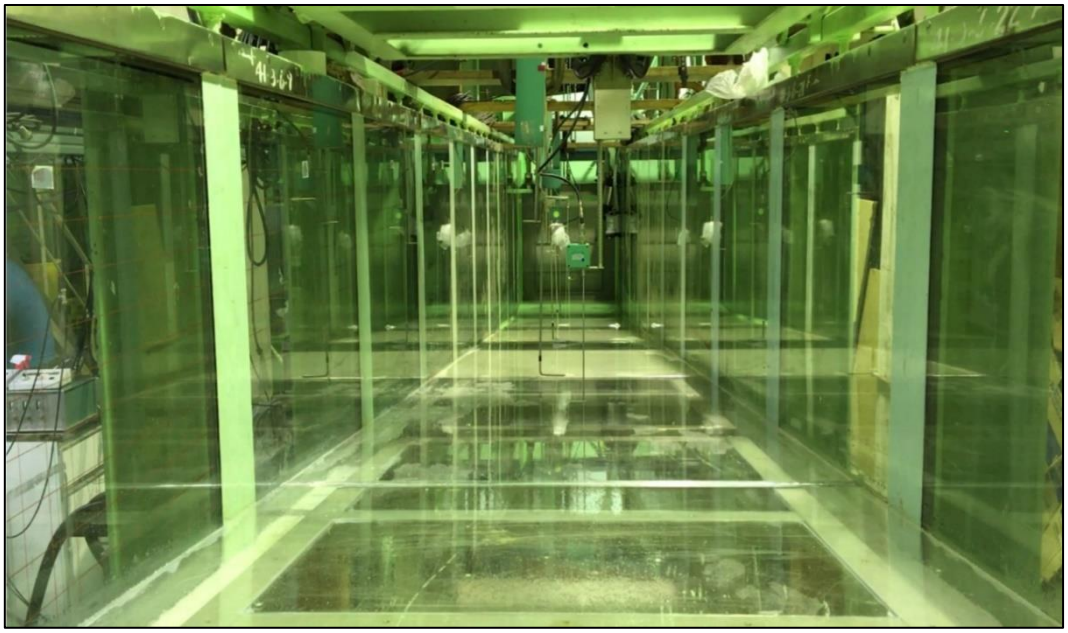

Figure 5-2 Photograph of the large-scale flume.

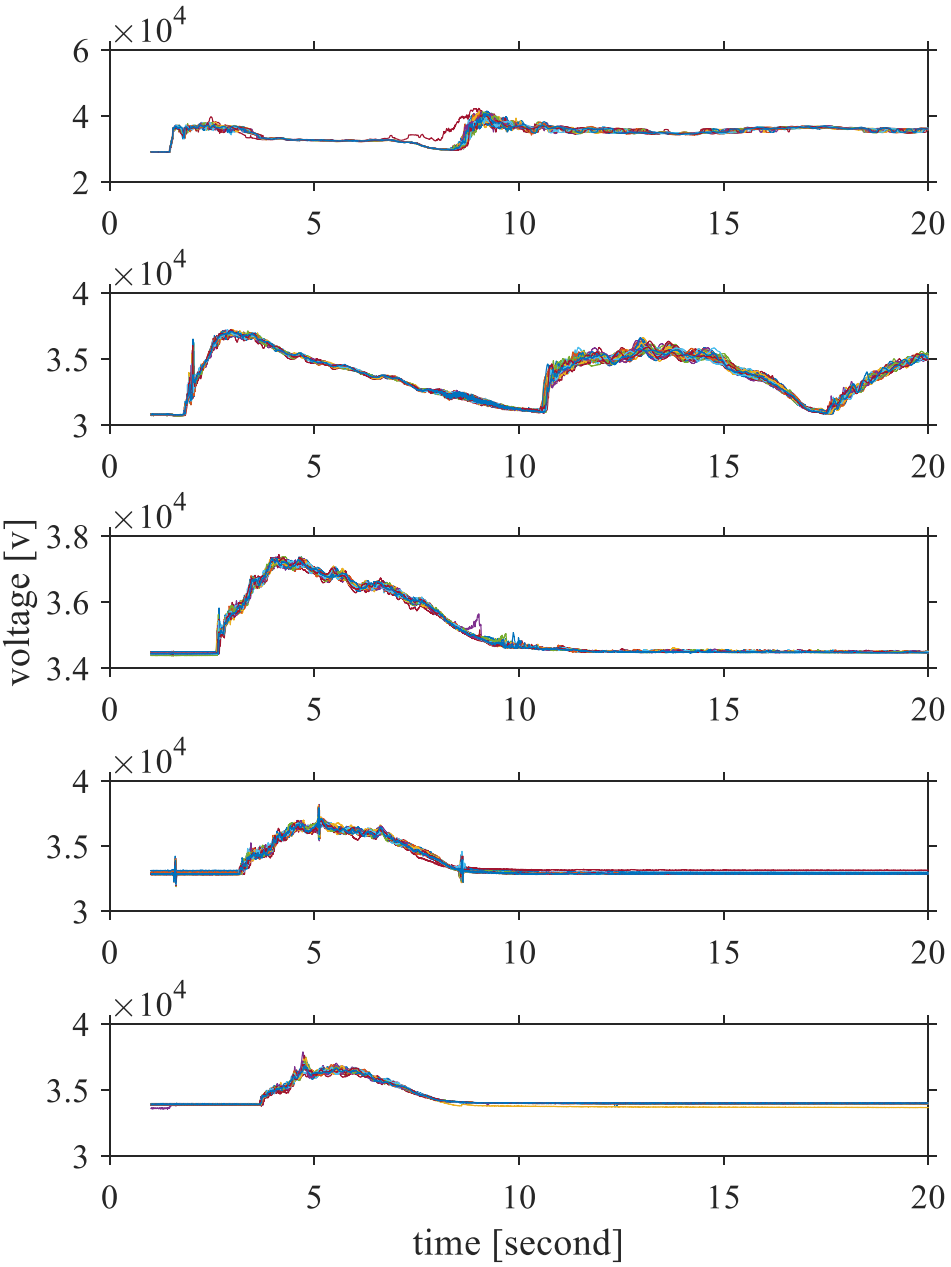

Figure 5-3 Wave gauge results at the five measurement locations.

5.3 PIV recordings processing

Because of the high magnification, the little deformation of the bottom bed can be detected by the high-speed camera. The maxim deformation from initial uprush to the whole water depth is about 30 pixels, which is too large to be ignored. In this study, this bed location was decided by finding the largest pixel intensity along the row of the image. Then the location of largest pixel intensity was regard as the bottom location. For the two successive recordings, the location is decided by finding the higher one since in the following they will be used for PIV analysis to extract the displacement.

After deciding the bottom location, the intensity capping method again was used to make all the pixel intensities to a similar level so as to increase the robust of the PIV analysis. This method is especially useful for the large-scale experiments, since some dirty materials are always included in the flume and once they enter the FOV, the image will be largely affected by these materials. In this study, three steps were used to do the cross-correlation work. The first step uses 156 x 32 interrogation window size with FFT algorithm for estimating the rough displacement. The second step uses 96 x 16 interrogation window size with FFT algorithm with a window offset based on the first step. The final step used 96 x 8 interrogation window size to calculate the velocity using modified FFT method. By using the modified FFT, the subpixel can be calculated accurately without introducing the errors caused by the normal FFT method. Here it is important to point out that in the bottom boundary layer measurements, the interrogation window size must be a rectangle with larger size in the flow direction and smaller size in the normal direction. This is because the flow in the bottom boundary

layer has high velocity gradient in the vertical direction. Using square interrogation window will decrease the velocity very much since the final results are an averaged value of the interrogation window. The measured velocity data usually contains outliers due to uneven seeding particles and sudden exist of dirty materials. It is very necessary to do the outlier check before analyzing the velocity data for further analysis. In this study, the outliers are decided by using the statistical method known as Grubbs Test. After detecting the outliers, the outliers were replaced by the values calculated using the neighbor data. As for the ensemble averaging, for all the runs, they have similar duration; then interpolation of the data into the same length is carried out to do the ensemble averaging. we already checked that using the timing when water depth is larger than some threshold or using the timing of flow reversal both give a similar ensemble averaged results.

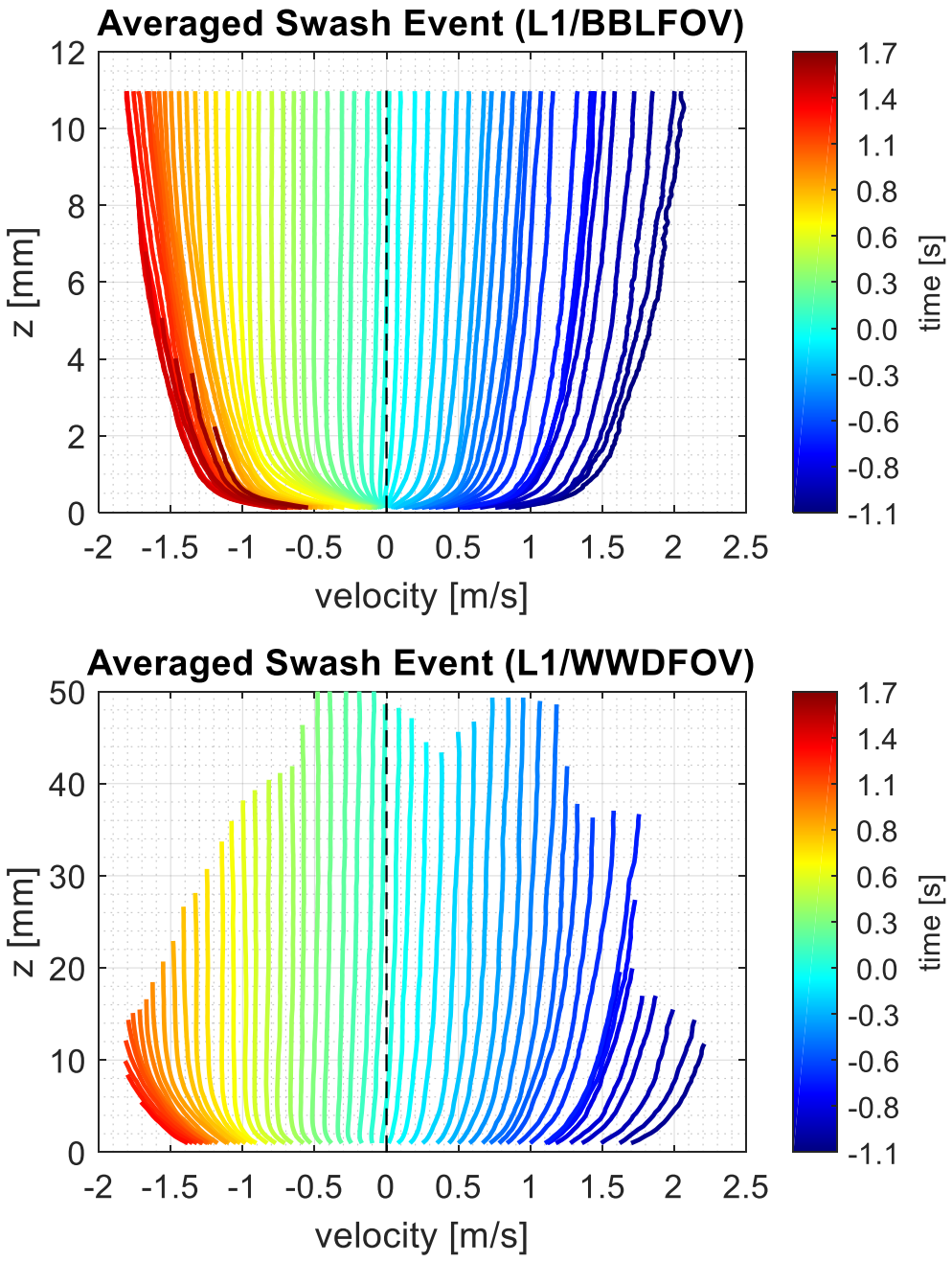

Figure 5-4 Velocity profiles based on averaged swash event at L1 for BBLFOV (first panel) and WWDFOV (second panel).

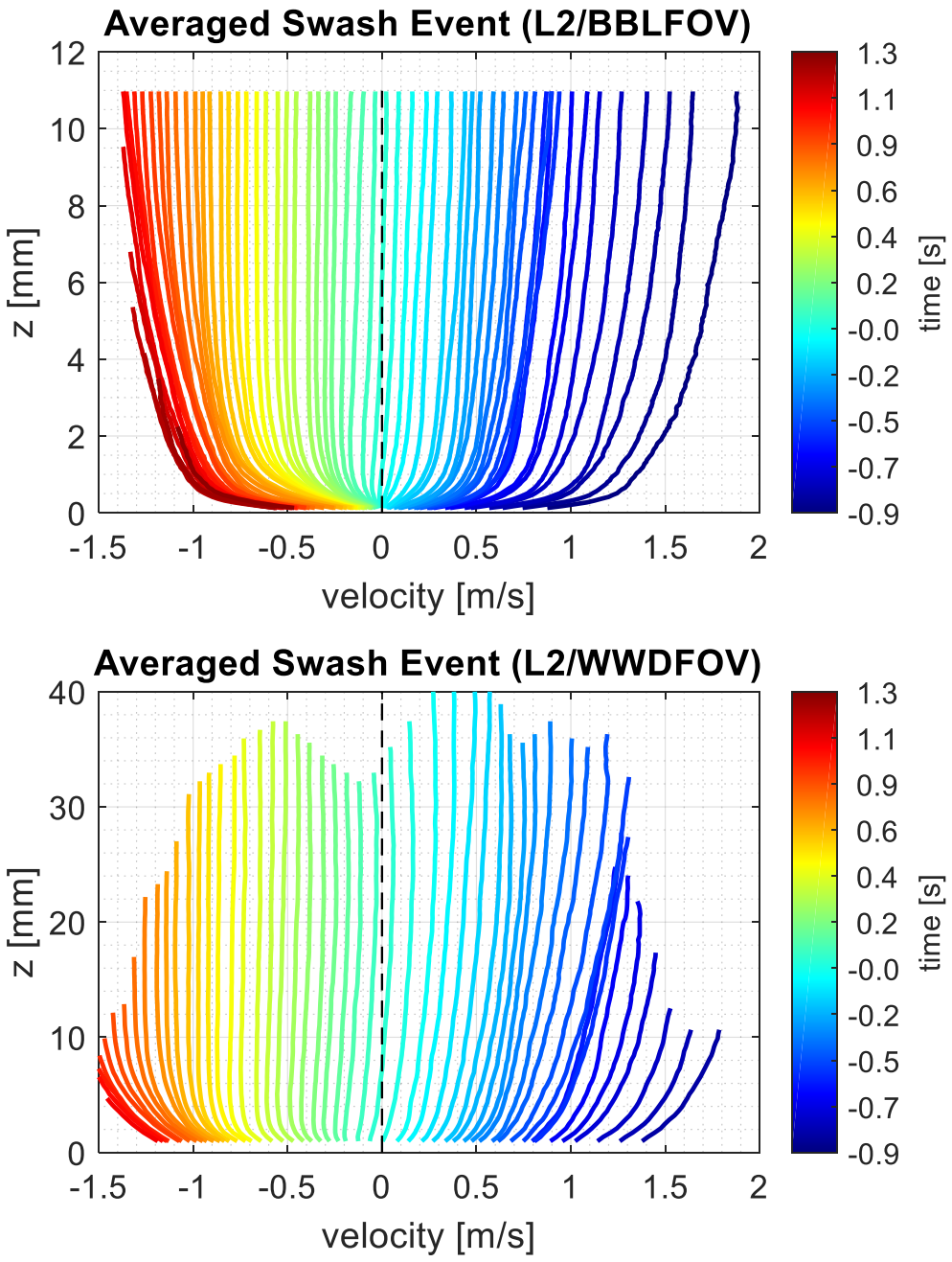

Figure 5-5 Velocity profiles based on averaged swash event at L2 for BBLFOV (first panel) and WWDFOV (second panel).

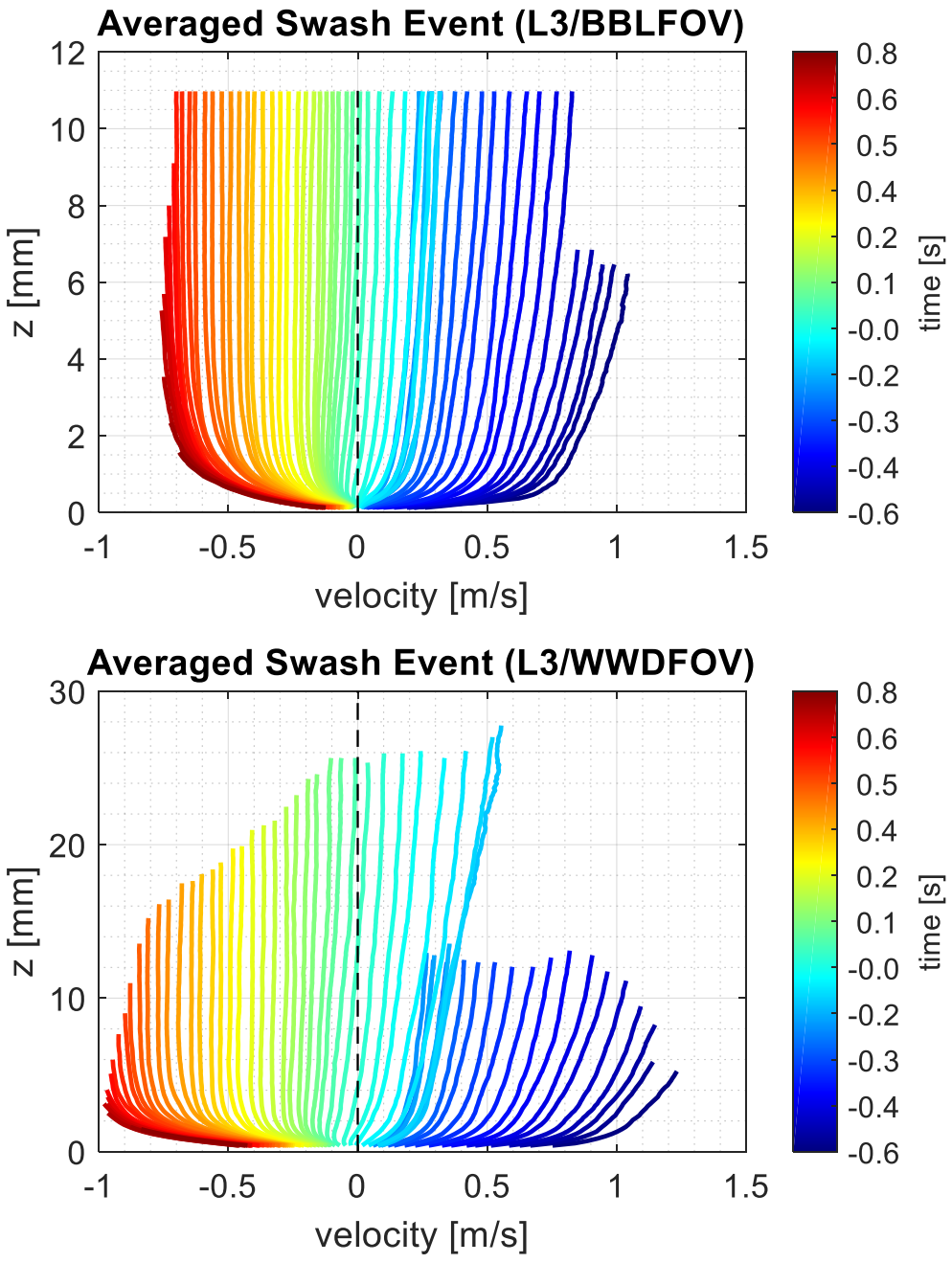

Figure 5-6 Velocity profiles based on averaged swash event at L3 for BBLFOV (first panel) and WWDFOV (second panel).

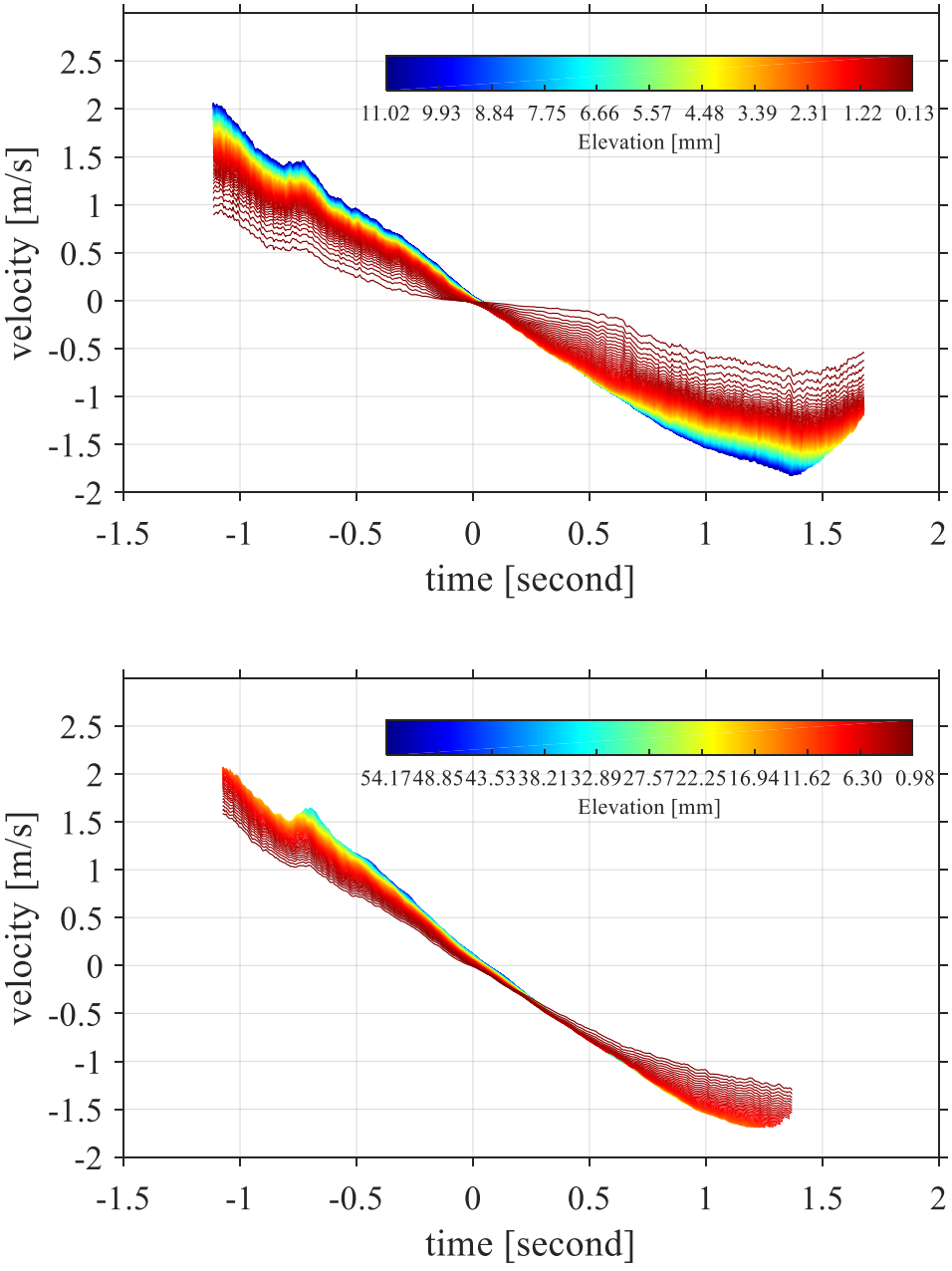

Figure 5-7 Time series of velocity at selected elevations at L1 for BBLFOV (first panel) and WWDFOV (second panel).

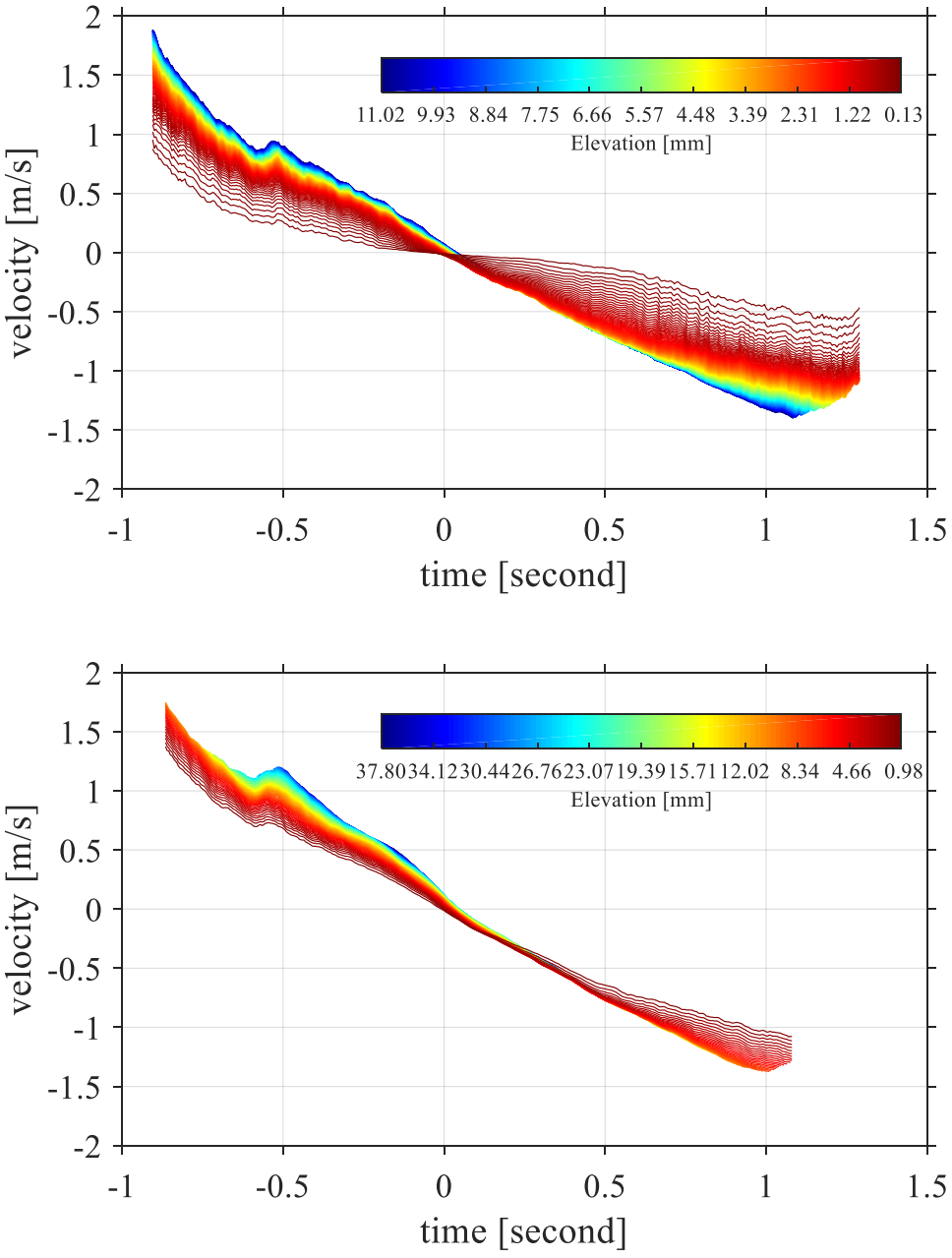

Figure 5-8 Time series of velocity at selected elevations at L2 for BBLFOV (first panel) and WWDFOV (second panel).

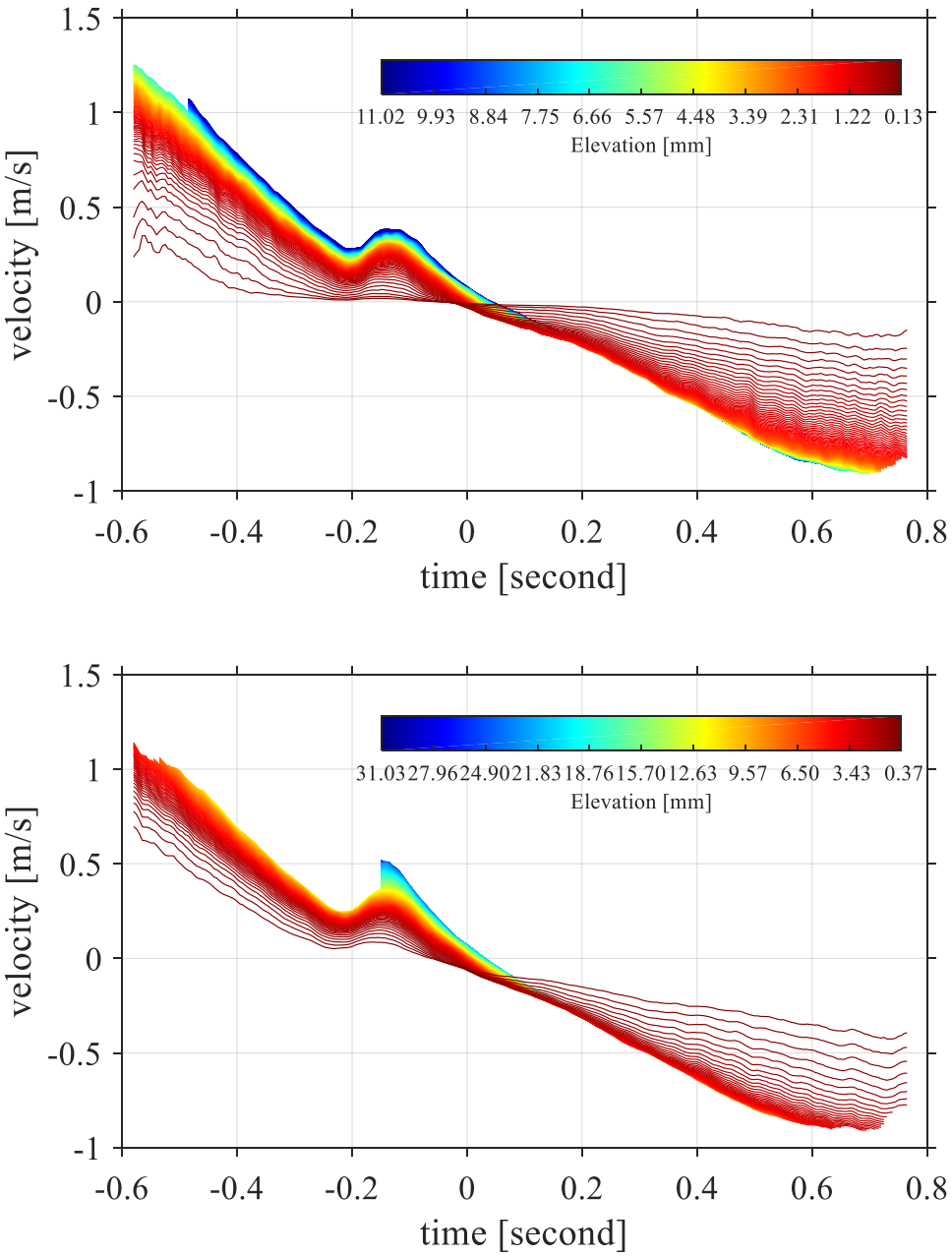

Figure 5-9 Time series of velocity at selected elevations at L3 for BBLFOV (first panel) and WWDFOV (second panel).

5.4 Results

5.4.1 Velocity profile

Based on the high repeatability of the experiments, measured velocities are ensemble averaged. In the following the ensemble averaged bed-parallel velocities are analyzed from the two FOVs for the three measurement locations (Figure 5-4~Figure 5-9). As the general characteristics of the velocity distributions have been analyzed in the small-scale experiments, here only the differences will be emphasized. In current study, the measured peak velocity exceeds 2 m/s in the uprush. This velocity can stand for the scale of real velocity and was observed in the field in previous studies. Although the measurement using different FOVs both can reveal the general tendency of the velocity distribution, the differences still can be observed especially during the late backwash. Using high spatial resolution measurement, the decelerating phenomenon can be detected successfully. However, these decelerating phases cannot be captured by the coarse resolution measurement. Another difference is that the high-resolution measurement can detect the high velocity gradient close to the bottom and this information is very useful when bed shear stress estimation was considered. This can easily be seen from the velocity time series at different locations. The velocity gradients in the high-resolution measurement are less apparent than that in the coarse measurement resolution. At location 3, the min bore collapse phenomenon was successfully measured using high resolution measurement. This mini bore collapse was already found in previous numerical studies (Zhang and Liu, 2008). However, it is the first time that the velocity distribution at the mini bore collapse phases is successfully captured. Because the mini bore collapse occurs at the very shallow water depth, and it is

very difficult for previous studies to make measurements in such shallow area. Compared the results obtained using high resolution and low resolution measurements, it can be concluded that the accuracy is dramatically increased with high resolution measurement, although the general tendency is similar. And much more phases of late backwash phases can be detected since when the water depth is shallow the low-resolution measurement always falls. It is important to note that in current study, the free surface was not detected accurately. So the velocities in the vicinity of the free surface were not investigated. And the phenomenon that the peak velocity occurs below the vicinity of the free surface cannot be found in this study.

5.4.2 Turbulence evolution

In this large-scale experiment, the turbulence is analyzed based on the ensemble average method to extract the turbulent velocity. Although as stated in the previous chapter, the moving average is a more robust method, the YAG laser pulse rate of 100 Hz is still not high enough to apply the moving average method to decompose the turbulent component. The TKE results obtained using ensemble averaging method are presented for the three locations (Figure 5-10~Figure 5-12). The first panel and the second panel show the results for BBLFOV and WWDFOV, respectively, with the third panel presents the depth averaged TKE. TKE results using the two FOVs depict similar tendency for the three locations: the high resolution always gives higher TKE level compared with that for the coarse resolution. However, the turbulent level is different from location to location. At location L1, the high TKE in the uprush should be related to the bed-generated turbulence and surface-generated turbulence; in the backwash, there is no significant TKE magnitude in the surface indicating that bed-generated

turbulence should be the main contribution to the total TKE. The depth averaged TKE shows that in the uprush the magnitude is about two to three times larger than that in the backwash both for the high-resolution data or low resolution data. At location 2, seen from the upper panel, in the uprush, although the surface-generated turbulence still has contribution to the total TKE, the percentage of its contribution is less compared with that at location 1. There is a small peak around t = -0.5 s, which should correspond to the mini collapse phenomenon. This small peak also can be found at location 1 around t = -0.8 s and at location 3 around t = -0.1 s. Compared with that at location 1, the depth averaged TKE level in the backwash is similar; in the uprush, it shows a little smaller value. At location 3, the TKE distribution is different from that at the former two locations. The TKE level in the uprush decreases to the similar level in the backwash, indicating the decreased effects of surface-generated turbulence to the total value. In fact, location 3 is close to the run-up limit, where the surface-generated turbulence almost completely dissipated. In short, from location 1 to location 3, the TKE level is decreasing because of the dissipated effect of surface-related turbulence and the decreasing velocity magnitude. The TKE obtained using the high-resolution data shows a little higher value that that of the coarse resolution, indicating that the smaller scale turbulence is more resolved by the high-resolution measurements.

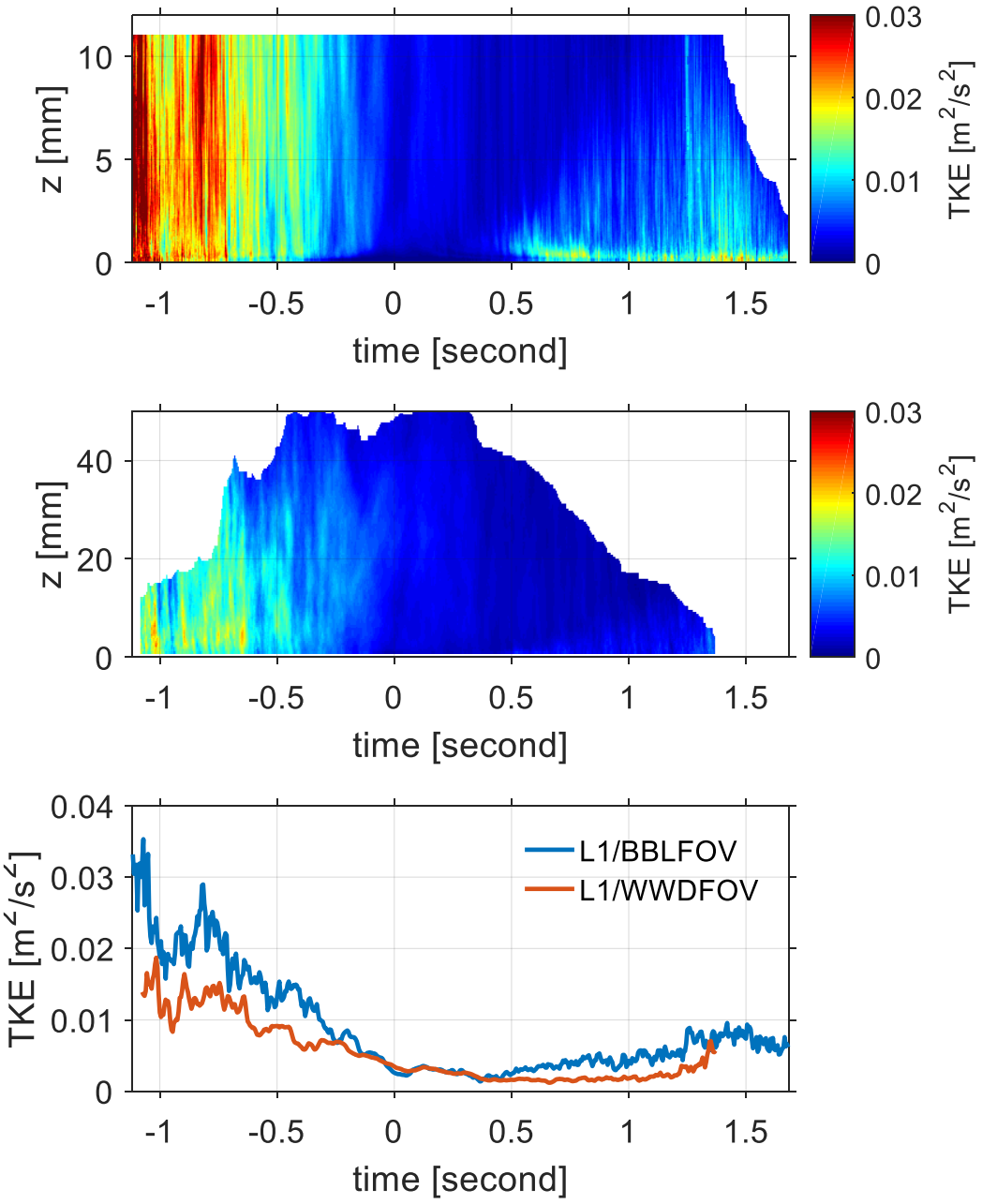

Figure 5-10 Estimated TKE at L1 for BBLFOV (first panel), WWDFOV (second panel) and depth-averaged TKE for the two FOVS (third panel).

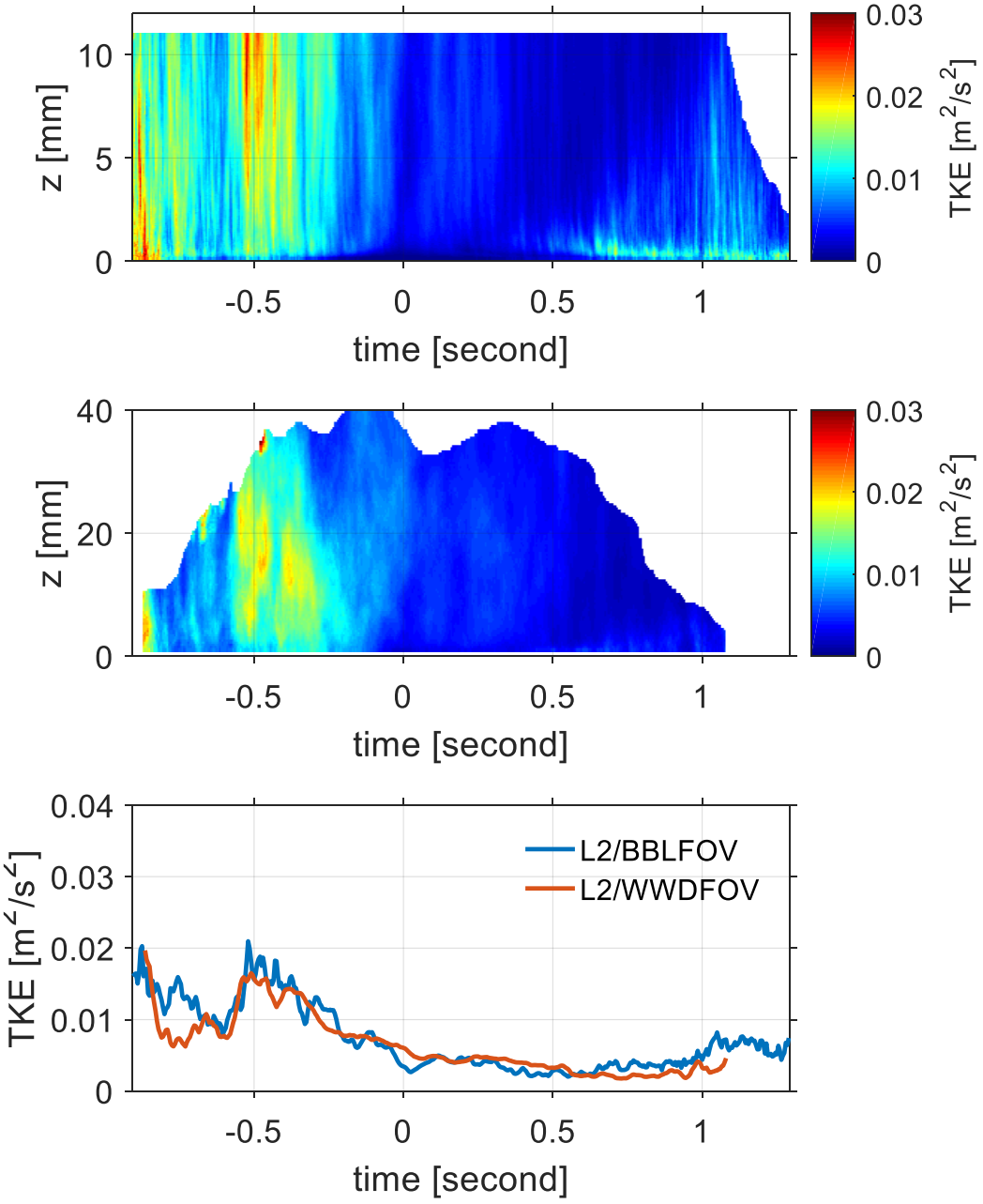

Figure 5-11 Estimated TKE at L2 for BBLFOV (first panel), WWDFOV (second panel) and depth-averaged TKE for the two FOVS (third panel).

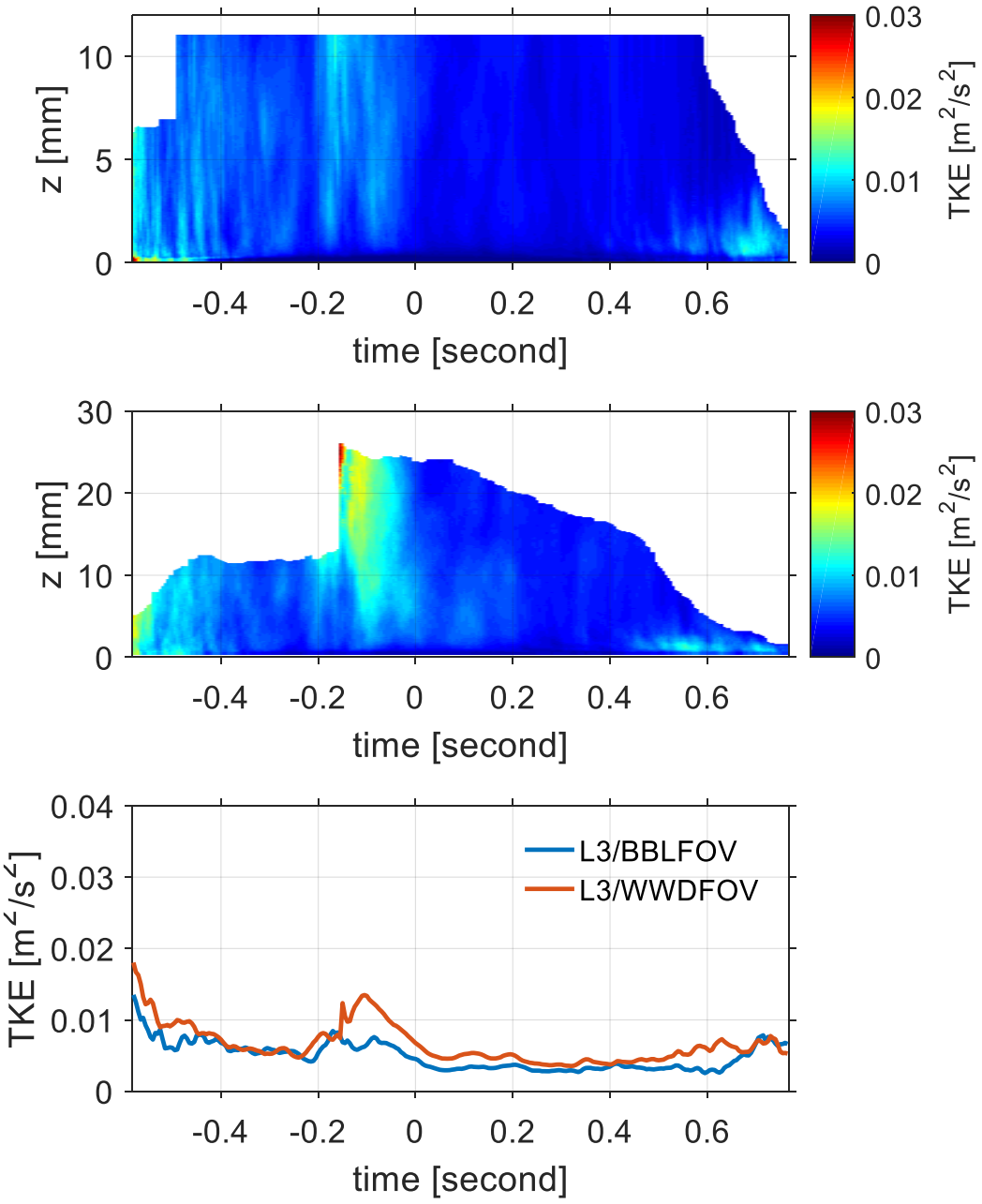

Figure 5-12 Estimated TKE at L3 for BBLFOV (first panel), WWDFOV (second panel) and depth-averaged TKE for the two FOVS (third panel).

5.4.3 Bed shear stress estimation

As described in the small-scale experiment, the momentum integral method and linear fitting method cannot give satisfactory bed shear stress estimations. As concluded by the previous studies, the bed shear stress estimated using the log-law gives the best match to the results using direct shear plate sensor. What's more, the log-law is widely used in the previous studies, making the comparison between previous studies more easily. The resolution in the large-scale experiment is higher than that in the small-scale experiments, which can improve the confidence of the estimated results. In the large-scale experiment, log-law also is used to estimate the bed shear stress and the corresponding results are presented in the following figures (Figure 5-13~Figure 5-28). At location 3, the velocity distribution using BBLFOV close the bottom shows much smaller value, whether this is error or not is unclear. And the log-law is much related to velocity profile, so the bed shear stress at location 3 for the WWDFOV is not estimated and analyzed in the following.

Bed shear stress shows similar tendency at the three locations, so the estimated results at location 1 are taken as an example for further analysis. As shown in the third panel of Figure 5-13, the correlation coefficients are all very high in the whole uprush and most of the late backwash with small values around the flow reversal. So it is still difficult to decide the upper limit elevation of the log-fitting. From the first panel of Figure 5-14, the non-dimensional wall unit values are almost all less than 1200, which is the upper limit value of the log law layer. However, during the flow reversal stage, the non-dimensional unit is very low, with values less than 30, showing the difficulty in applying the log-law here. In fact, in the flow reversal stage, the opposite directions of the flow close to the

bottom layer and the upper layer makes the application of the log-law difficult. The mean errors and the standard deviations of the errors show the similar tendency, with smallest values located at the elevation close to the bottom. So by taking the correlation coefficients, the non-dimensional wall unit, the mean errors and the standard deviations of the mean errors into consideration, the upper limit of the log fitting can be uniquely decided with the best fitting. At location 1 for the case of BBLFOV, the upper limit of the log-fitting is decided to locate at 0.46 mm from the bottom, which is a very small value that usually cannot be measured by the previous studies. However, it should be pointed out that the log-layer is a very thin layer in theory, especially on the smooth bed. For the case of WWDFOV, the upper limit of the log fitting is chosen to be 2.836 mm, which is also a very small value. The upper limit of log fitting is the same for location 1 and location 2 for the both FOVs.

The bed shear stress results shown at the first panel of Figure 5-15 depicted that the peak magnitudes in the uprush and backwash are almost similar. However, it is pointed out by many previous studies that the measured peak uprush bed shear stress is larger than that in the backwash. It must be acknowledged that the true peak bed shear stress during the uprush may be larger than those calculated but is potentially undetermined due to velocity data from the beginning of the uprush is not measured because of the air bubbles contained in the bore front. Higher bed shear stresses during the uprush are normally attributed to bore-generated turbulence impinging on the bed (Puleo et al., 2000).

However, Osborne and Rooker (1999) investigated turbulent energy in the

swash zone and concluded that the influence of bore turbulence is short lived following bore collapse. Therefore, turbulence is likely to have been less significant in this study due to the distance between bore collapse and the location of measurement. Additionally, the short period of flow acceleration at the beginning of the uprush responsible for enhancing bed shear stress in some studies is also absent from the data record. These factors suggest that the bed shear stresses presented may not be representative of flows further seaward in the swash zone. Higher bed shear stresses at the beginning of the uprush and end of the backwash are to be expected because of the higher flow velocities and steeper velocity gradient at these times. The characteristic of a larger or similar peak bed shear stress in the backwash is also found at location 2 and location 3 for the BBLFOV. The consistency of the current measurement with previous studies using high resolution measurement technique shows that the swash hydrodynamics in the upper swash zone should be different from that in the inner swash zone. Especially, at location 3, the measured peak bed shear stress in the backwash is almost 3 times larger than that in the uprush. Another point is that the measured peak uprush bed shear stress estimated using data from WWDFOV is similar or larger than that in the backwash at location 1 and location 2. Since the measurement resolution of WWDFOV at location 3 is different from that of the other two locations, so the comparisons cannot be made. However, by comparing the bed shear stress results estimated using high resolution and low resolution at the first two locations, it should be concluded that the resolution is very important. With different resolutions, opposite conclusions can be obtained, indicating the necessary of high resolution data to reveal the actual characteristics of swash zone flow.

As for the non-dimensional bed shear stress, the friction coefficient, it shows consistent tendency with the bed shear stress. At the first two locations, the mean friction coefficient in the uprush and backwash present similar magnitudes. However, the friction coefficient during the late backwash shows a less magnitude and turns to become larger at the very late backwash at location 1 compared with that at location 2. And this also is true for that at location 3 for the WWDFOV with a less magnification factor, where the friction coefficients both in the uprush and backwash show larger values than that at the first two locations. It can be guessed if using the same larger magnification factor at location 3; the estimated friction coefficients should be much larger. Although the magnitude of the estimated friction coefficient largely depends on the choice of the free stream velocity, the general tendency is almost similar, with a similar magnitude at the uprush and backwash. In the future study, the criteria used to decide the free stream velocity that used in the friction coefficients calculation should be developed. Since now the comparisons between different studies cannot be directly made because of different choices of the free stream velocity.

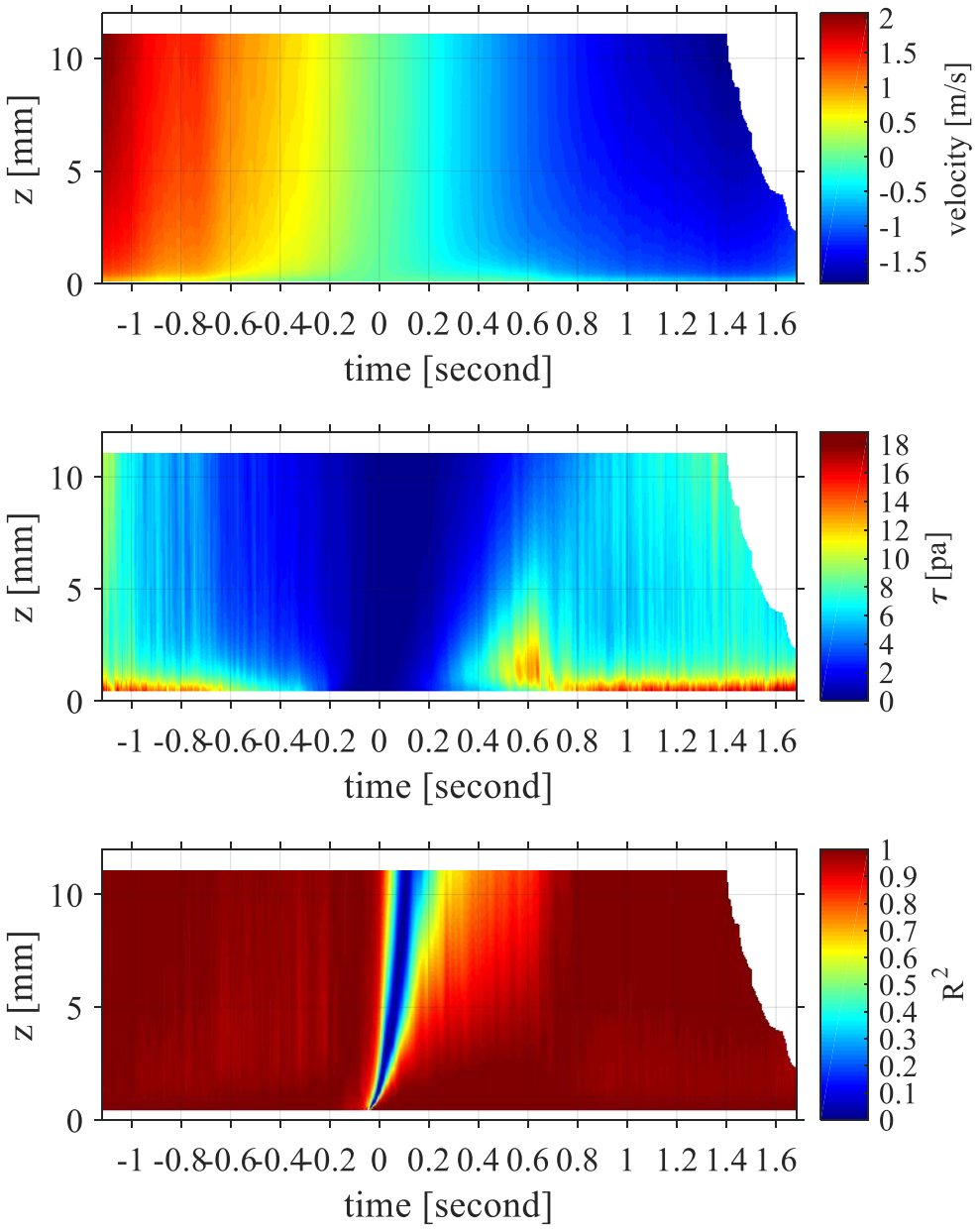

Figure 5-13 Distribution of velocity (first panel), estimated bed shear stress at different fitting elevations (second panel), and correlation coefficient (third panel) for BBLFOV at L1.

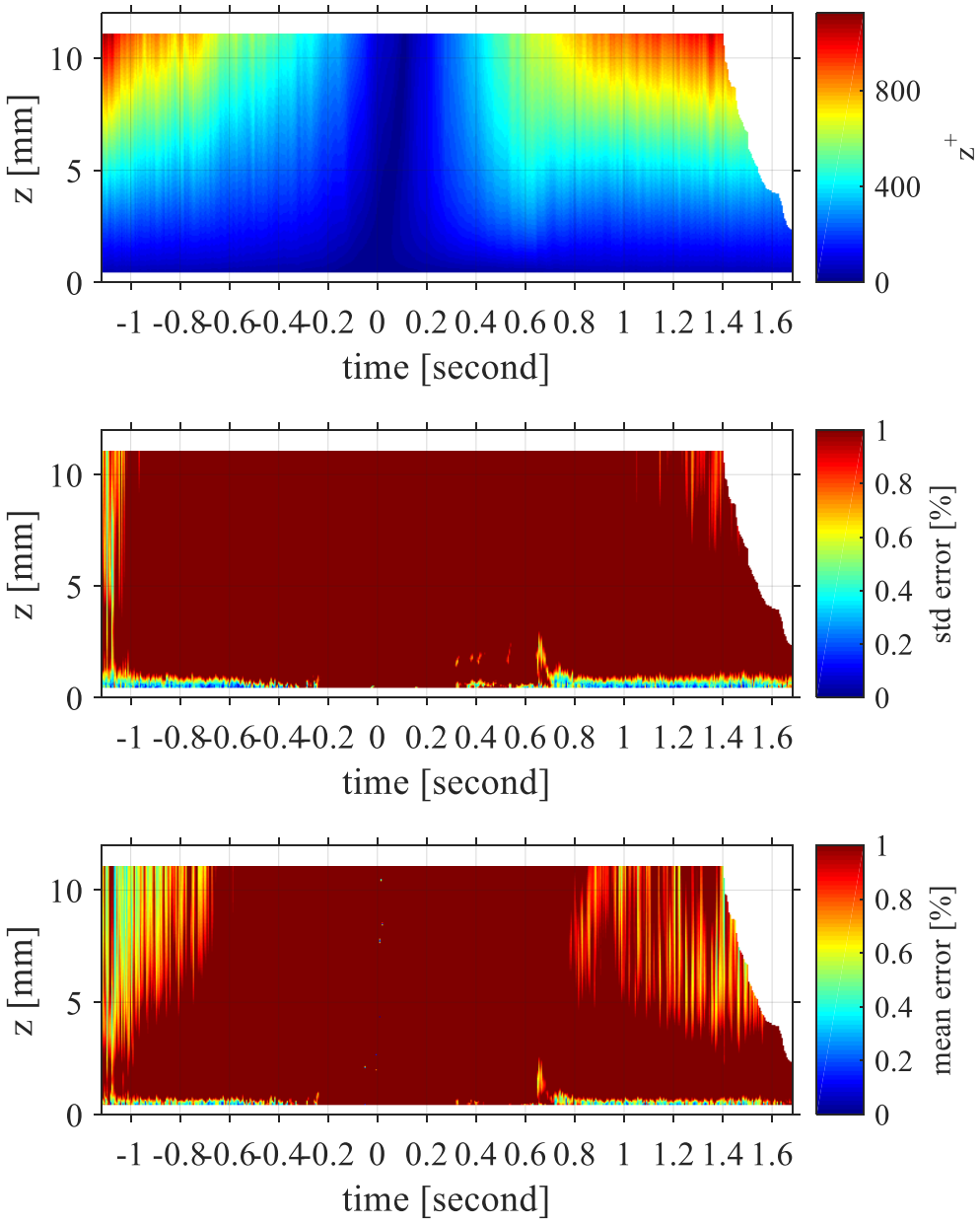

Figure 5-14 Distribution of non-dimensional wall unit (first panel), standard deviation of errors (second panel), and mean errors (third panel) for BBLFOV at L1.

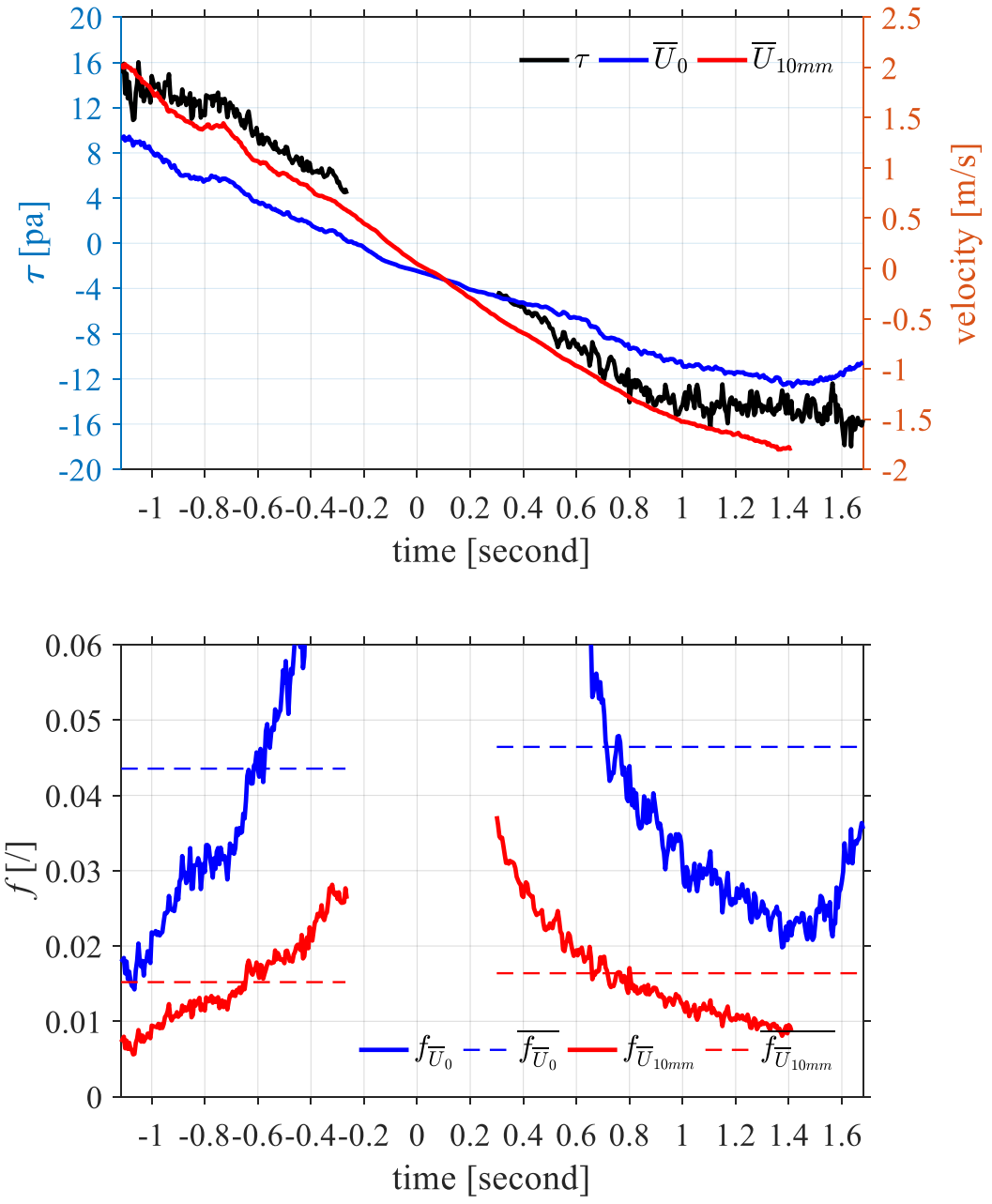

Figure 5-15 Time series of bed shear stress and velocities at the chosen fitting elevation and the 10mm elevation (first panel); corresponding friction coefficient (second panel) for BBLFOV at L1.

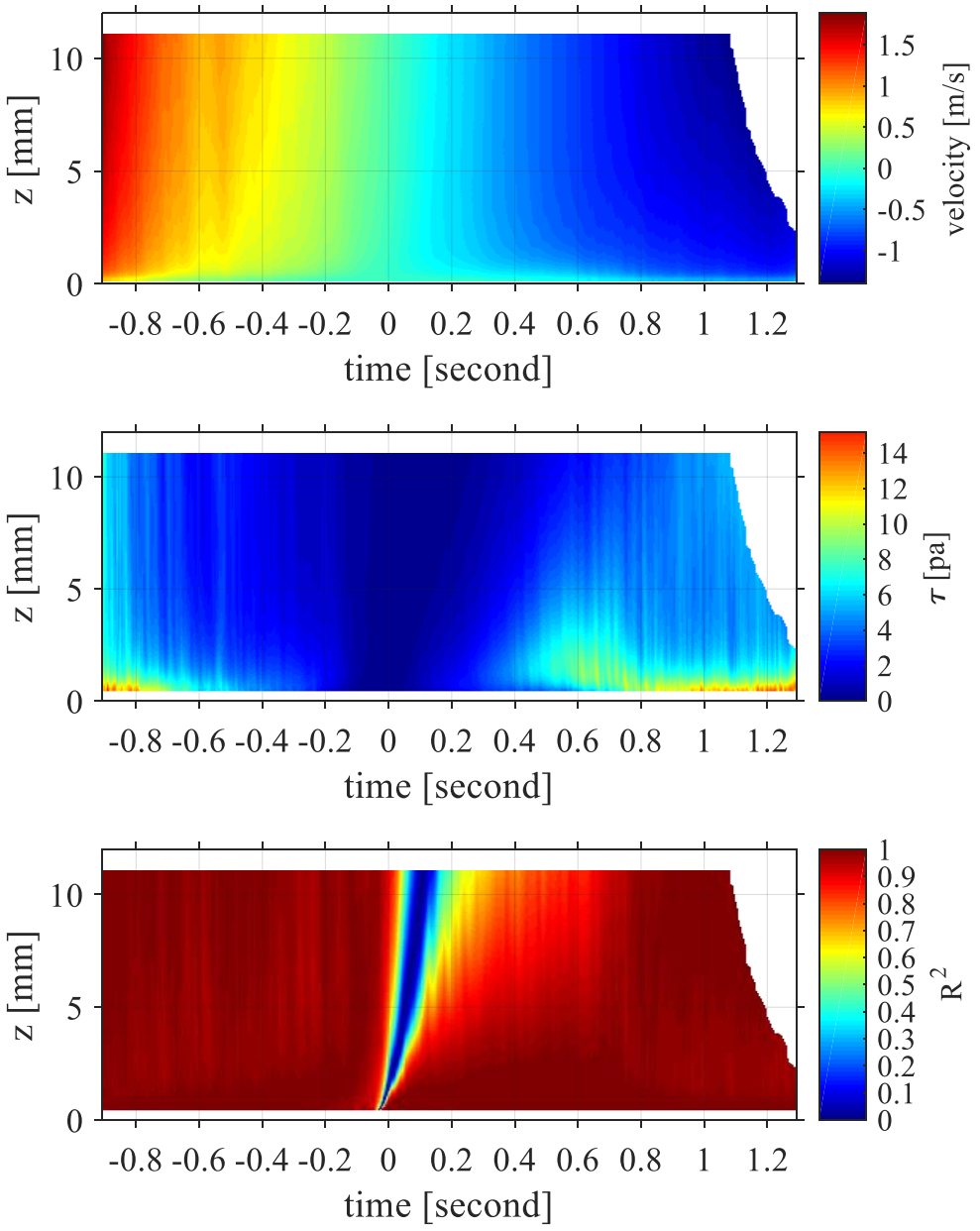

Figure 5-16 Distribution of velocity (first panel), estimated bed shear stress at different fitting elevations (second panel), and correlation coefficient (third panel) for BBLFOV at L2.

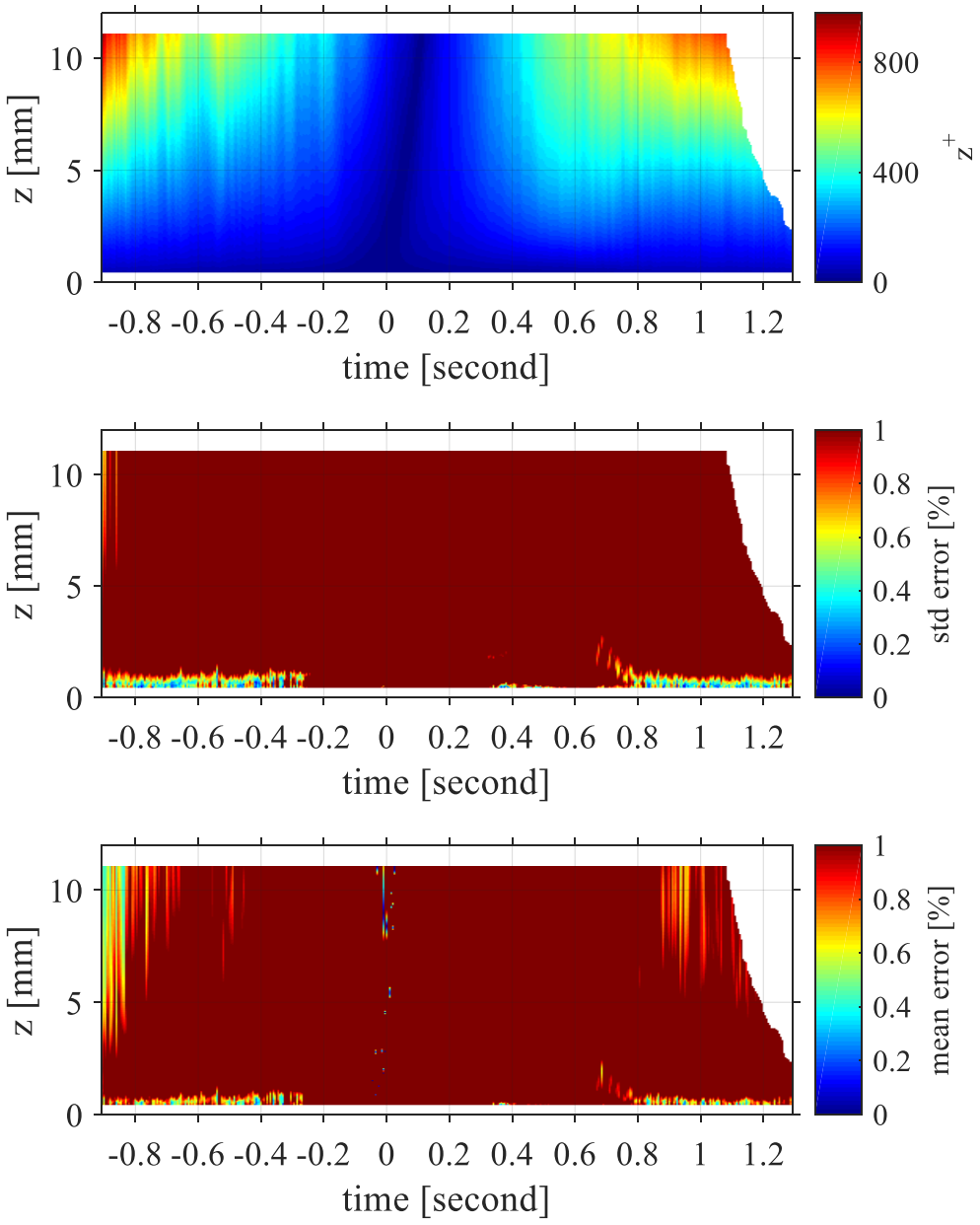

Figure 5-17 Distribution of non-dimensional wall unit (first panel), standard deviation of errors (second panel), and mean errors (third panel) for BBLFOV at L2.

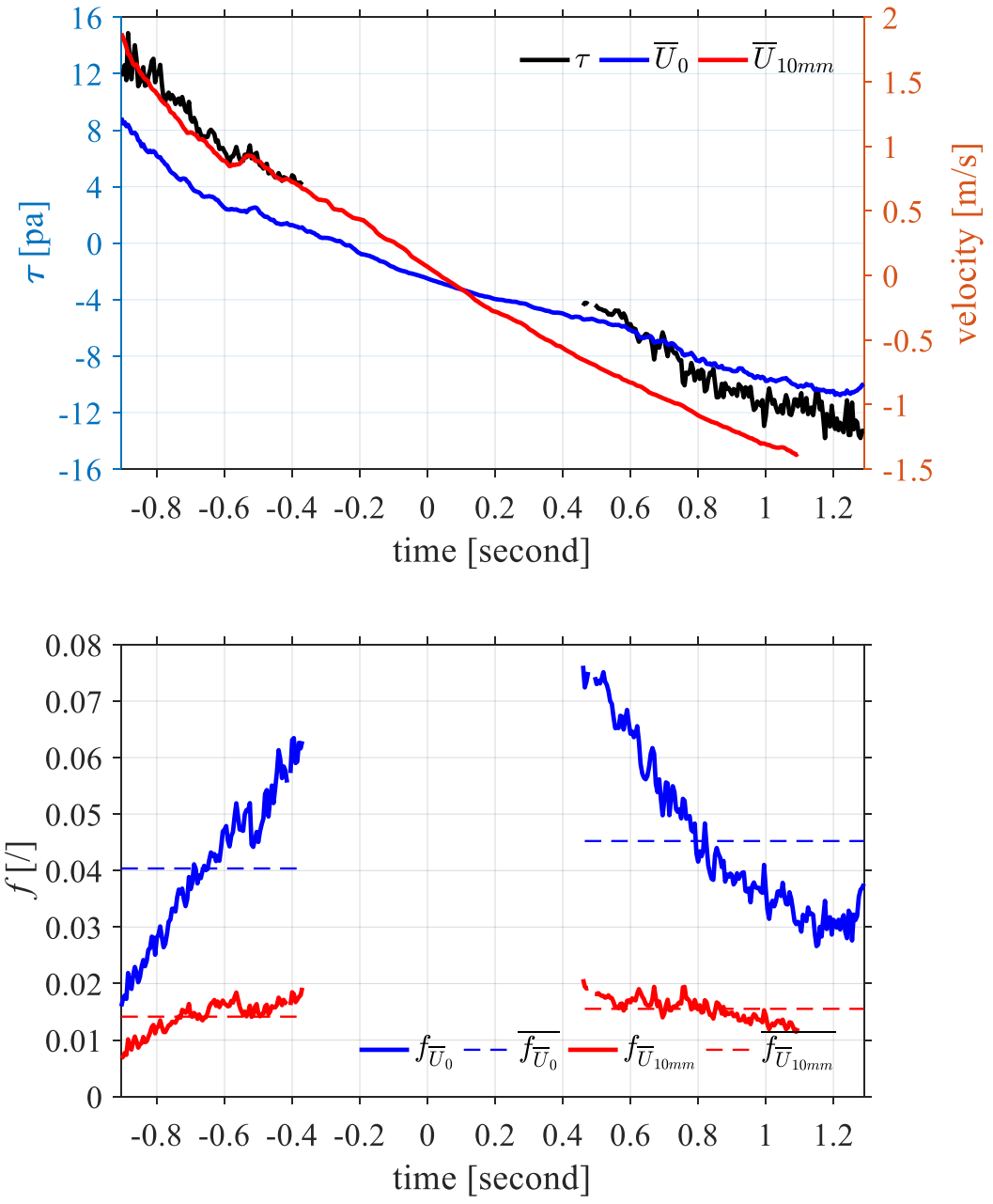

Figure 5-18 Time series of bed shear stress and velocities at the upper fitting elevation and the 10mm elevation (first panel); corresponding friction coefficient (second panel) for BBLFOV at L2.

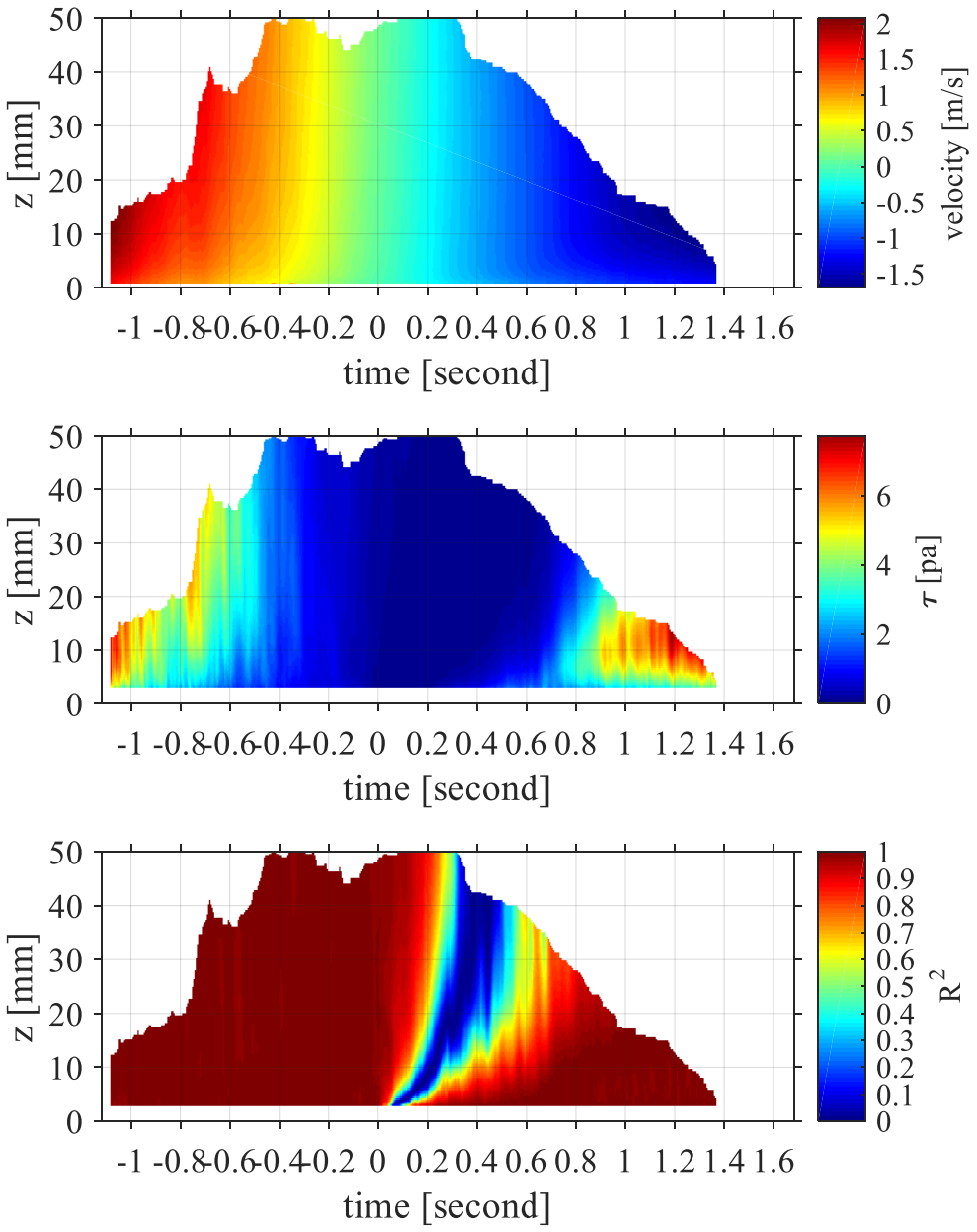

Figure 5-19 Distribution of velocity (first panel), estimated bed shear stress at different fitting elevations (second panel), and correlation coefficient (third panel) for WWDFOV at L1.

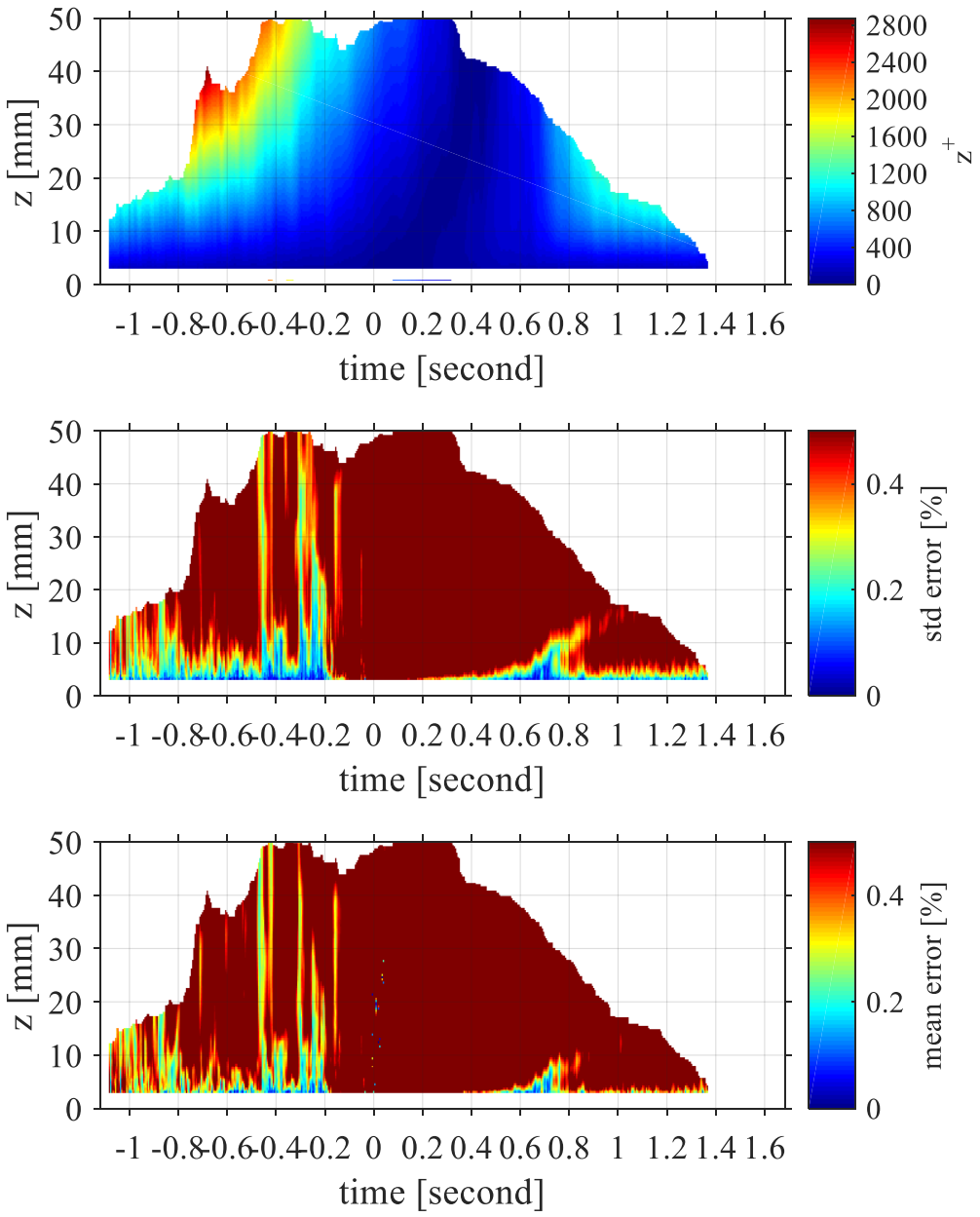

Figure 5-20 Distribution of non-dimensional wall unit (first panel), standard deviation of errors (second panel), and mean errors (third panel) for WWDFOV at L1.

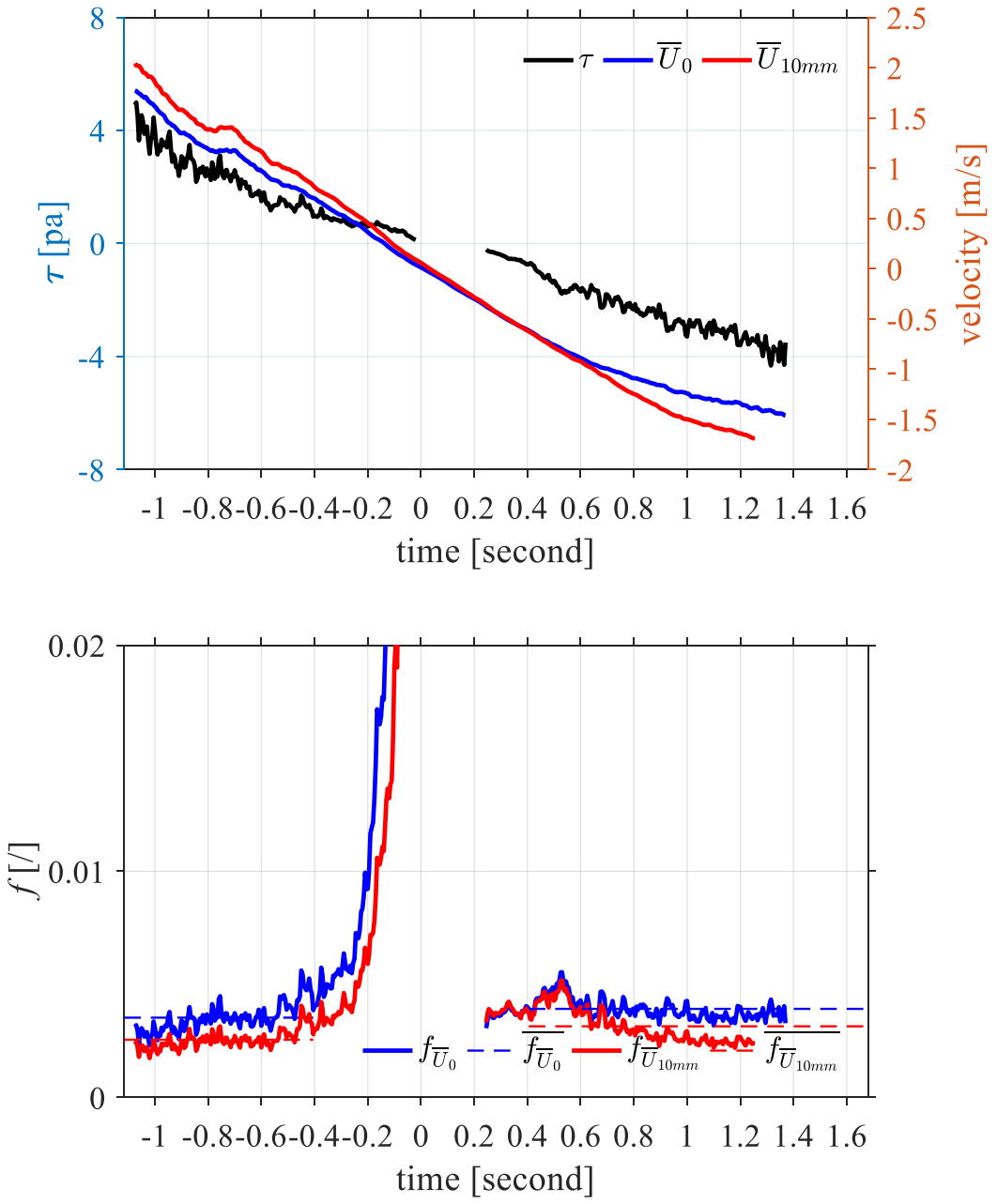

Figure 5-21 Time series of bed shear stress and velocities at the chosen fitting elevation and the 10mm elevation (first panel); corresponding friction coefficient (second panel) for WWDFOV at L1.

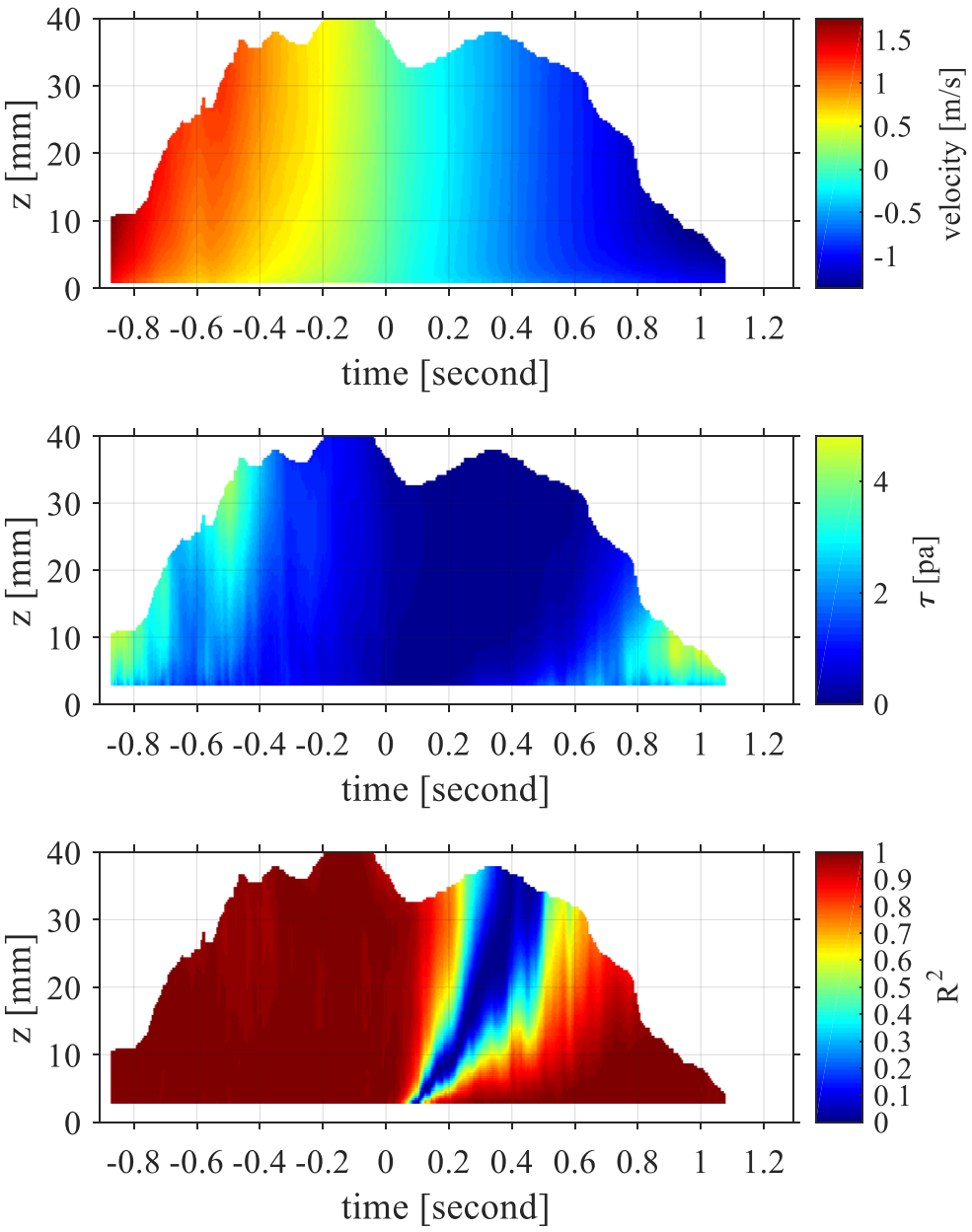

Figure 5-22 Distribution of velocity (first panel), estimated bed shear stress at different fitting elevations (second panel), and correlation coefficient (third panel) for WWDFOV at L2.

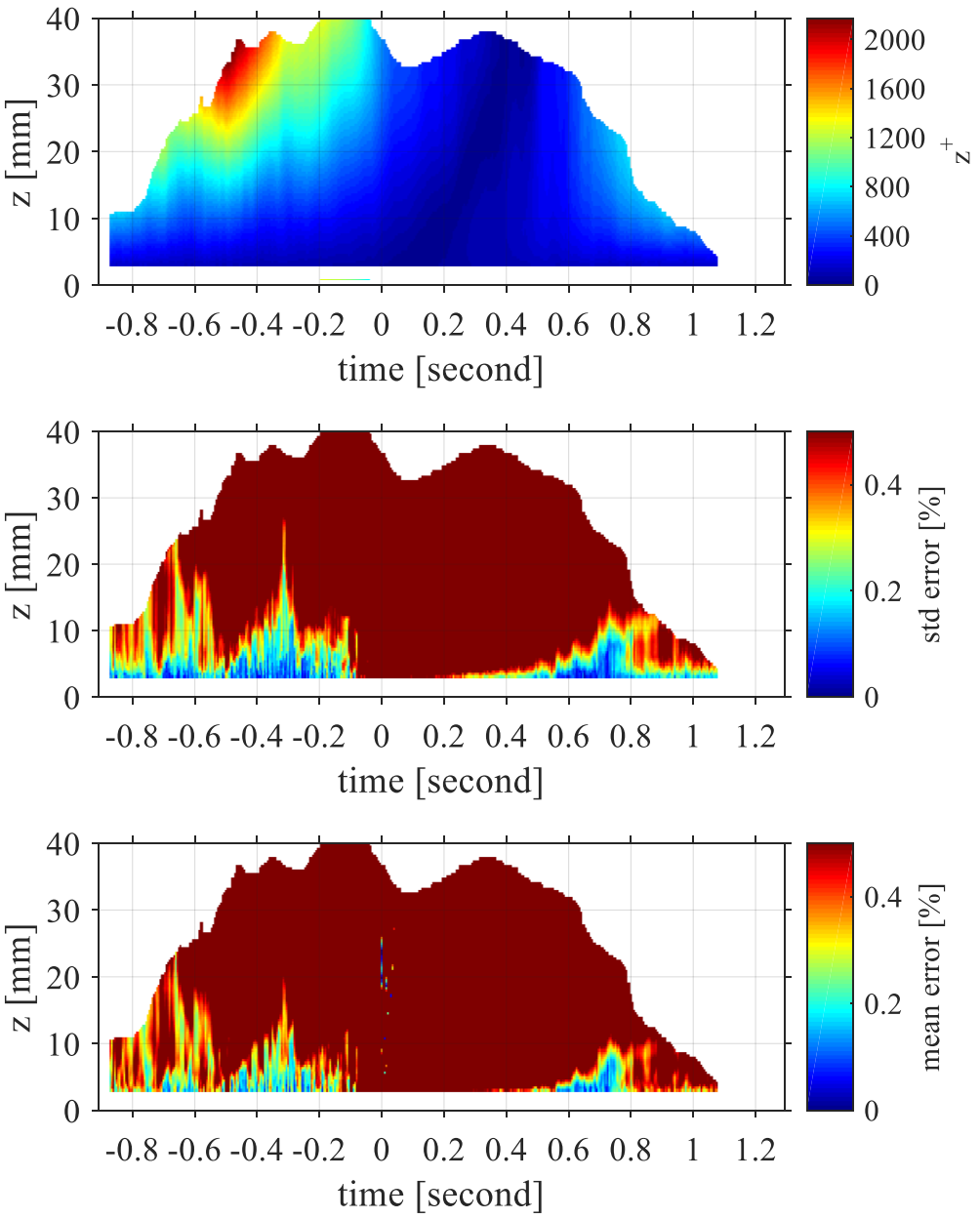

Figure 5-23 Distribution of non-dimensional wall unit (first panel), standard deviation of errors (second panel), and mean errors (third panel) for WWDFOV at L2.

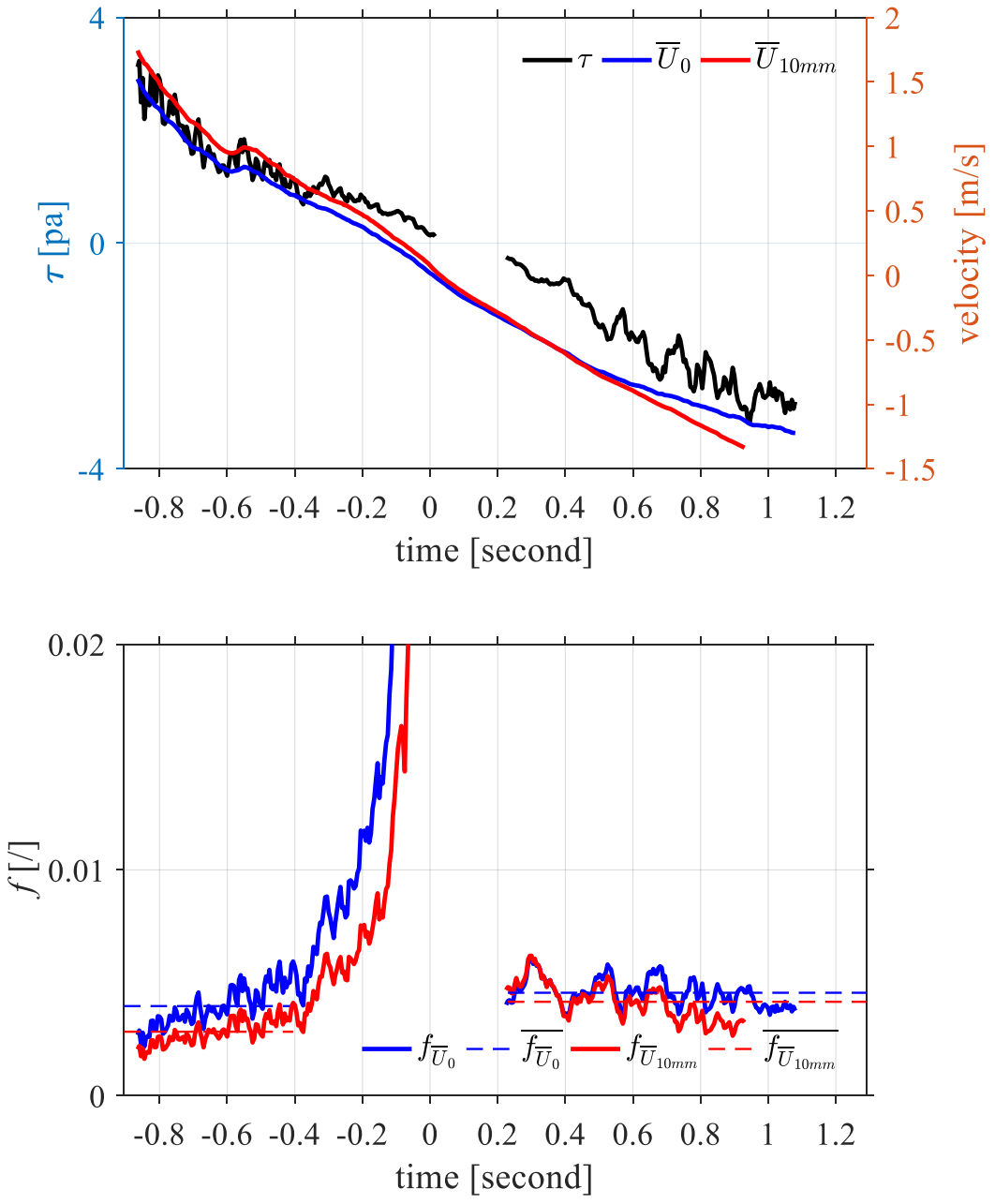

Figure 5-24 Time series of bed shear stress and velocities at the chosen fitting elevation and the 10mm elevation (first panel); corresponding friction coefficient (second panel) for WWDFOV at L2.

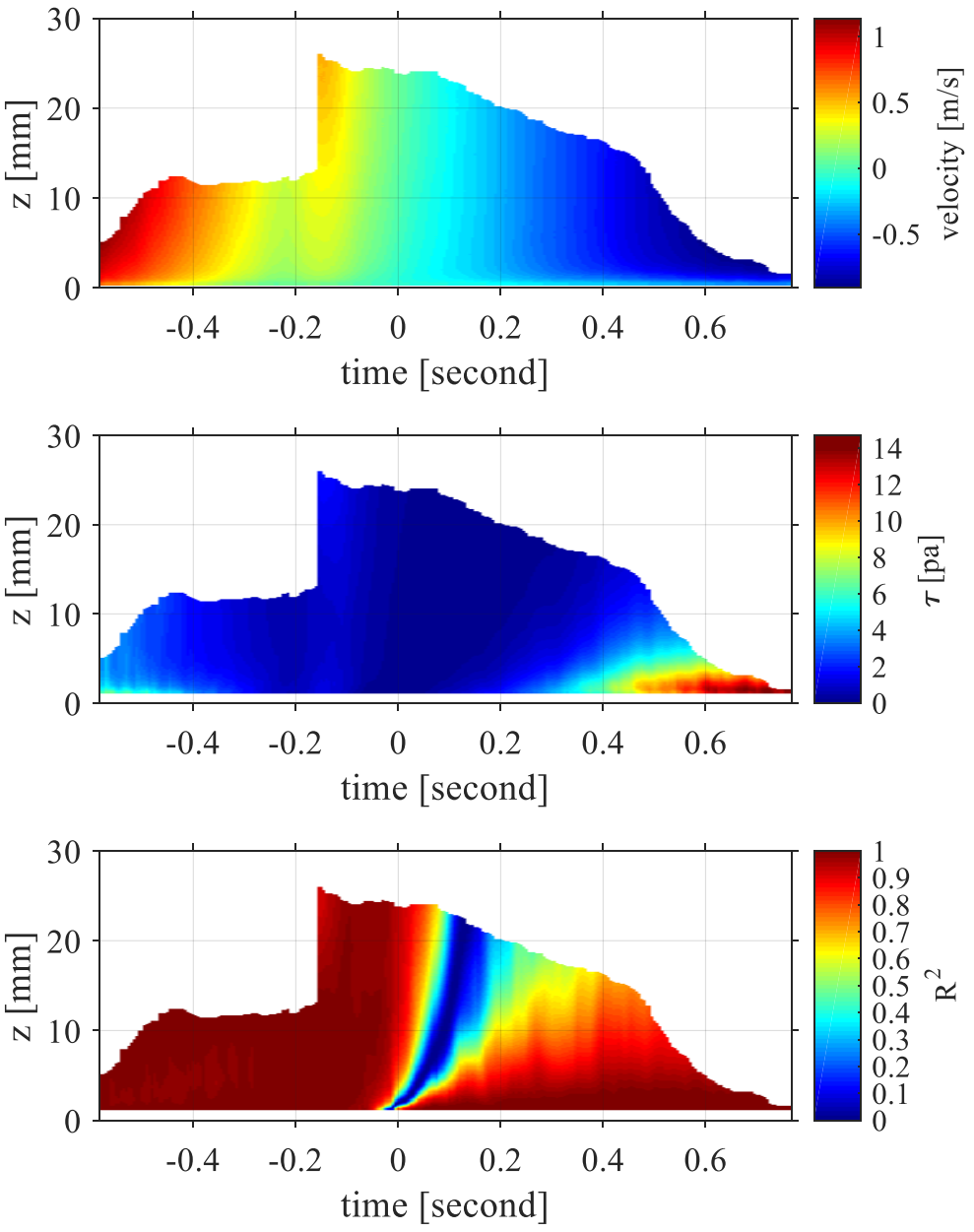

Figure 5-25 Distribution of velocity (first panel), estimated bed shear stress at different fitting elevations (second panel), and correlation coefficient (third panel) for WWDFOV at L3.

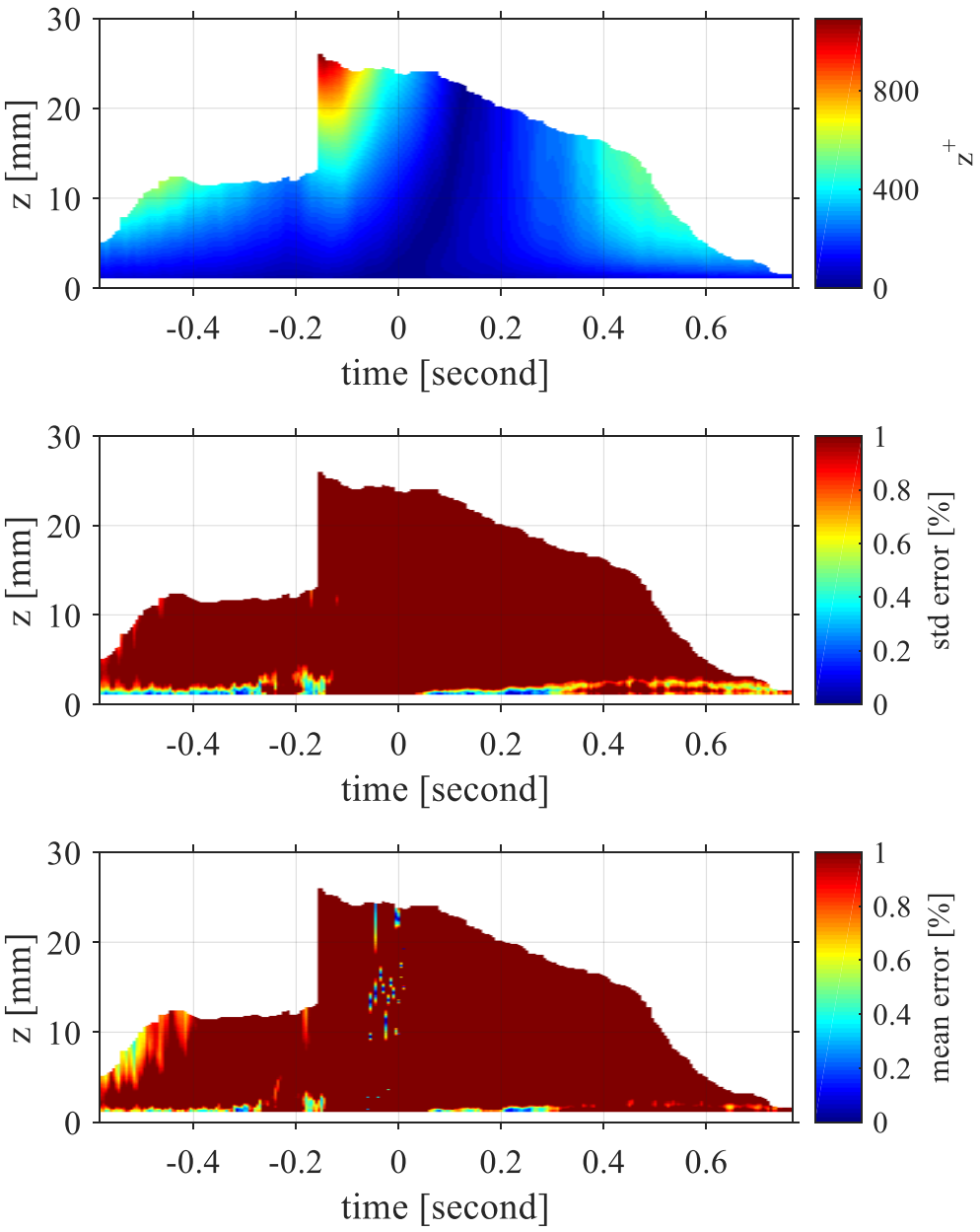

Figure 5-26 Distribution of non-dimensional wall unit (first panel), standard deviation of errors (second panel), and mean errors (third panel) for WWDFOV at L3.

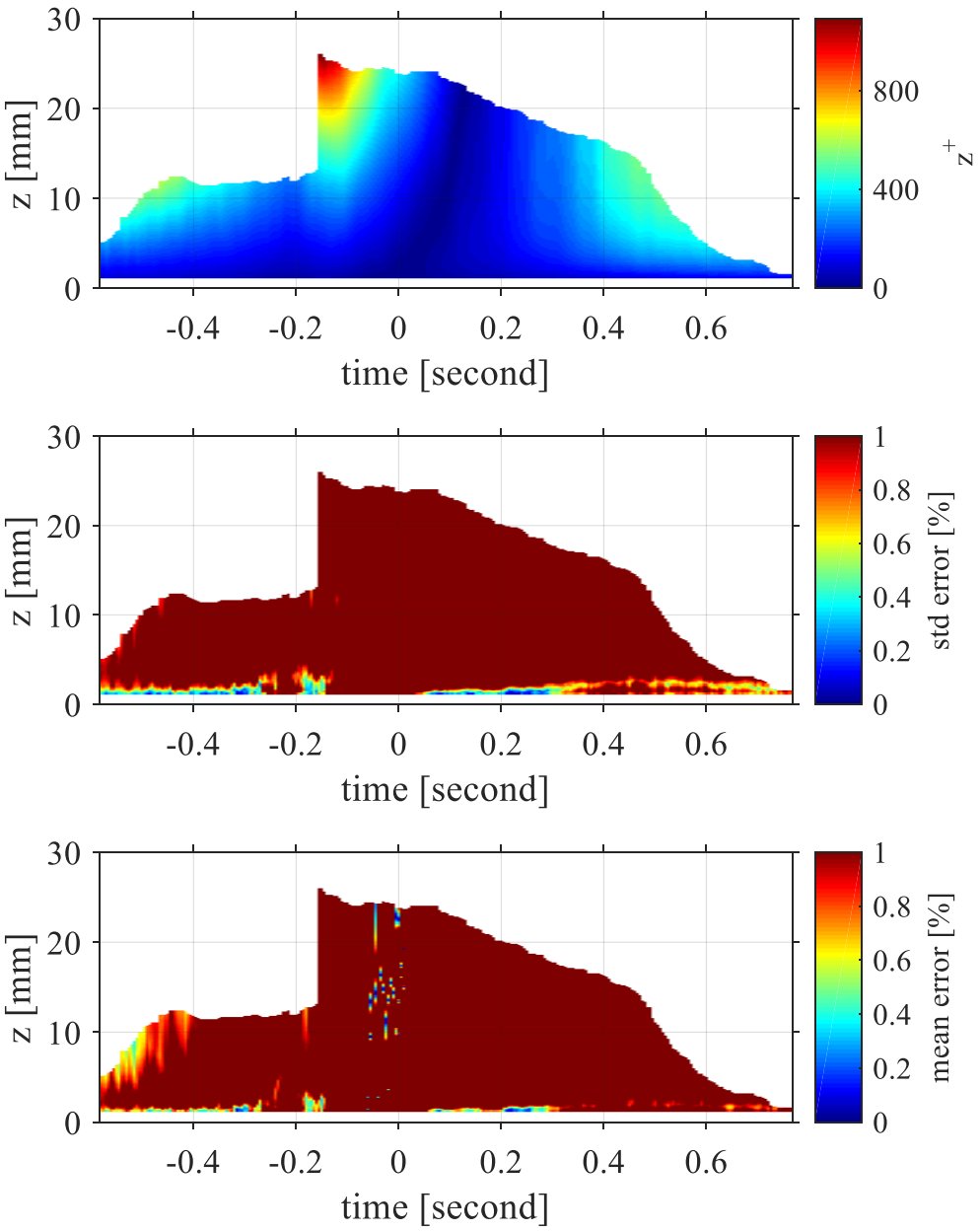

Figure 5-27 Distribution of non-dimensional wall unit (first panel), standard deviation of errors (second panel), and mean errors (third panel) for WWDFOV at L3.

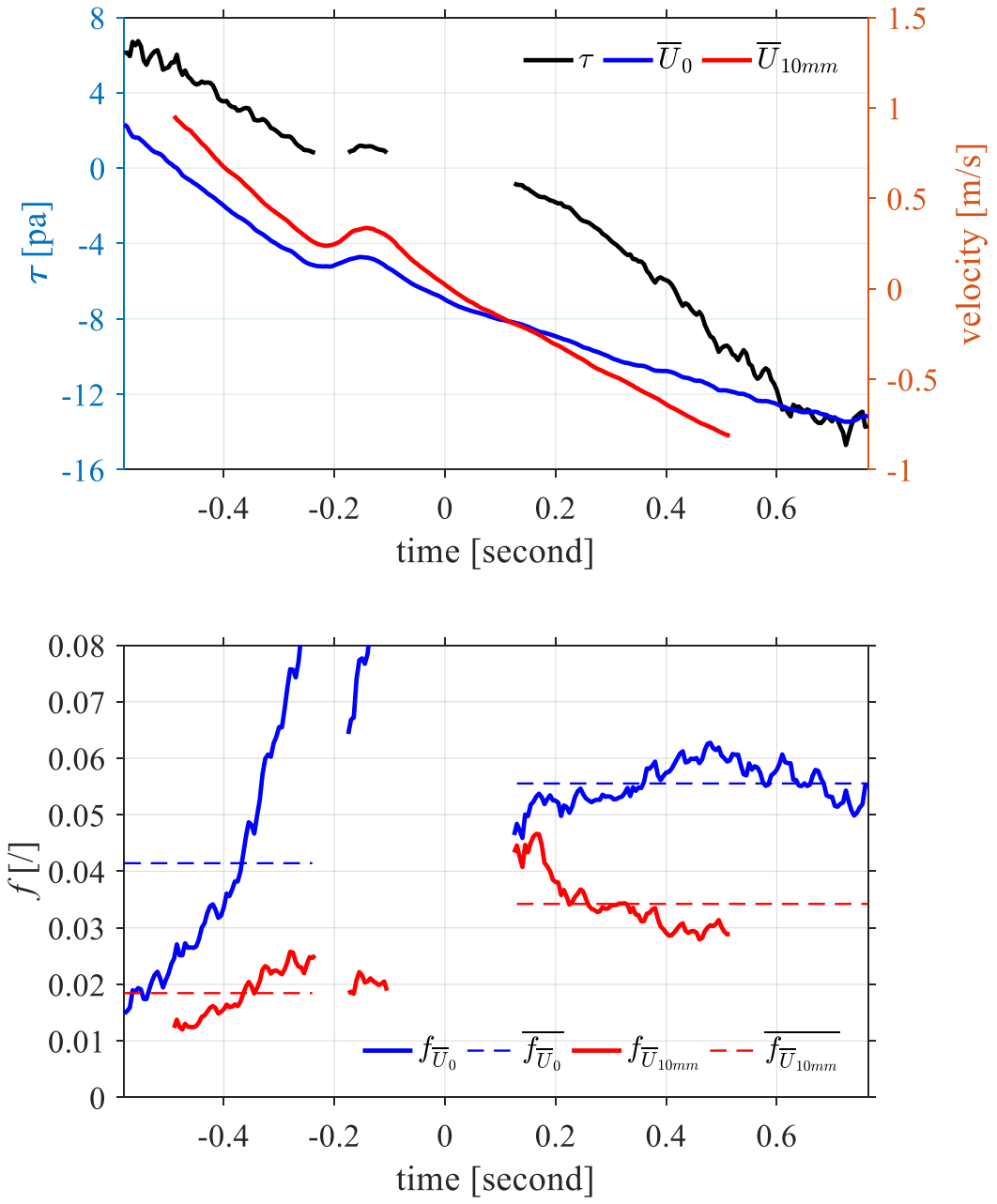

Figure 5-28 Time series of bed shear stress and velocities at the chosen fitting elevation and the 10mm elevation (first panel); corresponding friction coefficient (second panel) for WWDFOV at L3.

5.5 Conclusions

A large-scale experiment aims at investigating the bottom boundary layer with a BBLFOV together with a coarse resolution measurement with a WWDFOV for comparisons have been done. The experiments were conducted for 100 times at each location, with the first 50 times using the BBLFOV and the second 50 times using the WWDFOV. Then the PIV recordings were analyzed using advanced algorithm so as to make high resolution measurements. The 50 individual swash events then were ensemble averaged to investigate the general characteristics. The main conclusions from this large-scale experiments were summarized as follows.

The velocity profiles show a similar tendency to that in the small-scale experiment with a larger measured maximum uprush velocity than that of the backwash. The velocity profiles show a typical forward leaning shape in the uprush and then become depth-uniform close to the stage of flow reversal. During the flow reversal, the flow close to the bottom changes direction firstly compared with that in the upper layer resulting in an apparent phase lead phenomenon. Different from that in the small-scale experiment, the phase lead phenomenon lasts only for portion of the backwash. However, it should be pointed out that the velocity profiles below the surface are not successfully calculated because of the less accurate detection of the free surface. By using the advanced PIV technique, the lowest measurement point is 0.126 mm from the bottom, and 40 points were obtained within the lowest 2mm, thus the velocity field within the bottom boundary layer can be greatly resolved. At location 3, the phenomenon of mini bore is observed and the velocity field under the mini bore is successfully

measured for the first time in the laboratory. Because it is out of the scope of the current study, the detailed description of the mini bore is not included in this thesis.

TKE level is estimated by using ensemble averaging method considering the high repeatability of the experiment. From location 1 to location 3, the TKE is decreasing because of the dissipation of the surface-related turbulence and the decreasing velocity magnitude. At location 1, the high TKE in the uprush is considered to be the results of the surface-related turbulence and bed-related turbulence, and the backwash TKE is only due to the bed-related turbulence. Thus, the TKE level in the uprush is 2-3 times larger than that in the backwash. At location 2, although the effects of surface-related turbulence still exist, the contribution to the total TKE is decreasing. Thus the uprush TKE is only a little larger than the backwash TKE level. At location 3, almost due to the entire dissipation of the surface-related turbulence, the TKE in the uprush shows similar magnitude of that in the backwash. The TKE based on the high-resolution data shows a slight larger value than that estimated by the coarse resolution data, indicating that the high-resolution measurement can detect more small scale turbulence.

The bed shear stress is estimated using log-law method in this study by taking the effects of correlation coefficients, non-dimensional wall unit and fitting error into consideration. At the three locations, the peak backwash bed shear stress shows a similar or greater magnitude than that in the uprush, which is contrast to most of the previous studies, where the measurement is done in the inner swash zone. However, the results show that the bed shear stress estimated using

high resolution data can be 2-3 times larger than that estimated using coarse resolution data. The results using high resolution data are obtained by fitting the velocity profile from the lowest point 0.126 mm to the 0.46 mm to the log profile. However, the results obtained by using coarse resolution are estimated by fitting the velocity profile from the lowest point 0.98 mm to the 2.836 mm to the log profile. Although there is no evidence to directly clarify which result is better, the fitting elevation from the lowest 0.126 mm to 0.46 mm seems to be more appropriate than that from 0.98 mm to the 2.836 mm. The magnitudes of friction coefficient largely depend on the choice of free stream velocity. Dramatic difference can be obtained when different free stream velocities are used since the friction coefficient is in inverse proportion to the square of the free stream velocity. But the general tendency is similar for the three measurement locations with a slight larger value in the backwash than that in the uprush.

Chapter 6 Conclusions and future work

6.1 Conclusions

The objectives of the work were to gain a better understanding of the flow of (bore) waves on (plane, impermeable, smooth) beaches, including the spatiotemporal distribution of velocity, turbulence and bed shear stress to improve the knowledge of the hydrodynamic processes occurring in the shallow swash zone. The work is divided into three separate parts: development of advanced PIV technique, the small-scale swash experiment and large-scale swash experiment.

Firstly, by recognizing the limitations of the commercial and open-source PIV software, an advanced PIV program was successfully developed by using modified FFT method as proposed by (Ronneberger et al., 1998) to overcome the circular effects caused by normal FFT method and keep the high computation speed as that in the direct cross correlation method. Considering the fact that in the swash zone, the bed-parallel velocity is much larger than the bed-normal velocity in almost all the swash duration, except during the flow reversal, where magnitudes of velocities of the two directions are both very small, and the vertical velocity gradient is relatively large. Considering the above-mentioned fact and with the aim to improve the measurement resolution in the bed-normal direction, in this study, the interrogation window size was set to be rectangle with a relative larger dimension in the bed-parallel direction and a smaller dimension in the bed-normal direction as suggested by (Liu Philip et al., 2007). By using the

advanced PIV technique, the velocity field within the bottom boundary layer is successfully resolved. The calculated velocity vectors were then post-processed by using the statistical method of Grubbs Test.

Secondly, with the main aim of comparing the TKE results estimated using the ensemble average and moving average methods, the experiment was conducted in the small-scale dam-break flume so as to make high temporal resolution PIV measurements by using the continuous wave laser as light source to illuminate the seeding particles and use the high-speed CCD camera (2000 frames per second) to record the illuminated seeding particles. It is almost impossible to apply the continuous wave laser in the large-scale dam-break flume of high incident bore velocity since the relative low energy output of the laser are not high enough to be sensed by the high-speed CCD camera within a very short shutter speed.

The velocity profiles show a typical forward leaning shape during the uprush and then become to be depth-uniform close to the flow reversal, at which the flow close to the bottom changes direction firstly compared with that in the upper layer. After that, during the flow reversal, the phase lead is formed and lasts for almost the entire backwash duration, which is different from the previous studies that measurements were done in inner swash zone, where the phase lead only exists for a short time after flow reversal. This may be caused by the less swash duration in the shallow swash zone, where there is not enough time for the backwash flow to reestablish the velocity profiles. The velocity profiles in the uprush show the peak value just below the surface, which is caused by the opposite direction of vorticities in the upper layer and lower layer of the bore front

as explained by (Watanabe et al., 2013). Consistent with the previous studies, the measured maximum uprush is larger than the measured maximum backwash velocity, although the actual maximum uprush and backwash velocities should be larger than the measured one. The uprush duration is less than the backwash duration, indicating the asymmetry of the swash flow in time (Kikkert et al., 2012; O'Donoghue et al., 2010).

Although the moving average method can reveal the local characteristics of the turbulence, it is still difficult to decide the moving window size (cut-off frequency). In this study, with the aim to find the tendency of the TKE in the swash zone rather than the actual magnitude, the TKE is estimated by using 4 cut-off frequencies. All of the results show similar tendency that the uprush TKE is larger than the backwash TKE with less TKE level close to the surface, indicating that in the shallow swash zone the main source of TKE is from the bottom rather than the surface. This is easy to understand when considering the distance between the measurement in the shallow swash zone and the location of bore collapse. However, it is found that the TKE level estimated using ensemble average is one order of magnitude higher than that estimated using moving average, showing the uncertainty of the results from ensemble average because of the difficulty in achieving perfect repeatability in practice.

Bed shear stress results from momentum integral method and linear fitting method show that these two methods are not suitable for the shallow swash zone. To make direct comparisons between previous studies easily, log-law is adopted to estimate the bed shear stress. The upper limit of the log fitting is decided by taking the following parameters into consideration: the correlation coefficient, the

non-dimensional wall unit and the fitting error. Results show that the measured peak uprush bed shear stress is larger than the measured peak backwash bed shear stress, which is contrast to that in the inner swash zone, where the measured peak uprush bed shear stress is larger than the measured peak backwash bed shear stress. Consistent with the tendency of the bed shear stress, the measured non-dimensional bed shear stress, friction coefficient, is larger in the backwash.

Thirdly, although the small-scale swash experiment already reveals the main hydrodynamics in the shallow swash zone and the distinct parts compared with the previous studies, the comparisons between results estimated using high resolution and coarse resolution data are still not easy to be made. Also the scale should have effect on the results. With the main aim to compare the results estimated using different resolution velocity data, the large-scale swash experiment using high performance YAG laser and CCD camera mounted with large magnification lens and small magnification lens was done at three measurement locations in the shallow swash zone to investigate the bottom boundary layer characteristics and compare the results estimated using high/coarse resolution velocity data.

The velocity profiles show a similar tendency to that of the small-scale experiment. However, the measurement resolution is improved with lowest measurement location being resolved to 0.126 mm from the bottom and 20 measurements points were successfully obtained within the lowest 1 mm. At location 3, the mini bore-collapse phenomenon, which was firstly detected by the numerical simulation study, was observed and the velocity field under the mini

bore-collapse was measured for the first time in the laboratory. Due to the difficulty in determining accurately the free surface, the velocities in the vicinity of the surface are not taken into consideration, leading to the less obvious phenomenon, which is very apparent in the small-scale experiment that the uprush velocity peaks just below the free surface. The TKE was estimated using ensemble average method because that the less high pulse laser rate prohibits the application of moving average method to estimate TKE. The results show that from the lower location to the upper location, the TKE is decreasing with the dissipation of surface-related turbulence and decreased velocity magnitude. In the lower location, the uprush TKE is 2 times larger than that in the backwash. However, in the upper location, the uprush and backwash TKE have similar magnitude, implying that the effect of surface-related turbulence has decreased to the minimum. At all locations, the TKE results estimated using high resolution velocity data give larger value, revealing that the high-resolution data can resolve the small-scale turbulence well. Bed shear stress estimated by log-law shows similar tendency with that in the small-scale experiment with the peak backwash bed shear stress is similar or larger than the peak uprush bed shear stress. However, the results estimated by fitting the velocity profile from the lowest point 0.126 mm to the 0.46 mm to the log profile using high resolution is 2-3 times larger than that estimated by fitting the velocity profile from the lowest point 0.98 mm to the 2.836 mm to the log profile using coarse resolution data. This is the first time that comparisons like this were made and no previous studies can estimate shear stress within this thin layer because of the difficulty in measuring the velocity in such shallow area. The magnitudes of friction coefficient largely depend on the choice of free stream velocity. Dramatic difference can be obtained

when different free stream velocities are used since the friction coefficient is in inverse proportion to the square of the free stream velocity. But the general tendency is similar for the three measurement locations with a slight larger value in the backwash than that in the uprush.

6.2 Future work

This work has shown the comprehensive results from the small-scale and large-scale experiments with promising outcomes when high resolution measurement was employed. However, in this study, the measurements were made in the upper swash zone, it is better to make measurements through the entire swash zone (the lower, the mid, the upper swash zone) so as to make comparisons among the results from all the locations. Then more reliable and logical conclusions can be made. What's more, the current study was done on smooth bed without taking the roughness, which is very important in modeling actual bed, into consideration. In the future, the large-scale experiments using high resolution measurement in rough bed should be conducted so as to figure out the effect of roughness on the swash hydrodynamics. Fundamental research of this kind, is a prerequisite to sediment transport modelling and ultimately the knowledge gained from such research must be incorporated into practical tools for predicting beach response to wave action

Appendix

A.1 Process of FFT calculation

```
clear;clc;close all

w1=[4,4,5,4,5,2;4,2,2,2,5,2;2,1,3,3,3,4;4,3,2,4,2,2];

w2=[4,2,2,5,3,3;2,2,4,2,3,4;5,3,3,4,1,5;2,3,3,4,1,2];

R=fftshift(real(ifft2(fft2(w2).*conj(fft2(w1)))))

r0=sum(sum(w1.*w2))

t1=[w1(2:end,:);w1(1,:)];

r1=sum(sum(t1.*w2))

t2=[w1(3:end,:);w1(1:2,:)];

r2=sum(sum(t2.*w2))

t3=[w1(:,2:end),w1(:,1)];

r3=sum(sum(t3.*w2))
```

A.2 Kernel parts of the modified PIV alogrithm

```
clear;clc;close all
load('image1.mat');
load('image2.mat');
ky=400.5;kx=400.5;yup=5;ydown=5;
xleft=20;xright=20;
window_height=16;window_width=96;
m=zeros(window_height+yup+ydown,window_width+xleft+xright);
m(yup+1:end-ydown,xleft+1:end-xright)=1;
const=1/(window_height*window_width);
f1=fft2(m);
w1=image1(ky-(window_height-1)/2-yup:ky+(window_height-1)/2+ydown,kx-(w
indow_width-1)/2-xleft:kx+(window_width-1)/2+xright);
w2=image2(ky-(window_height-1)/2-yup:ky+(window_height-1)/2+ydown,kx-(w
indow_width-1)/2-xleft:kx+(window_width-1)/2+xright);
RR=fftdcc(const,m,f1,w1,w2);% kernel
R=RR(floor(size(RR,1)/2)+1-yup:floor(size(RR,1)/2)+1+ydown,floor(size(RR,2)/2)
+1-xleft:floor(size(RR,2)/2)+1+xright);
```

```
function tt=fftdcc(const,m,f1,w1,w2)

f2=fft2(w2);

t0=fftshift(ifft2(f2.*conj(fft2(m.*w1))));

t1=const*(sum(sum(m.*w1)));

t2=fftshift(ifft2(f2.*conj(f1)));

t3=sqrt(sum(sum((m.*w1).^2))-const.*(sum(sum(m.*w1))).^2);

t4=sqrt(fftshift(ifft2(fft2(w2.*w2).*conj(f1)))-const.*(t2).^2);

tt=(t0-t1.*t2)./t3./t4

end
```

Reference

Aagaard, T., & Hughes, M. G. Sediment suspension and turbulence in the swash zone of dissipative beaches. Marine Geology, 228(1), 117-135, (2006).

Adrian, R. J. Particle-imaging techniques for experimental fluid mechanics. Annual review of fluid mechanics, 23(1), 261-304, (1991).

Alsina, J. M., Cáceres, I., Brocchini, M., & Baldock, T. E. An experimental study on sediment transport and bed evolution under different swash zone morphological conditions. Coastal Engineering, 68, 31-43, (2012).

Austin, M. J., Masselink, G., Russell, P., Turner, I., and Blenkinsopp, C. Alongshore fluid motions in the swash zone of a sandy and gravel beach. Coastal Engineering, 58(8), 690–705, (2011).

Alsina, J. M., Falchetti, S., & Baldock, T. E. Measurements and modelling of the advection of suspended sediment in the swash zone by solitary waves. Coastal Engineering, 56(5), 621-631, (2009)

Archetti, R., & Brocchini, M. An integral swash zone model with friction: an experimental and numerical investigation. Coastal Engineering, 45(2), 89-110, (2002).

Austin, M. J., & Masselink, G. Swash–groundwater interaction on a steep gravel beach. Continental Shelf Research, 26(20), 2503-2519, (2006).

Bakhtyar, R., Barry, D. A., Li, L., Jeng, D. S., & Yeganeh-Bakhtiary, A. Modeling sediment transport in the swash zone: A review. Ocean Engineering, 36(9), 767-783, (2009).

Baldock, T. E., & Hughes, M. G. Field observations of instantaneous water slopes and horizontal pressure gradients in the swash-zone. Continental Shelf Research, 26(5), 574-588, (2006).

Barnes, M.P., Baldock, T., Direct bed shear stress measurements in bore-driven swash and swash interactions. Coastal Sediments '07, pp. 1947–1960, (2007).

Barnes, M. P., O'Donoghue, T., Alsina, J. M., & Baldock, T. E. Direct bed shear stress measurements in bore-driven swash. Coastal Engineering, 56(8), 853-867, (2009).

Barnes, M. P., & Baldock, T. E. A Lagrangian model for boundary layer growth and bed shear stress in the swash zone. Coastal Engineering, 57(4), 385-396, (2010).

Blenkinsopp, C. E., Mole, M. A., Turner, I. L., & Peirson, W. L. Measurements of the time-varying free-surface profile across the swash zone obtained using an industrial LIDAR. Coastal Engineering, 57(11), 1059-1065, (2010).

Briganti, R., Dodd, N., Pokrajac, D., & O'Donoghue, T. Non linear shallow water modelling of bore-driven swash: Description of the bottom boundary layer. Coastal Engineering, 58(6), 463-477, (2011).

Briganti, R., Torres-Freyermuth, A., Baldock, T. E., Brocchini, M., Dodd, N., Hsu, T. J., & Postacchini, M. Advances in numerical modelling of swash zone dynamics. Coastal Engineering, 115, 26-41, (2016).

Butt, T., Russell, P., Puleo, J., Miles, J., & Masselink, G. The influence of bore turbulence on sediment transport in the swash and inner surf zones. Continental Shelf Research, 24(7), 757-771, (2004).

Calantoni, J., & Puleo, J. A. Role of pressure gradients in sheet flow of coarse sediments under sawtooth waves. Journal of Geophysical Research: Oceans, 111(C1), (2006).

Chardón-Maldonado, P., Pintado-Patiño, J. C., & Puleo, J. A. Advances in swash-zone research: Small-scale hydrodynamic and sediment transport processes. Coastal Engineering, 115, 8-25, (2016).

Conley, D. C., & Griffin, J. G. Direct measurements of bed stress under swash in the field. Journal of Geophysical Research: Oceans, 109(C3), (2004).

Cowen, E. A., Mei Sou, I., Liu, P. L. F., & Raubenheimer, B. Particle image velocimetry measurements within a laboratory-generated swash zone. Journal of Engineering Mechanics, 129(10), 1119-1129, (2003).

Cox, D. T., Hobensack, W., & Sukumaran, A. Bottom stress in the inner surf and swash zone. In Coastal Engineering 2000(pp. 108-119), (2001).

Desombre, J., Morichon, D., & Mory, M. RANS v 2–f simulation of a swash event: Detailed flow structure. Coastal Engineering, 71, 1-12, (2013).

Erikson, L., Larson, M., & Hanson, H. Prediction of swash motion and run-up including the effects of swash interaction. Coastal Engineering, 52(3), 285-302, (2005).

Fredsøe, J., Deigaard, R. Mechanics of coastal sediment transport. World Scientific, 1992.

Elfrink, B., & Baldock, T. Hydrodynamics and sediment transport in the swash zone: a review and perspectives. Coastal Engineering, 45(3), 149-167, (2002).

Garcia, D. Robust smoothing of gridded data in one and higher dimensions with missing values. Computational statistics & data analysis, 54(4), 1167-1178, (2010).

Guard, P. A., & Baldock, T. E. The influence of seaward boundary conditions on swash zone hydrodynamics. Coastal Engineering, 54(4), 321-331, (2007).

Holland, K. T., Raubenheimer, B., Guza, R. T., & Holman, R. A. Runup kinematics on a natural beach. Journal of Geophysical Research: Oceans, 100(C3), 4985-4993，(1995).

Houser, C., & Barrett, G. Divergent behavior of the swash zone in response to different foreshore slopes and nearshore states. Marine geology, 271(1), 106-118, (2010).

Hsu, T. J., & Raubenheimer, B. A numerical and field study on inner-surf and swash sediment transport. Continental Shelf Research, 26(5), 589-598，(2006).

Inch, K., Masselink, G., Puleo, J. A., Russell, P., & Conley, D. C. Vertical structure of near-bed cross-shore flow velocities in the swash zone of a dissipative beach. Continental Shelf Research, 101, 98-108，(2015).

Karambas, T. V. Prediction of sediment transport in the swash-zone by using a nonlinear wave model. Continental Shelf Research, 26(5), 599-609, (2006).

Kelly, D. M., & Dodd, N. Beach-face evolution in the swash zone. Journal of Fluid Mechanics, 661, 316-340，(2010).

Kikkert, G. A., O'Donoghue, T., Pokrajac, D., & Dodd, N. Experimental study of bore-driven swash hydrodynamics on impermeable rough slopes. Coastal Engineering, 60, 149-166，(2012).

Kikkert, G. A., Pokrajac, D., O'Donoghue, T., & Steenhauer, K. Experimental study of bore-driven swash hydrodynamics on permeable rough slopes. Coastal engineering, 79, 42-56，(2013).

Kobayashi, N., & Johnson, B. D. Sand suspension, storage, advection, and settling in surf and swash zones. Journal of Geophysical Research: Oceans, 106(C5), 9363-9376, (2001).

Lanckriet, T., & Puleo, J. A. A semianalytical model for sheet flow layer thickness with application to the swash zone. Journal of Geophysical Research: Oceans, 120(2), 1333-1352，(2015).

Lanckriet, T., & Puleo, J. A. Near-bed turbulence dissipation measurements in the inner surf and swash zone. Journal of Geophysical Research: Oceans, 118(12), 6634-6647，(2013).

Lanckriet, T., Puleo, J. A., Masselink, G., Turner, I. L., Conley, D., Blenkinsopp, C., & Russell, P. Comprehensive field study of swash-zone processes. II: Sheet flow sediment concentrations during quasi-steady backwash. Journal of Waterway, Port, Coastal, and Ocean Engineering, 140(1), 29-42，(2013).

Liu, P. L. F., Park, Y. S., & Cowen, E. A. Boundary layer flow and bed shear stress under a solitary wave. Journal of Fluid Mechanics, 574, 449-463，(2007).

Longo, S., Petti, M., & Losada, I. J. Turbulence in the swash and surf zones: a review. Coastal Engineering, 45(3), 129-147，(2002).

Masselink, G., Evans, D., Hughes, M. G., & Russell, P. Suspended sediment transport in the swash zone of a dissipative beach. Marine Geology, 216(3), 169-189，(2005).

Masselink, G., & Puleo, J. A. Swash-zone morphodynamics. Continental Shelf Research, 26(5), 661-680, (2006)_

Masselink, G., & Russell, P. Flow velocities, sediment transport and morphological change in the swash zone of two contrasting beaches. Marine Geology, 227(3), 227-240，(2006).

Masselink, G., Russell, P., Turner, I., & Blenkinsopp, C. Net sediment transport and morphological change in the swash zone of a high-energy sandy beach from swash event to tidal cycle time scales. Marine Geology, 267(1), 18-35，(2009).

Mihoubi, M. K., Bélorgey, M., & Kettab, A. Determination of the interstitial velocity field in the swash zone by Ultrasonic Doppler Velocimetry (UDV). Comptes Rendus Geoscience, 344(5), 312-318, (2012).

Miles, J., Butt, T., & Russell, P. Swash zone sediment dynamics: A comparison of a dissipative and an intermediate beach. Marine Geology, 231(1), 181-200，(2006).

Nielsen, Peter. Coastal bottom boundary layers and sediment transport. World Scientific, 1992.

Nikuradse, J. Gesetzmassingket der turbulenten Stromung in glattten Rohren. VDIForschungsheft, (1932).

Nadaoka, K., Hino, M., & Koyano, Y. Structure of the turbulent flow field under breaking waves in the surf zone. Journal of Fluid Mechanics, 204, 359-387, (1989).

O'donoghue, T., Pokrajac, D., & Hondebrink, L. J. Laboratory and numerical study of dambreak-generated swash on impermeable slopes. Coastal Engineering, 57(5), 513-530，(2010).

Othman, I. K., Baldock, T. E., & Callaghan, D. P. Measurement and modelling of the influence of grain size and pressure gradient on swash uprush sediment transport. Coastal Engineering, 83, 1-14，(2014).

Osborne, P. D., & Rooker, G. A. Sand re-suspension events in a high energy infragravity swash zone. Journal of Coastal Research, 74-86, (1999).

Petti, M., & Longo, S. Turbulence experiments in the swash zone. Coastal Engineering, 43(1), 1-24，(2001).

Pedrozo-Acuña, A., de Alegría-Arzaburu, A. R., Torres-Freyermuth, A., Mendoza, E., & Silva, R. Laboratory investigation of pressure gradients induced by plunging breakers. Coastal Engineering, 58(8), 722-738, (2011).

Pintado-Patiño, J. C., Torres-Freyermuth, A., Puleo, J. A., & Pokrajac, D. On the role of infiltration and exfiltration in swash zone boundary layer dynamics. Journal of Geophysical Research: Oceans, 120(9), 6329-6350，(2015).

Postacchini, M., Othman, I. K., Brocchini, M., & Baldock, T. E. Sediment transport and morphodynamics generated by a dam-break swash uprush: Coupled vs uncoupled modeling. Coastal Engineering, 89, 99-105，(2014).

Pope, S.B. Turbulent flows. University press, Cambridge, UK, (2000).

Pritchard, D., & Hogg, A. J. On the transport of suspended sediment by a swash event on a plane beach. Coastal Engineering, 52(1), 1-23, (2005).

Pujara, N., & Liu, P. L. F. Direct measurements of local bed shear stress in the presence of pressure gradients. Experiments in fluids, 55(7), 1767, (2014).

Pujara, N., Liu, P. L. F., & Yeh, H. The swash of solitary waves on a plane beach: flow evolution, bed shear stress and run-up. Journal of Fluid Mechanics, 779, 556-597, (2015).

Puleo, J. A., & Butt, T. The first international workshop on swash-zone processes，(2006).

Puleo, J. A., Beach, R. A., Holman, R. A., & Allen, J. S. Swash zone sediment suspension and transport and the importance of bore-generated turbulence，(2000).

Puleo, J. A., Blenkinsopp, C., Conley, D., Masselink, G., Turner, I. L., Russell, P., ... & Poate, T. Comprehensive field study of swash-zone processes. I: Experimental design with examples of hydrodynamic and sediment transport measurements. Journal of Waterway, Port, Coastal, and Ocean Engineering, 140(1), 14-28，(2013).

Puleo, J. A., & Butt, T. The first international workshop on swash-zone processes，(2006).

Puleo, J. A., & Holland, K. T. Estimating swash zone friction coefficients on a sandy beach. Coastal engineering, 43(1), 25-40，(2001).

Puleo, J. A., Lanckriet, T., & Wang, P. Near bed cross-shore velocity profiles, bed shear stress and friction on the foreshore of a microtidal beach. Coastal

Engineering, 68, 6-16，(2012).

Puleo, J. A., & Torres-Freyermuth, A. The second international workshop on swash-zone processes. Coastal Engineering, 115, 1-7，(2016).

Raubenheimer, Britt, Steve Elgar, and R. T. Guza. "Observations of swash zone velocities: A note on friction coefficients." Journal of Geophysical Research: Oceans 109.C1 (2004).

Raffel, M., Willert, C. E., Wereley, S., & Kompenhans, J. Particle image velocimetry: a practical guide. Springer, 448 pages, (2013).

Ronneberger, Olaf, M. Raffel, and J. Kompenhans. "Advanced evaluation algorithms for standard and dual plane particle image velocimetry." Proceedings of the 9th International Symposium on Applied laser techniques to fluid mechanics, Lisbon, Portugal, paper. Vol. 10. 1998.

Ruju, A., Conley, D., Masselink, G., & Puleo, J. Sediment transport dynamics in the swash zone under large-scale laboratory conditions. Continental Shelf Research, 120, 1-13，(2016).

Shavit, U., Lowe, R. J., & Steinbuck, J. V. Intensity capping: a simple method to improve cross-correlation PIV results. Experiments in Fluids, 42(2), 225-240, (2007).

Shaw, W. J., & Trowbridge, J. H. The direct estimation of near-bottom turbulent fluxes in the presence of energetic wave motions. Journal of Atmospheric and Oceanic Technology, 18(9), 1540-1557, (2001).

Shin, S., & Cox, D. Laboratory observations of inner surf and swash-zone hydrodynamics on a steep slope. Continental Shelf Research, 26(5), 561-573，(2006).

Sou, I. M., Cowen, E. A., & Liu, P. L. F. Evolution of the turbulence structure in the surf and swash zones. Journal of Fluid mechanics, 644, 193-216，(2010).

Sou, In Mei, and Harry Yeh. "Laboratory study of the cross-shore flow structure in the surf and swash zones." Journal of Geophysical Research: Oceans 116.C3 (2011).

Steenhauer, K., Pokrajac, D., O'Donoghue, T., & Kikkert, G. A. Subsurface

processes generated by bore-driven swash on coarse-grained beaches. Journal of Geophysical Research: Oceans, 116(C4), (2011).

Stevens, C., & Coates, M. Applications of a maximised cross-correlation technique for resolving velocity fields in laboratory experiments. Journal of Hydraulic Research, 32(2), 195-212, (1994).

Sumer, B. Mutlu, et al. "Flow and sediment transport induced by a plunging solitary wave." Journal of Geophysical Research: Oceans 116.C1 (2011).

Sumer, B. M., Guner, H., Hansen, N. M., Fuhrman, D. R., & Fredsøe, J. Laboratory observations of flow and sediment transport induced by plunging regular waves. Journal of Geophysical Research: Oceans, 118(11), 6161-6182, (2013).

Thielicke, W., & Stamhuis, E. PIVlab–towards user-friendly, affordable and accurate digital particle image velocimetry in MATLAB. Journal of Open Research Software, 2(1), (2014).

Torres-Freyermuth, A., Puleo, J. A., & Pokrajac, D. Modeling swash-zone hydrodynamics and shear stresses on planar slopes using Reynolds-Averaged Navier–Stokes equations. Journal of Geophysical Research: Oceans, 118(2), 1019-1033，(2013).

Trowbridge, J. H. On a technique for measurement of turbulent shear stress in the presence of surface waves. Journal of Atmospheric and Oceanic Technology, 15(1), 290-298, (1998).

Vousdoukas, M. I., Kirupakaramoorthy, T., Oumeraci, H., De La Torre, M., Wübbold, F., Wagner, B., & Schimmels, S. The role of combined laser scanning and video techniques in monitoring wave-by-wave swash zone processes. Coastal Engineering, 83, 150-165. (2014).

Watanabe, Y., Saeki, H., & Hosking, R. J. Three-dimensional vortex structures under breaking waves. Journal of Fluid Mechanics, 545, 291-328，(2005).

Weir, F. M., Hughes, M. G., & Baldock, T. E. Beach face and berm morphodynamics fronting a coastal lagoon. Geomorphology, 82(3), 331-346, (2006).

Wei, T., & Willmarth, W. W. Reynolds-number effects on the structure of a

turbulent channel flow. Journal of Fluid Mechanics, 204, 57-95, (1989).

Watanabe, Y., Horii, M., & Niida, Y. Mechanical Balance to Form Flow Structures in a Run-Up Wave Journal of Japan Society of Civil Engineers, Ser. B2 (Coastal Engineering) Vol. 69 No. 2, I_66-I_70, (2013).

Yeh, H.H., Ghazali, A. On bore collapse. J. Geophys. Res. Oceans 93, 6930–6936, (1988).

Zhang, Q., & Liu, P. L. F. A numerical study of swash flows generated by bores. Coastal Engineering, 55(12), 1113-1134, (2008).